DISSERTATION

submitted to the

Combined Faculty of Mathematics, Engineering and Natural Sciences

of Heidelberg University, Germany

for the degree of

Doctor of Natural Sciences

Put forward by

Martin Klassen

born in: Trier

Oral examination: 26 October 2023

Measurement of the Invisible Width of the Z Boson with the ATLAS Detector

Referees: Prof. Dr. Monica Dunford
Prof. Dr. Stephanie Hansmann-Menzemer

Zusammenfassung

Die Messung der partiellen Zerfallsbreite des Z-Bosons in unsichtbare Teilchen stellt einen präzisen Test der elektroschwachen Struktur des Standardmodells der Teilchenphysik dar. In dieser Arbeit wird eine Messung dieser Größe mit dem ATLAS Detektor am Large Hadron Collider unter der Verwendung von Proton-Proton Kollisionsdaten vorgestellt, die bei einer Schwerpunktsenergie von $13\,\text{TeV}$ produziert wurden und einer integrierten Luminosität von $37\,\text{fb}^{-1}$ entsprechen. Es werden Ereignisse mit fehlendem Transversalimpuls, die mit mindestens einem hochenergetischen Jet assoziiert sind, selektiert. Verhältnisse der so erhaltenen unsichtbaren Z-Boson Zerfälle zu Zerfällen des Z-Bosons in Paare entgegengesetzt geladener Elektronen oder Myonen werden konstruiert. Diese Verhältnisse werden bezüglich Detektoreffekten korrigiert und zu einem Verhältnis der Verzweigungsverhältnisse $\hat{R}^{\text{miss}}$ kombiniert. Diese Relation ergibt zusammen mit der leptonischen Zerfallsbreite des Z-Bosons, welche am Large Electron-Positron Collider gemessen wurden, $\Gamma_Z(\text{inv})$. Die gemessene unsichtbare Zerfallsbreite ist 506 ± 2 (stat.) $\pm$ 12 (syst.) MeV und zeigt damit sehr gute Übereinstimmung mit der Vorhersage des Standardmodells und mit vorherigen Messungen. Dieses Ergebnis ist zum jetzigen Zeitpunkt die präziseste Einzelmessung, die auf dem Endzustand mit fehlendem Transversalimpuls basiert.

Abstract

The measurement of the partial decay width of the Z boson into invisible particles represents a precision test of the electroweak structure of the Standard Model of particle physics. In this thesis, a measurement of the invisible Z boson width with the ATLAS detector at the Large Hadron Collider is presented using an integrated luminosity of $37\,\text{fb}^{-1}$ of proton-proton collision data collected at a centre-of-mass energy of $13\,\text{TeV}$. Collision events with missing transverse momentum associated with at least one highly energetic jet are selected. Ratios of the obtained invisible Z boson decays to Z boson decays into pairs of oppositely charged electrons or muons, respectively, are constructed. These ratios are corrected for detector effects and combined into a ratio of branching fractions $\hat{R}^{\text{miss}}$. This ratio is then used in combination with the leptonic Z boson width, determined at the Large Electron-Positron Collider, to derive the invisible width of the Z boson. It is measured to be 506 ± 2 (stat.) ± 12 (syst.) MeV, which is in excellent agreement with the Standard Model prediction and with previous measurements. This result is the single most precise measurement of $\Gamma_Z(\text{inv})$ to date based on missing transverse momentum in the final state.

Contents

1 Introduction

The field of particle physics strives for a complete theory describing the intrinsic nature of the Universe via elementary particles and the fundamental forces determining their interplay. The Standard Model of particle physics (SM) is extremely successful in describing these fundamental particles and their interactions. It has been consistently tested at different energy scales by various experiments. Nevertheless, the SM has several limitations, among others: it lacks a description of the generation of neutrino masses [1], it includes no viable Dark Matter candidate although it is known that Dark Matter contributes 26.8% to the total energy density [2, 3], and it does not provide an explanation of the observed matter-antimatter asymmetry in the Universe. This motivates the extensive search program for physics beyond the SM which reaches from the high energy frontier searching directly for Dark Matter candidates to precision measurements deviating from the SM. The electroweak theory describing the interactions mediated by the photon and the Z and W gauge bosons is highly predictive, which allows stringent tests of the consistency of the SM.

One key electroweak observable is the decay width of the Z boson into a neutrino-antineutrino pair. These are minimal interacting particles and therefore invisible to the detector. The corresponding invisible partial decay width $\Gamma_Z(\text{inv})$ is given by the total Z boson width times the branching fraction into invisible particles. In the SM, these are three generations of neutrinos. A deviation from the predicted $\Gamma_Z(\text{inv})$ could hint towards a new physics contribution.

After the discovery of the Z boson at the Super Proton Synchrotron proton-antiproton collider at CERN by the UA1 and UA2 experiments [4, 5], the properties of the Z boson were extensively studied at the Large Electron-Positron (LEP) collider [6]. This included two independent measurement strategies to determine $\Gamma_Z(\text{inv})$ which both unveiled the existence of exactly three generations of light neutrinos. In the first approach, the visible partial decay widths were subtracted from the total Z boson width [6–10], whereas the second approach considered a final state with missing transverse momentum, $E_{\mathrm{T}}^{\mathrm{miss}}$, and a photon which is radiated from the initial state [6, 11–13]. Recently, a measurement using a $E_{\mathrm{T}}^{\mathrm{miss}}$ +jet final state was performed with the CMS experiment at the Large Hadron Collider (LHC) [14]. Measuring the invisible Z boson width at the LHC permits testing the validity of the SM at a different energy scale and in another production environment compared to the LEP measurements. These measurements are a valuable tool to search indirectly for physics beyond the SM, even if they do not exceed the precision of the first LEP approach, as manifestations of new physics could be revealed through differences between these measurements [15].

In the measurement presented in this thesis, the $\Gamma_Z(\text{inv})$ is derived from ratios of invisible Z boson decays in association with at least one high energetic jet $Z(\rightarrow \text{invisible})$+jets to $Z(\rightarrow \ell\ell)+\text{jets}$ where $\ell\ell$ are either electrons or muons. These ratios are called R^{miss} in the remainder of this thesis. Decays into pairs of taus are not considered due to their short lifetime and the corresponding sizeable reconstruction and modelling uncertainties [16–18]. The presented $\Gamma_Z(\text{inv})$ measurement uses $37\,\text{fb}^{-1}$ collected by the ATLAS detector at a centre-of-mass energy of $\sqrt{s} = 13\,\text{TeV}$ in 2015-2016 with a lower number of simultaneous interactions compared to the full Run 2 data set [19], which improves the precision of the measurement. The hadronic recoil system is used to reconstruct the otherwise invisible decays of the Z boson into neutrinos pairs. The ratio measurements are performed as a function of $p_{\text{T},Z}$ as it is approximately equal to the p_{T} of the hadronic recoil system. This recoil system is very similar for the different decay channels of the Z boson. Corrections to the measured R^{miss} are necessary such that the numerator and the denominators are within a common kinematic phase space which allows the combination of the electron and muon channels, thereby improving the overall precision of the measurement. The invisible width is then obtained by deriving the best estimator $\hat{R}^{\text{miss}}$ of the measured ratios combined with the leptonic width $\Gamma_Z(\ell\ell)$ measured at LEP under the assumption of lepton universality.

The benefit of ratio measurements is the cancellation of systematic uncertainties. In the presented analysis, these are on the experimental side mainly the systematic uncertainties related to the hadronic recoil system. In addition, the theoretical uncertainties are reduced as they are treated as fully correlated between the numerator and the denominator. These ratio measurements are also an established approach in the determination of branching fractions often used in flavour physics [20].

The remainder of this thesis is structured as follows: The key aspects of the Standard Model relevant for the presented $\Gamma_Z(\text{inv})$ measurement are summarised together with previous measurements of this parameter in Chapter 2. In Chapter 3, the LHC and the ATLAS experiment are introduced. Chapter 4 discusses the collision event simulation using Monte Carlo generators, and the reconstruction of the physic objects measured by the detector is presented in Chapter 5. The data set, the collision event selection and the definition of the signal regions follow in Chapter 6. The background contributions to these signal regions are derived in Chapter 7, which is followed by a discussion of the systematic uncertainties in Chapter 8. The detector level results are shown in Chapter 9 and Chapter 10 focuses on the detector correction to a common particle level phase space. The particle level R^{miss} ratios and the extraction of $\Gamma_Z(\text{inv})$ are described in Chapter 11. Chapter 12 summarises the $\Gamma_Z(\text{inv})$ measurement.

Author's Contribution

The presented measurement is performed within the ATLAS collaboration which designed, constructed and ensures a successful operation of the ATLAS detector enabling the collection of collision data. Software frameworks for the calibration and the reconstruction of the particles and event quantities are provided by the collaboration to ensure the presence of standardised objects in the analyses. The $\Gamma_Z(\text{inv})$ measurement relies on these frameworks and additional helpful software tools.

The author contributed to the successful data-taking in 2018 by supporting the Level-1 calorimeter trigger operation on-site at CERN and by optimising the calibration of this trigger, particularly focusing on the forward calorimeter. Parts of this work are documented in [21].

The work performed by the author required extensive data processing which to a substantial fraction was conducted on the ATLAS Heidelberg High Throughput computing cluster. The author was part of the administrator team and was responsible for the maintenance and operation of the cluster.

Prior to the $\Gamma_Z(\text{inv})$ measurement, the author provided several contributions to the detector-corrected cross section measurement of boson + jet processes which are interpreted in terms of physics beyond the Standard Model. These include among others: optimisations of the chosen bin widths, sensitivity studies of the baseline lepton isolation, impact studies of switched-off tile modules in 2018 on the missing transverse momentum in the affected areas, enhancements of the interpretation framework, dark matter sensitivity studies, implementation of a Rivet routine for the photon + jet channel, extensive studies of the particle level photon isolation to resemble the performance of the isolation on the detector level, and validation of the analysis framework.

The current state of this analysis is summarised in [22, 23]. For the sake of clarity of the presented analysis, the remainder of this thesis solely concentrates on the $\Gamma_Z(\text{inv})$ measurement. Nevertheless, several frameworks, tools, and methods used and developed in the detector-corrected cross section measurement are adapted and expanded to the needs of the presented work.

The $\Gamma_Z(\mathrm{inv})$ measurement described in this thesis is performed almost solely by the author. Exceptions are the original analysis design idea, the phase space definitions which were adjusted to this analysis from a previous detector corrected dark matter search [24] by collaborators and only re-optimised by the author to reject fake background sources, a particle level study that R^{miss} is constant as a function of $p_{\mathrm{T},Z}$ [25], the derivation of the theory correction for virtual photon contributions, and the production of the uncertainty simulation samples. Background estimation techniques used in [22] which are re-implemented and re-optimised for the $\Gamma_Z(\mathrm{inv})$ phase spaces include the QCD multijet smearing, non-collision estimation, and the matrix method for the fake lepton background. The consideration of an additional source of $E_{\mathrm{T}}^{\mathrm{miss}}$ in the QCD multijet background estimation and the expansion of the matrix method to muons and two charged lepton final states are two examples emphasising the necessity of adjustments of those methods due to different phase spaces.

Both analyses are expected to be published soon and are at advanced stages in the internal ATLAS review process. The $\Gamma_Z(\mathrm{inv})$ measurement is published as a conference note [26] and the publication of the corresponding paper is foreseen within the next weeks.

2 Theoretical Foundation

The Standard Model of Particle Physics is the backbone of the presented $\Gamma_Z(\text{inv})$ measurement. A brief summary of this quantum field theory focusing on the relevant aspects to this analysis is presented in Section 2.1. The measurement presented in this thesis is set into a broader perspective by providing a summary of previous direct and indirect measurements of the invisible width of the Z boson in Section 2.2.

2.1 The Standard Model of Particle Physics

The behaviour of free particles and their interactions among each other are described by the Standard Model of particle physics (SM). Glashow, Salam and Weinberg [27–29] laid the foundation of the mathematical description of the SM by developing the electroweak theory which combined with the theory of quantum chromodynamics (QCD) obeys the local gauge symmetry $SU(3)_C \otimes SU(2)_L \otimes U(1)_Y$.

Figure 2.1 provides an overview of the particle content of the SM including their respective quantum numbers as well as measured masses. The carriers of the three fundamental forces described within the SM are spin-1 gauge bosons. The strong interaction is transmitted by eight massless gluons which carry a so-called colour charge. The presence of colour and anti-colour in every gluon enables self-couplings which limits the range of this interaction. The electromagnetic force is mediated by massless photons between charged particles and has an infinite range. The weak interaction introduces charged current interactions where a W^+ or W^- boson is exchanged as well as a neutral current interaction mediated by the Z boson. The force carriers of the weak interaction obtain masses via spontaneous symmetry breaking which will be discussed in Section 2.1.1. Weak interactions are suppressed below the heavy gauge boson masses.

Down to the present day no incorporation of a quantised version of gravity, the fourth known fundamental force, into the SM has been found. The SM nevertheless provides a successful description of the observed experimental particle physics data as the attractive gravitational interaction acting on all particles is extremely feeble even compared to the weak force.

The particle content of the fermionic sector of the SM contains 12 spin $\frac{1}{2}$ particles

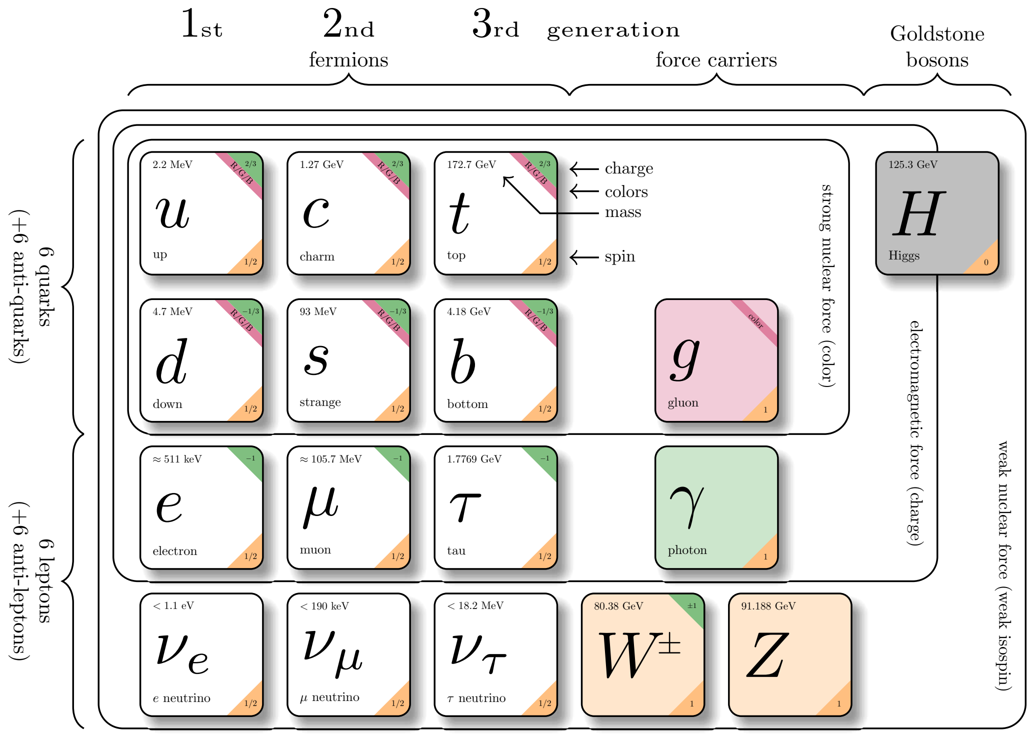

Figure 2.1: Overview of the particle content of the Standard Model including the particle mass [1], spin (orange), electrical charge (green) and colour charge (red). Adopted from [30].

which can be categorised into quarks and leptons depending on being affected by the strong force or not. These fermions can be grouped into three generations with identical properties besides an increasing mass and a different flavour state. All fermions undergo weak interactions and have a corresponding anti-particle with the same mass and spin but otherwise opposite quantum numbers.

Each generation of leptons consists of a charged particle, the electron, muon or tau and a corresponding electrical neutral neutrino. The charged leptons carry one negative unit of electrical charge, the charge of the electron e, whereas their respective anti-particles carry an opposite charge.

The quark generations are constructed from an up-type and a down-type quark which have different fractional elementary electrical charges of $\frac{2}{3}$ and $-\frac{1}{3}$. The six different flavour states are the up, charm, top as well as the down, strange and bottom. All quarks carry one of three different colour charges (red, blue, green) and due to the confinement of QCD form bound states, so-called hadrons. A hadron constructed from a quark and an anti-quark is called a meson whereas bound states of three quarks with three different colours are referred to as baryons.

The Higgs boson is the only scalar particle (spin-0) in the SM and was detected by the ATLAS and CMS experiments in 2012 [31, 32]. The Higgs mechanism [33–35] provides masses to the fermions and the weak gauge bosons. Higgs self-couplings are expected as the Higgs itself is massive.

Despite its tremendous success in describing and even predicting the behaviour of particles and their interactions at the tested energy scales it also has various shortcomings which indicate that the SM in its current form is incomplete. In the SM neutrinos remain massless even after the spontaneous symmetry breaking which is in clear contrast to observed neutrino oscillations [1]. Hence the SM lacks a mechanism to generate neutrino masses for which until the present day only upper mass limits could be set. A further shortcoming of the SM is that despite the overwhelming cosmological evidence for the existence of dark matter [3] there is no suitable dark matter candidate in the SM which is one of the biggest puzzles in particle physics which still needs to be resolved. The combined violation of charge and parity (CP) in the quark sector in the SM is not sufficient to provide an explanation for the observed matter-antimatter asymmetry in the Universe. CP violation is still unobserved in the lepton sector, but it is likely that an additional source beyond this potential SM contribution is required.

Alongside these experimental evident problems, there are also theoretically motivated deficits. As aforementioned, the SM does not include a description of gravity which is instead modelled by general relativity. The several order of magnitude difference between the different lepton and quark masses which are inserted as external parameters into the SM call for an underlying flavour theory motivating the mass hierarchies for the three generations. The absence of CP violation in the strong sector motivates searches for additional pseudoscalars, for example, the axion, whereas the hierarchy problem of the Higgs is still the main driving force behind supersymmetric extensions of the SM.

As the decay characteristics of the Z boson are solely determined by the electroweak part of the SM an emphasis will be placed on the corresponding theory in Section 2.1.1 following [1, 36–38]. Nevertheless, producing the Z boson at a hadron collider makes it impossible to omit an adequate discussion of the strong interaction which is presented in Section 2.1.2 based on [36, 39].

2.1.1 The Electroweak Theory

The simplest group which combines the weak and the electromagnetic interaction is $SU(2)_L \otimes U(1)_Y$. The weak interaction transforms left- and right-handed fermions differently. Left-handed fermions are grouped into doublets $\psi_i = \binom{u_i}{d^{'}_i}_L$ and $\binom{\nu_i}{l_i}_L$ where the index i runs over the generations and $d^{'} = \sum_j V_{ij} d_j$ are the weak eigenstates obtained from the mass eigenstates via the rotation matrix V_{ij} known as the Cabibbo-Kobayashi-Maskawa matrix [40, 41]. The right-handed states are singlets under $SU(2)_L$. The generators of the $SU(2)_L$ symmetry are the three gauge bosons W^i_μ with $i \in [1, 2, 3]$. The fourth generator of the electroweak sector stems from the $U(1)_Y$ gauge group and is denoted B_μ. It carries the hypercharge Y which is defined as $Y = Q - T_3$, where Q is the electrical charge and T_3 is the third component of the weak isospin which is $+1/2$ for the upper component of the doublets, $-1/2$ for the lower component and 0 for the singlets. The electroweak Lagrangian can be written as

$$\mathcal{L}_{\mathrm{EW}} = \sum_\psi i\bar{\psi}\gamma^\mu D_\mu \psi - \frac{1}{4} W^i_{\mu\nu} W^{\mu\nu}_i - \frac{1}{4} B_{\mu\nu} B^{\mu\nu}, \tag{2.1}$$

where the fermion sector is described by the Dirac matrices γ^μ and the covariant derivative $D_\mu = \partial_\mu + i\frac{g}{2}\sigma_i W^i_\mu + ig^{'} Y B_\mu$ acting on the fermion fields ψ. The second term which includes the Pauli matrices σ_i only acts on left-handed fields. The coupling strength of the weak interaction is denoted as g whereas the coupling strength of the electromagnetic interaction is given by $g^{'}$. The field strength tensors of the gauge sector are defined as $W^i_{\mu\nu} = \partial_\mu W^i_\nu - \partial_\nu W^i_\mu - ig\epsilon_{ijk} W^j_\mu W^k_\nu$ with ϵ_{ijk} being the anti-symmetric Levi-Civita tensor and $B_{\mu\nu} = \partial_\mu B_\nu - \partial_\nu B_\mu$. The respective gauge terms provide the kinetic terms of these gauge fields as well as their self-interactions in the case of the non-Abelian W^i bosons.

The symmetries of the SM do not allow any explicit mass terms for both the fermions and the gauge bosons which is in clear contrast with the observations in nature. An additional field charged under the $SU(2)_L$ hence becomes necessary, a complex scalar Higgs doublet $\phi = \begin{pmatrix} \phi^+ \\ \phi^0 \end{pmatrix}$. The corresponding Lagrangian is given by

$$\mathcal{L}_{\mathrm{Higgs}} = |D_\mu \phi|^2 - \mu^2 \phi^\dagger \phi - \lambda \left(\phi^\dagger \phi\right)^2, \tag{2.2}$$

with the same covariant derivative as above. The last two terms define the Higgs potential. The interactions between the fermions and the Higgs boson are described by the Yukawa Lagrangian which ultimately also generates the masses of the fermions after electroweak symmetry breaking:

$$\mathcal{L}_{\text{Yukawa}} = \sum_f Y_f \left(\bar{\psi}_L \phi \psi_R + \bar{\psi}_L \tilde{\phi} \psi_R + \text{h.c.} \right) \,, \tag{2.3}$$

with the Yukawa coupling Y_f which in its most general form is a 3×3 matrix and the conjugated Higgs doublet field $\tilde{\phi}$. The electroweak gauge symmetry is spontaneously broken to a $U(1)_{\text{em}}$ of electromagnetism by the neutral component of the Higgs acquiring a vacuum exception value, $v = \sqrt{\frac{-\mu^2}{2\lambda}} \approx 246$ GeV, deviating from zero which requires $\mu^2 < 0$ as the potential should be bounded from below demanding $\lambda > 0$. The breaking of the symmetry results in the appearance of three massless Goldstone bosons alongside the massive scalar Higgs boson. These can be associated with the physical $W^{\pm}$ and Z bosons which absorb these additional degrees of freedom as longitudinal polarisations and thereby become massive. The mass of the Z boson can easiest be derived from the kinetic term of the Higgs Lagrangian in unitary gauge and is $m_Z = \frac{1}{2}\sqrt{g^2 + g'^2}v$. The weak mixing angle is defined as $\theta_W = \tan^{-1}\left(\frac{g'}{g}\right)$. The weak gauge bosons and the photon field A can now be expressed as

$$Z_\mu = -\sin_{\theta_W} B_\mu + \cos_{\theta_W} W^3_\mu, \quad A_\mu = \cos_{\theta_W} B_\mu + \sin_{\theta_W} W^3_\mu, \quad W^{\pm}_\mu = \frac{W^1_\mu \mp i W^2_\mu}{\sqrt{2}}. \tag{2.4}$$

At tree-level the neutral current interaction between the fermions and the Z boson can be expressed as

$$\mathcal{L}_Z = -\frac{g}{2\cos\theta_W} \sum_f \bar{\psi}_f \gamma^\mu \left(c^f_V - c^f_A \gamma^5 \right) \psi_f Z_\mu, \tag{2.5}$$

with the vector current coupling $c^f_V = T^f_3 - 2Q^f \sin^2\theta_W$ and the axial vector current coupling $c^f_A = T^f_3$. The partial decay widths of the Z boson at tree-level neglecting the fermion masses can then be calculated:

$$\Gamma_Z(f\bar{f}) = N_c \frac{\sqrt{2} G_F m^3_Z}{12\pi} \left(c^{f^2}_V + c^{f^2}_A \right), \tag{2.6}$$

including a colour factor N_c which enhances the decay rate into quarks and the Fermi constant $G_F = 1/\left(\sqrt{2}v^2\right)$. Leading order electroweak corrections can be partially incorporated in a running of the fine-structure constant and G_F whereas QCD corrections in case of decays into quarks can be expressed in terms of an effective number of colours. The rest of the electroweak corrections can be absorbed by a redefinition of the vector and axial vector couplings $\hat{c}_V^f = \sqrt{\rho_Z^f}\left(T_3^f - 2Q^f \sin^2\theta_{W,\mathrm{eff}}\right)$ with $\sin^2\theta_{W,\mathrm{eff}} = \kappa_Z^{f^2}\sin^2\theta_W$ and $\hat{c}_A^f = \sqrt{\rho_Z^f T_3^f}$ where κ_Z^f and ρ_Z^f depend on the centre-of-mass energy. QCD final state radiation corrections are currently known up to four orders in the strong coupling constant whereas QED final state radiation is calculated in up to two orders [1].

The sum of all possible fermion decay channels yields $\Gamma_Z = 2.4941 \pm 0.0009$ GeV which is in perfect agreement with the measured total width of 2.4955 ± 0.0023 GeV [1]. This already indicates a particular strength of the electroweak sector: it is highly predictive and therefore can be tested in a multitude of observables which only depend on the four key parameters: $g, g^{'}, v$ and the Higgs mass m_h.

The parameter of interest in the presented analysis $\Gamma_Z(\mathrm{inv})$ is the decay width of the Z boson into pairs of neutrinos and potential additional final states beyond the SM which would also leave the detector undetected. $\Gamma_Z(\mathrm{inv})$ can be obtained via a ratio measurement of Z decays into pairs of charged leptons compared to invisible decays which in the SM are decays into pairs of neutrinos. Equation 2.6 provides a direct handle on this quantity omitting small fermion mass corrections [36]

$$R_{ll}^{\mathrm{miss}} = \frac{\Gamma_Z(\mathrm{inv})}{\Gamma_Z(ll)} = \frac{T_3^{\nu^2} N_\nu}{\left(T_3^{l^2} - 2Q^{l^2}\sin^2\theta_{W,\mathrm{eff}}\right)^2 + T_3^{l^2}} = \frac{2N_\nu}{\left(1 - 4\sin^2\theta_{W,\mathrm{eff}}\right)^2 + 1} \approx 5.966 \ , \tag{2.7}$$

for $\sin^2\theta_{W,\mathrm{eff}} = 0.23122$. The universality of the neutral current couplings to the charged leptons enables a direct combination of the electron and the muon R^{miss}.

The leptonic decay pattern of the Z boson is solely defined by the electroweak theory. However, the production of the Z boson in association with jets depends on the strong interaction which is described next.

2.1.2 The Strong Interaction

The interaction between quarks and gluons can be described by the theory of quantum chromodynamics. This quantum field theory obeys an invariance under local $SU(3)_c$ colour transformations. The corresponding colour charge is assigned to the quarks and is conserved within strong interactions. Ratio measurements of the hadronic to the muon cross section in electron-positron collisions showed that there are exactly three different quark colours. Eight differently charged gluons are the force carriers of the strong interaction which is embedded in the dimensionality of the adjoined representation of $SU(3)_c$. These gauge fields of QCD are massless as a mass term is forbidden by local gauge symmetry. The Lagrangian of QCD can then be written as

$$\mathcal{L}_{\mathrm{QCD}} = \bar{\psi}_q^i \left(i\gamma^\mu\right) D_{\mu,ij}\psi_q^j - m_q\bar{\psi}_q^i\psi_q^j - \frac{1}{4}G_{\mu\nu}^a G^{a,\mu\nu}. \tag{2.8}$$

The quark fields $\bar{\psi}_q^i$ are summed over flavour, q, as well as colour, i, and m_q represents the quark mass. The quark mass term however is not invariant under the full SM gauge group. The covariant derivative is given by $D_{\mu,ij} = \delta_{ij}\partial_\mu - ig_s t_{ij}^a G_\mu^a$ with the strong coupling constant g_s, the generators of $SU(3)_c$ t_{ij}^a with the colour index a which are proportional to the Gell-Mann matrices, and the gluon field G_μ^a. The gluon field strength tensor corresponds to $G_{\mu\nu}^a = \partial_\mu G_\nu^a - \partial_\nu G_\mu^a + g_s f^{abc} G_\mu^b G_\nu^c$. The structure constants f^{abc} arise due to the non-Abelian characteristic of QCD and enable cubic and quartic gluon self couplings.

A prominent feature of the strong interaction is that the strong coupling constant $g_s = \sqrt{4\pi\alpha_s}$ changes logarithmically with energy. This running of the coupling can be expressed depending on a renormalisation scale μ_R as

$$\mu_R^2\frac{\partial\alpha_s}{\partial\mu_R} = \frac{\partial\alpha_s}{\partial\ln\mu_R^2} = \beta\left(\alpha_s\right) \quad \text{with} \quad \beta = -\alpha_s\left(\beta_0 + \beta_1\alpha_s + \beta_2\alpha_s^2 + ...\right). \tag{2.9}$$

The β-function at one loop leading order with three colour states is $\beta_0 = \frac{33-2N_f}{12\pi}$ and depends on the number of quark flavours N_f which for the up to six SM quarks returns a positive β_0. This enables a description of α_s at a reference scale M_Z

$$\alpha_s\left(\mu_R^2\right) = \alpha_s\left(M_Z^2\right)\frac{1}{1 + \beta_0\alpha_s\left(M_Z^2\right)\ln\frac{\mu_R^2}{M_Z^2} + \mathcal{O}\left(\alpha_s^2\right)}\ , \tag{2.10}$$

with $\alpha_s\left(M_Z^2\right) = 0.1179 \pm 0.0009$ [1]. The negative sign of the β function arises due to the gluon self-interaction terms and results in a decreasing coupling at high energies. The slope of the coupling changes whenever the mass threshold of a quark species is passed. At small distances corresponding to high energies, the quarks essentially become free particles which is also known as asymptotic freedom. At low energies, in particular, at the QCD scale $\Lambda_{\mathrm{QCD}} \approx 200\,\mathrm{MeV}$, the coupling becomes large and a perturbative description of QCD breaks down. Hadronisation, the process of quarks forming bound states, is the most important consequence leading to the fact that quarks cannot be observed as free particles which is commonly referred to as confinement.

A summation over the outgoing colour states and an averaging over the incoming colour states needs to be performed in cross section calculations including quarks as the colour state of a quark cannot be measured due to confinement.

The strong interaction manifests itself in several places in the presented measurement: among others in the parton distribution functions of the initial colliding protons, in the higher order perturbation theory being responsible for the description of the radiation of the leading jet, in the modelling of the lepton isolation or in the rate of jets being mis-identified as leptons.

2.2 Γ_Z(inv) Measurements

The number of light neutrino families is one of the fundamental results obtained at the Large Electron-Positron Collider (LEP) and is directly related to the invisible width of the Z boson. The invisible width of the Z boson was measured both directly and indirectly at the experiments at LEP in 1990-1995. The direct measurement relied on the initial state radiation of a photon and was performed at ALEPH [11], L3 [12] and OPAL [13] and is discussed in greater detail in Section 2.2.2. In the indirect approach, the total Z lineshape was measured from which the partial visible widths are subtracted yielding $\Gamma_Z(\text{inv}) = 499.0 \pm 1.5\,\text{MeV}$ [1, 6] for the combination of the four LEP experiments [7–10]. In addition, is the discussion of the direct and indirect Γ_Z(inv) measurements based on [37, 42].

In 2022 CMS published a direct measurement of the invisible width of the Z boson obtaining $523 \pm 3\,(\text{stat.}) \pm 16\,(\text{syst.})\,\text{MeV}$ following a similar strategy as outlined in this thesis measuring Z boson decays into neutrinos, electrons and muons but extracting Γ_Z(inv) in a combined fit [14].

2.2.1 Indirect Γ_Z(inv) Measurements

The invisible partial width of the Z boson can be determined by subtracting the visible partial widths from the total width Γ_Z. The visible partial decay widths can be obtained from so-called lineshape measurements for which Z boson decay cross sections $\sigma_{f\bar{f}}$ are measured as a function of the centre-of-mass energies. An energy scan was hence performed at LEP consisting of seven distinct energies within a 3 GeV interval around the Z boson mass, $\sqrt{s} \approx m_Z$. A total of 17×10^6 Z boson decays were recorded [6].

The cross section of a Z boson decaying into a pair of leptons or quarks, up to the bottom quark, at lowest order is given by

$$\sigma\left(e^+e^- \to Z \to f\bar{f}\right) = \frac{12\pi}{m_Z^2}\frac{s\Gamma_{ee}\Gamma_{f\bar{f}}}{\left(s-m_Z^2\right)^2 + s^2\Gamma_Z^2/m_Z^2}. \tag{2.11}$$

From this Breit-Wigner function, m_Z and Γ_Z can be extracted if the corresponding cross sections are determined at different $\sqrt{s}$. The performed fits of the four experiments to the hadronic and leptonic cross sections consider the interference with an off-shell photon, contributing at the percent level close to the Z boson mass, and extract a total of nine parameters. Those are besides m_Z and Γ_Z, the hadronic peak cross section σ^0_{had}, three leptonic to hadronic cross section ratios $R_{e,\mu,\tau}$, and three forward-backward asymmetries $A^{\text{FB}}_{e,\mu,\tau}$. The $R_{e,\mu,\tau}$ ratios, which are used to reduce systematic uncertainties and correlations compared to directly using the partial decay widths, are defined as

$$R_l = \frac{\sigma^0_{\text{had}}}{\sigma^0_{l^+l^-}} = \frac{\Gamma_{\text{had}}}{\Gamma_{l^+l^-}}. \tag{2.12}$$

Figure 2.2 shows the combined measured cross sections of the four LEP experiments into the hadronic final state at the seven centre-of-mass energies and a single measurement at m_Z by SLD. The cross sections obtained from the Breit-Wigner fit are shown in blue. They are corrected via theory calculations which narrow the distribution and increase the peak cross section as can be seen by the red lineshape function. This becomes necessary as the data are distorted by QED effects, in particular the initial state radiation of photons.

The combined fit over all visible decay channels and LEP experiments of the QED corrected spectra, under the assumption of lepton universality and taking a correction for the tau mass into account, yields $\Gamma_Z = 2.4952 \pm 0.0023\,\text{GeV}$. This corresponds to a short lifetime of $2.6 \times 10^{-25}\,\text{s}$.

Partial widths can be derived from the peak cross sections at $\sqrt{s} = m_Z$ as

$$\Gamma_{f\bar{f}} = \frac{\sigma^0_{f\bar{f}}\Gamma_Z^2 m_Z^2}{12\pi\Gamma_{e^+e^-}}\ , \tag{2.13}$$

after $\Gamma_{e^+e^-}$ is obtained from $\sigma^0(e^+e^- \to Z \to e^+e^-)$ where additional t-channel Bhabha scattering needs to be considered.

The indirect invisible width is then obtained by the subtraction of the visible widths

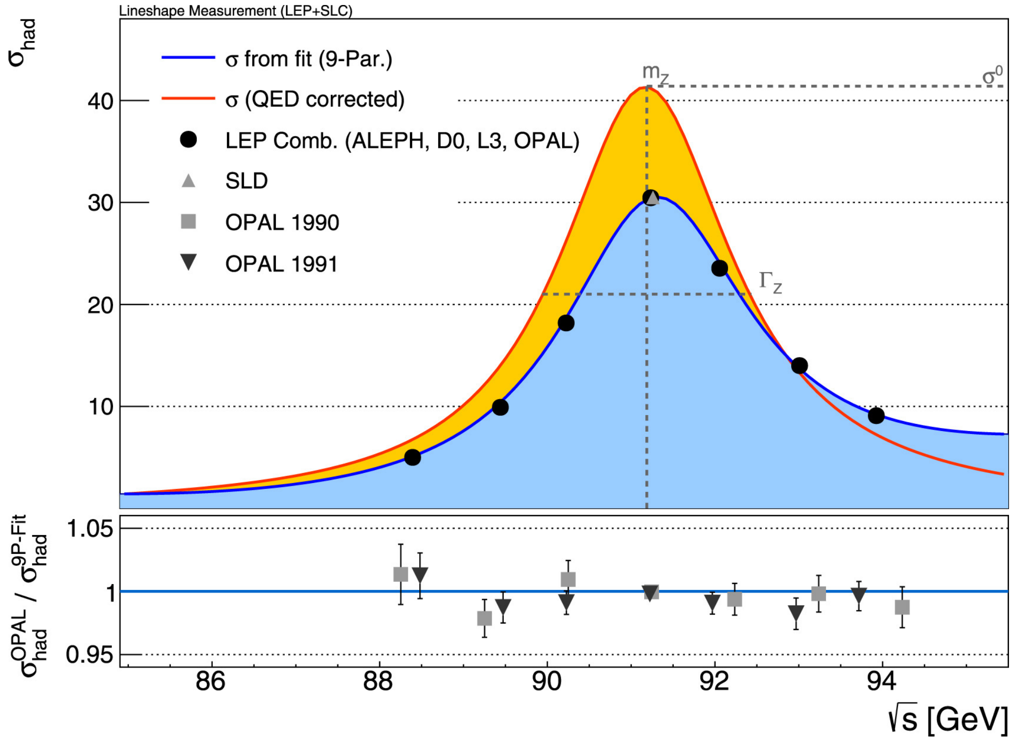

Figure 2.2: Hadronic cross sections from a combination of the four LEP experiments and from a single SLD measurement at m_Z. The lineshapes obtained by a 9-parameter Breit-Wigner fit to the LEP data with (red) and without (blue) considering QED corrections. The hadronic cross sections measured by OPAL are compared to the lineshape fit. The Figure is taken from [42].

from the total Z width assuming lepton universality

$$\Gamma_Z(\text{inv}) = \Gamma_Z - 3\Gamma_{l^+l^-} - \Gamma_{\text{had}} = 499.0 \pm 1.5\,\text{MeV} \ . \tag{2.14}$$

The individual measurements are statistically limited but compatible with each other. Significant uncertainties are those which are shared by all four experiments including the theory QED correction, luminosity, and relative beam energy calibration uncertainties. Uncertainties on the final state reconstruction differ among the experiments.

The long-standing $2\,\sigma$ deviation [6, 37] in the number of light neutrino families, which can be derived from

$$N_v = \frac{\Gamma_Z - 3\Gamma_{ll} - \Gamma_{\text{had}}}{\Gamma_{\nu\nu}^{\text{SM}}} = 2.9840 \pm 0.0082, \tag{2.15}$$

where $\Gamma_{\nu\nu}^{\text{SM}}$ is one-third of the SM predicted $\Gamma_Z(\text{inv})$ given in Table 11.1, disappeared with recent corrections to the luminosity related to beam-beam interactions and improvements to the Bhabha cross section calculation resulting in $N_\nu = 2.9963 \pm 0.0074$ alongside an increase of 0.3 MeV in Γ_Z [43, 44].

2.2.2 Direct Γ_Z(inv) Measurements

Γ_Z(inv) was directly determined at LEP by measuring the single photon production cross section at several centre-of-mass energies close to the Z resonance [6]. These measurements were performed by ALEPH, L3 and OPAL which in total analysed 2938 single photon events resulting in a combined invisible width of 503 ± 16 MeV. These results are complementary to the indirect determination of Γ_Z(inv). In particular potential exotic visible Z decays failing the event selections of the visible partial width measurements do not influence the direct measurement [15]. Limits on exotic invisible Z decays were derived in the past from the direct measurements.

Radiative QED backgrounds are the largest source of background to the single photon production where all the final state particles besides the photon are not detected. Bhabha scattering is the dominant of these background processes where the electrons are often already trapped in the beam pipe. Additional background sources are three photon production, two photon π^0 production, $l^+l^-\gamma$ as well as cosmic muons. Dedicated event selections were applied by all three experiments to reduce those backgrounds.

Each experiment performed a combined likelihood fit of the obtained cross sections using Equation 2.15 with varied $\sqrt{\hat{s}} \approx \sqrt{s} - E_\gamma$ taking the varied centre-of-mass energy into account due to the initial state photon radiation. The mass of the Z boson, the total width and the partial width in electrons were set to the values obtained from the lineshape measurements within each experiment. The maximum likelihood fit determined the number of signal events by taking the $W - Z$ interference in the t-channel for electron neutrinos into account. The total width was fixed in the fit which made Γ_Z(inv) the parameter of interest.

The uncertainties on the luminosity and the energy scale of the beam are highly correlated between the experiments. The experimental uncertainties such as the trigger efficiency for photons above 1-1.5 GeV, the estimates of subtracted backgrounds, selection efficiencies as well as uncertainties of the fit among others depend on the respective experiment. The direct Γ_Z(inv) measurements of each experiment tend to be statistically limited, except for the L3 measurement where the systematic uncertainties are of similar size.

An overview of the directly measured $\Gamma_Z(\text{inv})$, the value obtained from the combined indirect measurements and the SM prediction is given in Table 2.1. The direct measurements are overall in good agreement with the SM prediction and $\Gamma_Z(\text{inv})$ obtained from the indirect lineshape measurements. The indirect $\Gamma_Z(\text{inv})$ measurements were also evaluated without assuming lepton universality which yields $497.4 \pm 2.5\,\text{MeV}$ [6].

Experiment	$\Gamma_Z(\text{inv})$ [MeV]
ALEPH	$450 \pm 34 \pm 34$
L3	$498 \pm 12 \pm 12$
OPAL	$539 \pm 26 \pm 17$
LEP Combination	503 ± 16
CMS	$523 \pm 3 \pm 16$
indirect LEP	499.0 ± 1.5
SM prediction	501.445 ± 0.047

Table 2.1: Summary of the direct $\Gamma_Z(\text{inv})$ measurements at LEP, the (in-)direct LEP combination, the direct CMS measurement, and the SM prediction including statistical and systematic uncertainties. For the LEP combinations and the SM prediction, only the total uncertainty is stated.

3 The ATLAS Experiment

The presented $\Gamma_Z(\text{inv})$ measurement is based on proton-proton collision data produced by the Large Hadron Collider (LHC) and collected by the ATLAS experiment in 2015-2016 at a centre-of-mass energy of 13 TeV. The following description of the LHC as operating during Run 2 is mainly based on [45–47] whereas the discussion of the working principle of the ATLAS experiment (Section 3.2) and in particular its sub-detectors mainly follows [48].

3.1 The Large Hadron Collider

The LHC is a particle accelerator located at CERN[1], 45 to 170 meters below the surface in Switzerland and France in the Geneva area. The accelerator complex is situated in the same 26.7 km long tunnel which hosted the predecessor, the Large Electron-Positron Collider (LEP).

In 2015 and 2016 proton-proton collisions with a centre-of-mass energy of 13 TeV were produced which were already in reach of the originally designed 14 TeV, following the previous runs at 7, and 8 TeV. These are amongst the highest collision energies ever reached in a laboratory particle accelerator and are only exceeded by collisions during Run 3 where the energy is raised to 13.6 TeV.

The accelerator consists of eight arcs intersected by eight straight parts. A 'twin-bore' magnet design is used as the tunnel is rather narrow in the curved sections. In this setup, the two rings, in which the two proton beams circulate in opposite directions, share the same return yoke and cryostat. The proton beams are kept on their trajectory by 1232 main superconducting dipole magnets cooled to 1.9 K with liquid helium producing a magnetic field of up to 8.33 T. The 392 main quadrupole magnets focus the beams close to the four interaction points where the two beams cross and the main LHC experiments are placed.

ATLAS and CMS[2] [49] are two multi-purpose detectors which were designed to dis-

---

[1] **C**onseil **e**uropéen pour la **r**echerche **n**ucléaire

[2] Compact Muon Solenoid

cover the Higgs, which was successfully achieved in 2012 [31, 32], and to search for physics beyond the SM. LHCb[3] [50] is specialised in rare hadron decays involving $c-$ or $b-$quarks in particular in the regard of CP violation, whereas ALICE[4] [51] focuses on studying the formation and the properties of the quark-gluon plasma when heavy ions instead of protons are collided in the LHC.

Several filling cycles are required to reach the designed 2808 bunches each containing 1.15×10^{11} protons to supply a sufficient number of collisions to the experiments. In Linac2 protons from a bottle of hydrogen gas, from which the electrons are stripped off via an electric field, are accelerated to 50 MeV and fed into the Proton Synchrotron Booster. There four separate rings accelerate the protons to 1.4 GeV. The Proton Synchrotron (PS) increases the proton energies up to 26 GeV before the Super Proton Synchrotron (SPS) accelerates them further to 450 GeV and injects them into the LHC where they are finally brought to 6.5 TeV via superconducting radio frequency cavities. The PS introduces the bunch structure of the proton beams with a 25 ns bunch spacing. The accelerator chain is sketched in Figure 3.1.

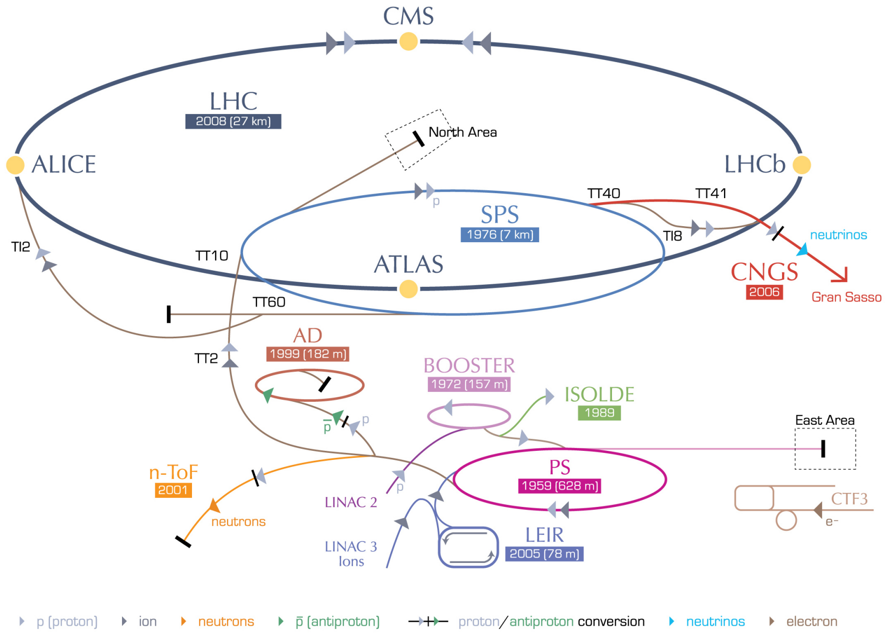

Figure 3.1: Sketch of the accelerator complex at CERN. Protons are pre-accelerated by the LINAC2, BOOSTER, PS and SPS before they are filled into the LHC. Figure adopted from [52].

---

[3] Large Hadron Collider beauty

[4] A Large Ion Collider Experiment

The number of produced events of a specific process is given by the product of the time-integrated instantaneous luminosity $\mathcal{L}_{\text{int}}$ and the corresponding cross section σ. Assuming a Gaussian beam profile the instantaneous luminosity is defined as

$$\mathcal{L} = \frac{n_b N_1 N_2 f_{\text{rev}}}{4\pi\sigma_x\sigma_y} F \ , \tag{3.1}$$

where n_b is the total number of interacting bunches, $N_{1,2}$ are the number of particles in each bunch, f_{rev} is the revolution frequency of 40 MHz and the beam sizes in the horizontal and vertical directions $\sigma_{x/y}$ give a measure of the beam area. F is a geometrical reduction factor as the two beams do not collide heads-on but under a crossing angle at the interaction point to avoid unwanted collisions along the shared beam pipe. The integrated luminosity is given by the time integral of the instantaneous luminosity

$$\mathcal{L}_{\text{int}} = \int \mathcal{L} dt \ . \tag{3.2}$$

The peak luminosity of $1.3 \times 10^{34}\,\text{cm}^{-2}\text{s}^{-1}$ exceeds the designed luminosity by 30% [53] even if the design number of bunches with a maximum of 2208 colliding bunches in 2016 containing 1.1×10^{11} protons is not reached. This is achieved by the introduction of a new bunch production scheme [54] which allows a significant improvement of the transverse beam emittance [55].

The high luminosity results in an average of 25.1 collisions taking place within the same bunch crossing in 2016. The separation of particles from the hard-scatter interaction from the additional so-called in-time pile-up collisions is a challenging process in the event reconstruction. Collisions in the previous or the following bunch crossing can distort the reconstructed event (out-of-time pile-up) as the readout of some detector components requires some time.

3.2 The ATLAS Detector

The design of the ATLAS detector is driven by the goal to discover the Higgs which mainly relies on an excellent photon, electron, and muon reconstruction. Searches for potential physics beyond the SM often require a precise measurement of $E_{\text{T}}^{\text{miss}}$. This makes a good jet resolution necessary, along with a reliable vertex reconstruction to ensure pile-up suppression. Among other requirements, this is achieved by a sufficient rapidity acceptance based on an almost full 4π coverage. The high particle multiplicity in a single event necessitates a finely grained detector which withstands large amounts of radiation. This results in a detector with a length of 44 m, a diameter of 25 m and a weight of roughly 7000 tonnes with several different detector components arranged around the beam pipe as shown in Figure 3.2.

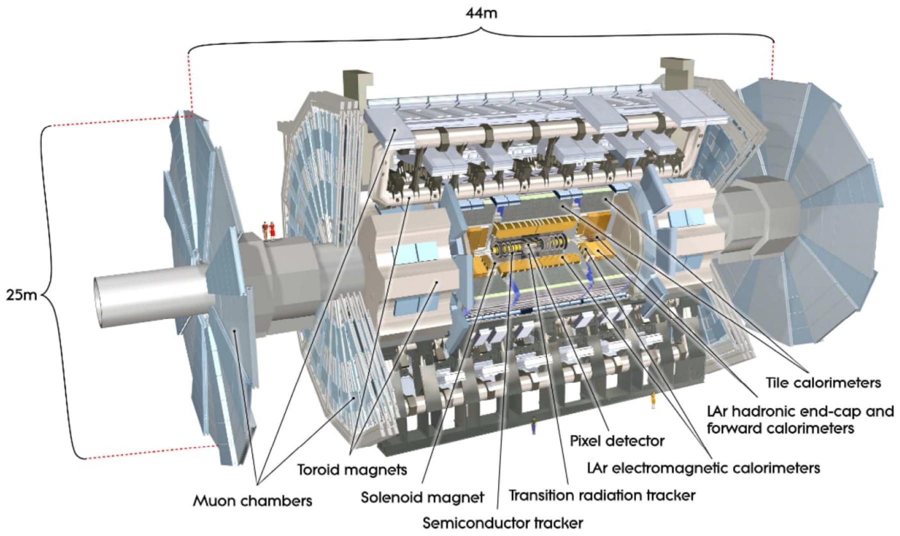

Figure 3.2: Sketch of the ATLAS detector and its sub-systems the inner detector, the calorimeters and the muon spectrometer listed from the interaction point outwards [48].

The sub-detector closest to the interaction point is a multilayered tracking detector to reconstruct primary and secondary vertices as well as to measure the momenta of charged particles. This inner detector (Section 3.2.1) is embedded in a 2 T magnetic field provided by an enclosing solenoid magnet. An electromagnetic calorimeter (Section 3.2.2) is responsible for measuring the energies of photons and electrons whereas the main task of the hadronic counterpart (Section 3.2.2) is to measure the energies of jets. The analysis of the particle shower shapes, as well as isolation variables, facilitates particle identification. The calorimeters are surrounded by one barrel and two end-cap superconducting toroid magnets each consisting of eight coils. These three magnets provide the necessary field to ensure adequate muon identification and momentum resolution in the muon spectrometer (Section 3.2.3) which builds the outermost detector layer.

A fast and efficient trigger system (Section 3.2.4) is required to handle the high rate at which the LHC provides collisions. A combined two layered hardware and software based trigger system ensures a high reconstruction efficiency of events even with low transverse momentum objects while keeping the background at an appropriate rate.

A right-handed coordinate system with its origin at the nominal interaction point is introduced to describe the kinematics of particles traversing the detector. The corresponding x- and y-axis span a plane transverse to the beamline along which the z-axis is defined. The x-axis points towards the centre of the LHC ring while the y-axis points upwards. The azimuthal angle ϕ around the z direction and the polar angle θ, being the angle relative to the beamline, are more frequently used due to the cylindrical geometry of the detector. The angle θ is often parameterised as the pseudorapidity defined as $\eta = -\ln\tan\left(\frac{\theta}{2}\right)$ or the rapidity $y = \frac{1}{2}\ln\frac{E+p_z}{E-p_z}$ in case of massive particles. The pseudorapidity is often preferably used as $\Delta\eta$ is Lorentz invariant under boosts along the z-axis. The angular distance between two particles in the $\eta - \phi$ plane is hence defined as $\Delta R = \sqrt{\Delta\eta^2 + \Delta\phi^2}$. The transverse momentum, p_T, and the missing transverse momentum, $E_\mathrm{T}^\mathrm{miss}$, are the respective projections into the $x - y$ plane.

3.2.1 The Inner Detector

The inner detector focuses on track reconstruction and momentum measurements of charged particles, primary and secondary vertex reconstruction as well as electron identification. This can be achieved through a combination of a pixel detector and a semiconductor tracker (SCT) spanning up to $|\eta| < 2.5$. These have a fine granularity to cope with the high particle event density, and a transition radiation tracker (TRT) in which charged particles leave curved tracks, due to the 2 T magnetic field inside the inner detector. The corresponding hits within $|\eta| < 2.0$ aid the particle identification. A compromise needs to be found between the mechanical structure holding this 7 m long and 2 m in diameter detector in place and a low material budget required for high reconstruction precision. For noise suppression, the pixel detector and the SCT need to be cooled down to −10 °C. The arrangement of the three sub-detectors is shown in Figure 3.3.

With the installation of the Insertable B-Layer (IBL) [56] the pixel detector consists out of four layers in the barrel surrounding the beamline and end-caps where the pixels are attached to disks. These silicon pixels are $50 \times 400\,\mu\mathrm{m}^2$ in $R - \phi, z$ enabling the highest accuracy of $10 \times 115\,\mu\mathrm{m}^2$ with which the position of tracks can be measured within ATLAS. This is further improved by the IBL which has a reduced pixel size of $50 \times 250\,\mu\mathrm{m}^2$. The pixel detector is closest to the beam and therefore enables precise secondary vertex reconstruction of particles which either decay or interact with the detector material.

A track traverses typically eight microstrip layers with daisy chained sensors attached.

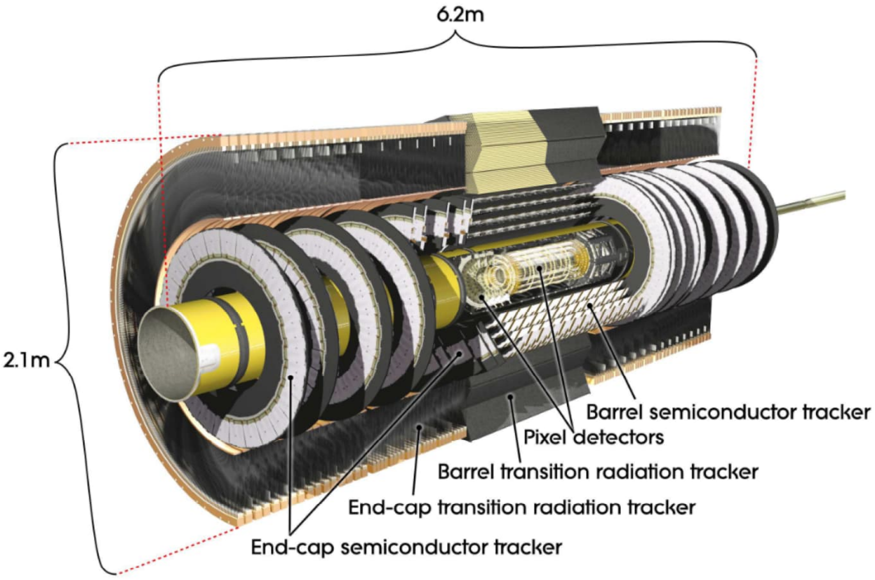

Figure 3.3: Schematic of the inner detector [48].

In the barrel, one set of strips runs parallel to the beam axis in each layer. Combined with stereo strips with an angle of 40 mrad they can measure $R - \phi$ at an accuracy of 17 µm and z with a precision of 580 µm. The SCT is completed by radially arranged strips in the end-caps and another set of stereo strips tilted by 40 mrad. This arrangement of the SCT improves the measurement of the impact parameter and the τ identification.

The TRT is constructed from straw tubes filled with a xenon gas mixture. These tubes have a diameter of 4 mm which provide a $R - \phi$ resolution of 130 µm per straw. These straws are split into two parts which in total are 144 cm long and run parallel to the beamline outside the SCT. At the end-caps, the straws run radially. The poorer precision with which the tracks are reconstructed in the TRT is compensated by the longer track length in combination with a larger number of hits. Electron identification can be achieved within the TRT by the detection of photons within the straw tubes which are produced by the interaction of the electrons with the transition radiation material.

The complementary interplay of the three sub-detectors ensures reliable track pattern recognition and position measurements.

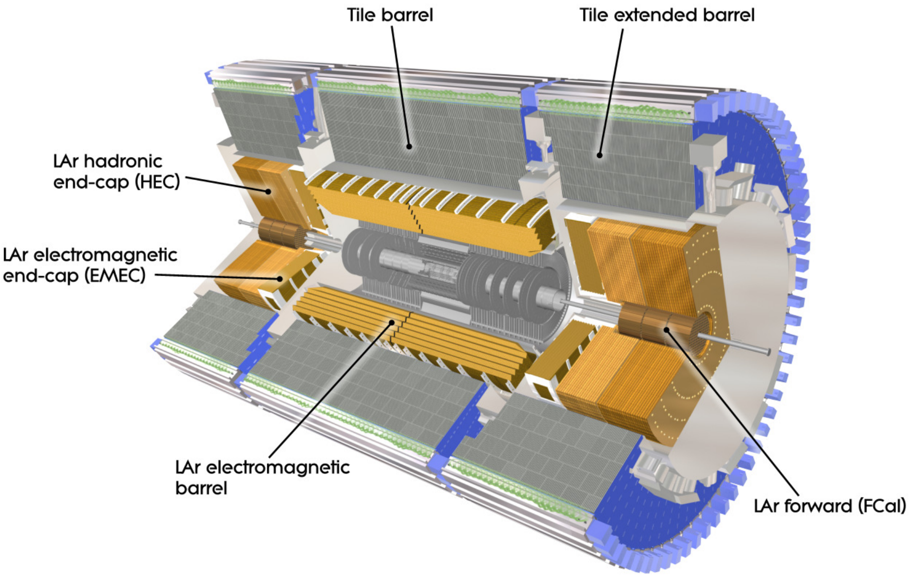

Figure 3.4: Schematic of the calorimeter system [48].

3.2.2 Calorimeters

The calorimeter consists of two sampling calorimeters using different absorbers and active materials to measure the energies of particles passing through the detector. The electromagnetic calorimeter builds the layer behind the solenoid magnet. Its fine granularity in the η coverage of the inner detector ensures a high resolution of electron and photon showers which are typically narrower than jet showers. The hadronic calorimeter has a coarser segmentation which is sufficient for jet and $E_{\mathrm{T}}^{\mathrm{miss}}$ reconstruction. Both calorimeters are symmetric in ϕ and are separated in a barrel, several end-cap disks, and a forward calorimeter to provide a hadronic coverage up to $|\eta| < 4.9$. An overview of the calorimeter layout is presented in Figure 3.4. The electromagnetic calorimeter has a depth of at least 22 radiation lengths (X_0) and hadrons need to pass material with a thickness of 11 interaction lengths (λ) around $|\eta| = 0$ to avoid particle showers reaching the muon system.

In the electromagnetic and partially in the hadronic calorimeter liquid argon (LAr) cooled to $-184\,^{\circ}\mathrm{C}$ is used as the active material due to its radiation hardness and its linear and stable response.

The Electromagnetic Calorimeter

The electromagnetic sampling calorimeter measures energy deposits in the active LAr enclosed by the absorber layers with a high spatial resolution up to $|\eta| = 3.2$. The showers are enforced by lead absorber plates which have an accordion shape and are interleaved with copper and kapton electrodes. The 2.1 mm drift gaps between the plates are filled with LAr which is ionised by traversing particles. High voltage is applied to the electrodes to measure electric currents which depend on the amount of ionisation. The thickness of the absorber is optimised regarding the energy resolution and the accordion shape ensures a symmetry in ϕ resulting in a flat resolution along ϕ.

The barrel is constructed from two 3.2 m long and 53 cm thick cylinders which are separated by 4 mm at $|\eta| = 0$ and reaches up to $|\eta| = 1.475$. Two end-caps with a diameter of roughly 4 m consist of an inner and an outer wheel measuring energy deposits in a range of $1.375 < |\eta| < 3.2$ where the outer wheel ($1.375 < |\eta| < 2.5$) overlaps with the barrel. For $|\eta| < 2.5$ the calorimeter has three layers. The first so-called strip layer is very narrow in η to enable a precise position measurement and discrimination of photons and $\pi^0 \to \gamma\gamma$. The second layer is the thickest layer ($\sim 16\,X_0$) containing the largest fraction of the electromagnetic shower (f_{em}). Each cell in the second layer has a typical size of $\Delta\eta \times \Delta\phi = 0.025 \times 0.0245$ where the resolution in ϕ is improved by a factor of four but reduced by a factor of up to eight in η compared to the first layer. For the third layer, two cells are combined along η which is sufficient for the tails of the showers. An active LAr layer in front of the first layer corrects for a potential energy loss of particles showering already in front of the electromagnetic calorimeter for $|\eta| < 1.8$. The transition region between the barrel and the end-caps at $1.37 < |\eta| < 1.52$ contains more passive material besides a coarser granularity resulting in an exclusion of electrons reconstructed in this η range. The design energy resolution of $\frac{\sigma_E}{E} = \frac{10\%}{\sqrt{E}} \oplus 0.7\%$ enables excellent electron and photon energy measurements.

The Hadronic Calorimeter

The hadronic calorimeter can be separated into a central (5.6 m), two extended barrels (2.6 m), and two LAr end-cap wheels placed behind the electromagnetic end-caps. Showers of hadronic particles, which are not stopped within the electromagnetic calorimeter are measured with scintillating tiles in the barrels where the showers are generated through steel absorbers.

The central barrel can measure energy deposits within $|\eta| < 1.0$ whereas the extended barrels cover $0.8 < |\eta| < 1.7$. All three barrels are divided in the azimuthal direction into 64 modules providing a 0.1×0.1 spatial granularity in $\eta \times \phi$. The three layers of the scintillating tile calorimeter have a depth of $9.7\,\lambda$ in the centre of the central barrel spanning from an inner radius of 2.28 m to 4.25 m. Photons produced by the traversing particle showers are transported via wavelength shifting fibres and are read out via photomultiplier tubes on two sides of the tiles.

The two end-caps, which range from 1.5 to 3.1 in $|\eta|$, overlap with the tile and forward calorimeters to ensure a smooth transition between the three detector systems. They are segmented into 32 wedges and two layers with copper plates intersected by LAr and have an inner (outer) radius of 0.47 (2.03) m.

The design resolution of the hadronic calorimeter of $\frac{\sigma_E}{E} = \frac{50\%}{\sqrt{E}} \oplus 3\%$ is sufficient for the jet and $E_{\mathrm{T}}^{\mathrm{miss}}$ energy measurements even if it is lower than for the electromagnetic calorimeter.

The Forward Calorimeter

The forward calorimeter (FCal) relies on LAr in three end-caps on each side of the barrel to measure particles in the forward direction. Copper is used as an absorber for the electromagnetic wheel whereas the two hadronic wheels use tungsten leading to a combined thickness of $10\,\lambda$. A high density is required as the FCal is placed further away from the interaction point compared to the electromagnetic end-cap to suppress the ability of neutrons to backscatter into the inner detector. The electrodes are constructed from rods and tubes running along the $z-$axis where LAr is filled into the gaps between the rods and the tubes. As the FCal is the calorimeter closest to the beam it has a coverage of $3.1 < |\eta| < 4.9$ with a designed resolution of $\frac{\sigma_E}{E} = \frac{100\%}{\sqrt{E}} \oplus 10\%$.

3.2.3 The Muon Spectrometer

Muons do not interact strongly and are about a factor of 207 heavier than the electron and are therefore the only particles besides neutrinos in the SM which are not stopped within the calorimeters. This makes an additional sub-detector necessary which is placed around the calorimeters in which only muons are expected to leave signatures.

The muon spectrometer is composed of high precision tracking chambers and trigger chambers with a fast readout. The air-core toroid barrel and end-cap magnets provide a strong muon bending power of 1.5-5.5 Tm ($|\eta| < 1.4$) and 1-7.5 Tm ($1.6 < |\eta| < 2.7$) and a slightly lower field strength in the transition region ($1.4 < |\eta| < 1.6$) between the two magnet systems. The magnetic field is orthogonal to the muon trajectories. The arrangement and design of the three magnets minimises multiple scattering ensuring a high track resolution.

Monitored drift tubes (MDTs) and cathode strip chambers (CSCs) measure the spatial track coordinates. In the barrel chambers, these are placed in a cylindrical shape around the beam axis in three layers at 5, 7.5 and 10 m from the beamline where each layer is split into two sets of in ϕ slightly overlapping octants. The end-caps also feature three layers perpendicular to the beam axis in four wheels on each side where the big wheel is 21.5 m away from the interaction point.

The MDTs consist of 3-8 layers of 30 mm drift tubes filled with an $\mathrm{Ar/CO_2}$ gas mixture and a 50 µm thick tungsten-rhenium wire. The non-linearity of the gas mixture at high rates leading to a reduced spatial resolution is compensated by its ageing resistance. The resolution of 80 µm per tube in the main bending direction of the magnetic field yields a combined chamber resolution of 35 µm. This resolution is below the threshold of 50 µm anticipated to measure a 1 TeV muon track with a precision of 10% using solely the muon spectrometer which is designed to be capable of measuring muons with p_{T} as low as 3 GeV. The p_{T} resolution is mainly limited by multiple scattering for muons with a momentum in the range of 30-200 GeV as they must pass through roughly 1.3 X_0. Only a single track per chamber is allowed to successfully match the transverse coordinate measured by the trigger chambers to the MDT measurement.

The CSCs are used in the first layer for $2.0 < |\eta| < 2.7$. They are essentially multi-wire proportional chambers with strip cathodes. Four measurements of the $\eta - \phi$ coordinates can be performed with a precision of 60 µm where the transverse resolution is 5 mm as the four planes in each of the two disks are arranged orthogonal to each other. The higher granularity allows coping with the higher rate and backgrounds in the more forward direction where a pulse height matching enables the measurement of more than one track per chamber.

Resistive plate chambers (RPCs), a with gas filled parallel electrode plate detector, can resolve signals within a spread of less than a bunch crossing. They are hence responsible for triggering muon signals in the barrel surpassing a certain p_{T} threshold as well as for the bunch crossing identification. They also enable a measurement of the coordinate ϕ orthogonal to the bending plane as a track passing all three stations allows six measurements of η and ϕ. The thin gap chambers (TGCs) take over this role in the end-cap region ($1.05 < |\eta| < 2.4$) as they are less impacted by neutron and converted photon radiation and can deal with higher rates as they are following the multiwire proportional chamber design. A coincidence principle in both trigger chamber types is used for background reduction.

An overall challenge in the muon spectrometer is the necessary exact alignment of the chambers and layers which is achieved by 12000 optical alignment sensors. The homogeneity of the magnetic field is monitored by 1800 Hall sensors.

A speciality of the muon spectrometer compared to the other sub-detectors is that the barrel has a gap of up to 2 m (± 0.08 in η) in the centre of the barrel for maintenance of the other systems. A different reconstruction algorithm is hence required to identify those very central muons.

3.2.4 The Trigger System

A two-level trigger system [57] is responsible for reducing the 40 MHz rate at which particle collisions take place in the ATLAS detector to about 1 kHz at which the detector information of about 1.5 MB per event can be saved in the permanent storage. The Level-1 trigger is hardware based as a trigger decision has to be taken within 2.5 µs after the bunch crossing to stay within the buffer time available in the read-out system. At this stage reduced calorimeter information and signals from the muon trigger chambers are analysed to reduce the rate to about 100 kHz at which the software-based High-Level Trigger (HLT) can operate. The aim is to identify high p_{T} muons, electrons, photons, hadronic taus and jet candidates as well as global observables such as $E_{\mathrm{T}}^{\mathrm{miss}}$.

About 190.000 calorimeter cells are combined to 7168 trigger towers containing up to 60 cells and with a size of 0.1×0.1 in $\eta \times \phi$ in large parts of the detector with increasing size in the forward direction. The LAr calorimeter signals have bipolar pulses with a width of up to four bunch crossings and a long undershooting tail which makes them sensitive to pile-up. The tower signals are calibrated via receiver boards and are digitised as well as synchronised in the Level-1 calorimeter PreProcessor [58]. These signals are further propagated through an autocorrelation finite impulse response filter and dynamically corrected for pile-up to identify the correct bunch crossing via a peak finding algorithm and to convert the filter output via dedicated look-up tables into E_{T} while applying noise cuts. In cases where the look-up table is saturated, the Level-1 trigger decision is directly fulfilled by sending out a 'Level-1 Accept'.

The PreProcessor sends the calibrated trigger tower information in parallel to the Cluster Processor (CP) and the Jet/Energy-sum Processor (JEP). The CP searches for electrons, photons and hadronic decaying taus passing predefined momentum thresholds whereas the JEP identifies jet candidates and measures $E_{\mathrm{T}}^{\mathrm{miss}}$ as well as the total transverse energy. In the CP isolation requirements can be requested alongside a hadronic veto. A sliding window algorithm is employed for electrons and photons to identify a local energy maximum of 2×2 trigger towers in the electromagnetic calorimeter and similarly for $\Delta R = 0.4$ jets with combined electromagnetic and hadronic towers.

The number of trigger objects over the predefined energy thresholds is directly sent to the Central Trigger Processor (CTP). Additionally, these objects are provided to the Level-1 Topological Processor which analyses the event topology.

The Level-1 muon trigger is based on coinciding hits in the RPC and TGC trigger chambers. The trajectories of muons constructed from their interaction points and their hits in the trigger chambers are compared to p_{T} dependent predicted trajectories. This allows the determination of the muon p_{T} in certain p_{T} ranges. The number of muons in every p_{T} interval is sent to the CTP.

The CTP then combines the information from the calorimeter, muon and the topological Level-1 triggers and compares them to up to different 512 trigger menus encoded in look-up tables. The final trigger decision is a logical or of all trigger items. The particle candidates identified by the Level-1 trigger are sent with their η and ϕ coordinates as well as the passed thresholds as seeds to the HLT in case of a positive trigger decision. The HLT runs dedicated trigger algorithms, which are often similar to the reconstruction algorithms but faster, on approximately 40.000 CPUs to take a final decision if the event has interesting enough characteristics to get stored. The algorithms usually take a few hundred milliseconds but can reach seconds if the event topology is very complex. The full calorimeter and muon spectrometer granularity is taken into account to reach a higher p_{T} threshold resolution, and the inner detector information is considered to be particularly helpful for particle identification.

At both the Level-1 trigger and the HLT certain event topologies fulfilling specific trigger criteria would cause very high rates way beyond what is still manageable by the read-out system and data storage. As these events can be of interest so-called prescales are introduced to only allow a fraction of the events to fire the trigger. The primary single electron and $E_{\mathrm{T}}^{\mathrm{miss}}$ triggers used in this analysis are unprescaled.

4 Monte Carlo Event Generation

A comparison of the measured distributions with theoretical predictions relies on the generation of events via Monte Carlo (MC) simulations which is described in this chapter. MC simulations of the studied processes are required to interpret the data and to derive estimates for various backgrounds contributing to the defined phase spaces. Moreover, these MC simulations are used to correct the data for detector effects. Hence accurate modelling of the hard physics process as well as the propagation of the produced particles in the detector, including interactions and decays, is of uttermost importance. A precise knowledge of the interplay between the particles and the detector components is also necessary. This enables a parallel reconstruction of data and MC simulations from real and modelled detector signals. The following chapter is based on [39, 59, 60].

A consequence of the running of the strong coupling is that only parts of QCD can be derived from a perturbative quantum field theory. An example of such a calculable quantity is the matrix element at fixed order in α_s. The consideration of real emissions of jets which influence the final state topology, the virtual loop corrections determining the normalisation of the cross section as well as further corrections such as hadronisation or the underlying event drastically complicates the event generation. Collinear factorisation allows a separation into a perturbative short distance part and a long distance part for which phenomenological models and comparisons to data are necessary. For the cross section of a proton-proton collision this factorisation can be expressed as

$$\sigma = \sum_{a,b} \int_0^1 dx_a dx_b \sum_n d\Phi_n f_a\left(x_a, \mu_F\right) f_b\left(x_b, \mu_F\right) d\hat{\sigma}_{a,b\rightarrow n}\left(\Phi_n; \mu_F, \mu_R\right) \ . \tag{4.1}$$

The colliding protons contain alongside their three valence quarks gluons which can create pairs of so-called sea quarks. Parton distribution functions (PDFs) $f_a\left(x_a, \mu_F\right)$ state in a simple picture the probability to find a parton of type a with a momentum fraction x_a within the proton at the factorisation scale μ_F. They incorporate the long distance part of the interaction and are determined by fits to data mostly obtained from fixed target deep inelastic scattering experiments but also including data from colliders. The evolution of the PDFs to higher energy scales is described by the DGLAP equations [61–63] whereas the momentum fractions are determined experimentally.

The differential phase space of the n final state particles is expressed as $d\Phi_n$. The differential parton level cross section depends in addition to Φ_n on the factorisation scale, μ_F, and the renormalisation scale, μ_R, and can be expressed as $d\hat{\sigma}_{a,b\rightarrow n} = \frac{1}{2\hat{s}_{ab}} \left|\mathcal{M}_{ab\rightarrow n}\right|^2$. Here the parton flux $1/\left(2\hat{s}_{ab}\right) = 1/\left(2x_a x_b s\right)$ is a function of the centre-of-mass energy squared, s, of the two protons. The matrix element $\mathcal{M}_{ab\rightarrow n}$ is squared and averaged over colour and spin of the initial state partons. For the calculation of the hard process, this matrix element is evaluated at a fixed order in an expansion in α_s. The lowest order includes neither real emissions nor virtual corrections and is called the leading order which is often equal to the tree-level.

Monte Carlo integration becomes the fastest integration method for higher dimensions which can rise rapidly as every real emission contributes an additional three dimensions to the integration. The corresponding statistical error simply scales with the number of generated events $1/\sqrt{N}$. A special phase space sampling is needed to ensure convergence of the integration in case of a high number of real emissions due to the non-uniformity of the corresponding matrix element. The produced jets need to be hard and angularly separated from each other to avoid soft and collinear singularities which lead to infinite cross sections. Next-to-leading-order calculations including loops are often necessary as the leading order approximations cannot determine the correct normalisation sufficiently accurate. Cancellations of the divergent loop amplitudes against divergences of unresolved real emissions become important when higher orders are considered.

There exists no unique factorisation scale μ_F. In a Z+jets topology, several valid scale choices can be justified ranging from the lowest to the highest possible momentum combination of the final state particles. The dependence of the cross section on the scale drops with the inclusion of additional orders and vanishes in the limit where all orders are considered. Typically the scales are chosen such that $\mu_F = \mu_R$ and are set to the scale of the hard interaction. To take this arbitrary choice into account the scales are often varied up and down by a factor of two to derive a corresponding scale uncertainty.

Following the hard matrix element evaluation a parton shower is simulated to recover the higher order emissions which have been dropped in the fixed order calculation. The parton shower adds splittings of quarks as well as gluons. The quarks radiate gluons which in turn split either into quark-antiquark pairs or gluon pairs. These splittings can occur prior to the collision, where they are referred to as initial-state radiation, or take place after the hard interaction, where they are called final-state radiation. Soft or collinear emissions cause divergences which need to be cancelled by equal, opposite sign singularities in the virtual loop corrections. This can be achieved by considering the Sudakov factors which describe the probability of the absence of a splitting during the evolution from one scale to another scale. The splitting is stopped as soon as the scale evolution reaches the hadronisation scale about the order of 1 GeV. A matching or merging procedure needs to be incorporated into the MC simulation chain to avoid double counting of certain phase space configurations which can be populated either by the matrix element calculation or by the parton shower.

At these low energy scales reached after the parton shower, the partons need to form colour-neutral states due to colour confinement. This process is known as hadronisation and needs to be described by phenomenological models as perturbative QCD can no longer be applied. The two most prominent models of the formation of hadrons are the string model [64] and the cluster model [65]. As not all the formed hadrons are stable potential hadron decays need to be considered. Their respective decays are often derived using the corresponding branching ratios taken from external measurements summarised by the PDG [1] whereas the kinematics of the decay products tend to be calculated via matrix elements.

QED radiation is either modelled by the QCD parton showers or alternatively by the Yennie-Frautschi-Suura formalism [66] in which soft photons are resummed. Depending on the generator the radiated photons are either stable or can in turn produce electron-positron pairs via pair production leading to particle cascades.

Alongside the hard interaction, softer collisions of the remaining partons of the colliding protons can take place which also undergo parton showers. These can typically be described within the framework of perturbative QCD and are called multiple parton interactions. Another effect which has to be taken into account is that also the remnants of the protons will hadronise. Both effects are summarised in the underlying event and are important to be modelled as they can for example change the particle multiplicity. The underlying event should not be confused with pile-up which is defined as the mean number of interactions per bunch crossing and arises at the LHC due to several interactions taking place simultaneously. Pile-up is simulated in the digitisation step of the detector simulation. The MC simulations are later reweighted to match the pile-up profile in the data to ensure a consistent event and object reconstruction efficiency [67].

A tuning of the free parameters which cannot be derived from first principle is required. The large dimensionality of the parameter space makes a separation into subsets of tuneable parameters necessary which are successively tuned either by hand or by using dedicated tools fitting the predictions to selected reference data.

GEANT4 [68, 69] is used to model the interactions of the generated particles with the detector. The energy deposits generated by the detector simulation and a subsequent digitisation simulation enable a common event reconstruction of data and simulated events. The so-called 'truth information' contains the information of the particles from the hard-scattering, the parton shower and the hadronisation as well as their development within the detector simulation with the therein produced particles. This information is stored as the 'truth record' alongside the digitised event information which has a similar format as the data. This state defines the detector level in contrast to the particle level which referrers to events after the parton shower and the QED radiation.

Four different MC generators are used within this analysis for various purposes. Sherpa [70] provides the estimates of the SM backgrounds besides processes involving top quarks. These are modelled with Powheg [71–73] which relies on the Pythia [74] parton shower. The nominal detector correction is performed with Sherpa. MadGraph5_aMC@NLO [75] is used to derive an alternative detector correction. A theory correction of the off-shell photon contribution is calculated with Pythia. Both Sherpa and MadGraph5_aMC@NLO provide SM predictions of R^{miss} for both channels to which the measurements are compared.

An overview of the signal and background samples used in the presented Γ_Z(inv) analysis including the corresponding generator and parton shower is given in Table 4.1. The Sherpa samples are produced with their own tune whereas the other samples are constructed with the A14 tune [76]. The NNPDF3.0nnlo PDF set [77] is used for all samples besides MadGraph5_aMC@NLO which uses the NNPDF3.1nnlo [78] and the top samples which are built with the NNPDF3.0nlo [77] set. More details on the generation of the V+jets signal samples can be found in [79].

Process	Generator	Parton shower
QCD V+jets (nominal)	Sherpa v2.2.11	Sherpa v2.2.11
QCD V+jets (alternative)	MadGraph5_aMC@NLO 2.6.5	Pythia 8.240
Electroweak V+jets	Sherpa v2.2.11	Sherpa v2.2.11
Diboson semileptonic (VV)	Sherpa v2.2.1	Sherpa v2.2.1
Diboson fully leptonic (VV)	Sherpa v2.2.2	Sherpa v2.2.2
Triboson (VVV)	Sherpa v2.2.2	Sherpa v2.2.2
Single-top: s-channel, Wt	Powheg-Box v2	Pythia 8.230
Single-top: t-channel	Powheg-Box v2	Pythia 8.230
$t\bar{t}$	Powheg-Box v2	Pythia 8.230

Table 4.1: Simulated signal and background samples used in the Γ_Z(inv) analysis with the underlying generators and parton showers.

5 Object Reconstruction

Particles originating from LHC collisions in the ATLAS detector leave signatures in different parts of the detector depending on their particle type. The signals in the subdetectors are combined to reconstruct particle candidates. The reconstruction is optimised for every particle type individually. The particle identification needs to be balanced between the rejection of objects coming from other sources and the preservation of a high classification rate for the correct particle type. Different working points are provided by the ATLAS combined performance group for the identification of objects which apply stronger or looser criteria and can be used depending on the requirements of the analysis. Several detector effects can cause differences in the reconstructed particle properties compared to the actual true particle properties. These can for example be the non-compensating calorimeter response to hadronic jets resulting in their energies being systematically measured too small as the neutral jet component dominated by neutrons deposit only small amounts of energy, detector noise or resolution effects. These detector effects are corrected by calibration procedures which are typically derived based on simulations and in-situ measurements which compare the data to simulations. Dedicated algorithms are implemented in the ATLAS software framework Athena [80] which reconstruct the detector signals to physical objects. The same algorithms are used for data as well as for simulated events to not introduce differences due to the object reconstruction approach.

Reconstruction, identification, and calibration of the objects relevant for the $\Gamma_Z(\text{inv})$ measurement are presented within this chapter based on the cited ATLAS performance papers beginning with jets (Section 5.1), followed by electrons (Section 5.2), muons (Section 5.4), hadronically decaying taus (Section 5.5) and missing transverse momentum (Section 5.6).

5.1 Jets

Quarks and gluons produced in a collision at the LHC form colour-neutral states due to colour confinement. This process is called hadronisation in which mesons and baryons are formed in a cone, the so-called jet. Jets are only well defined if their constructing algorithms fulfil two requirements. The constituents clustered into the jet need to be independent of any additional soft radiation. This requirement is known as infrared safety. The number of jets needs to remain invariant under the addition of an additional collinear splitting in the fragmentation process. This is referred to as collinear safety [81].

The anti-k_t algorithm [81] is a sequential recombination algorithm which fulfils both requirements. Two distances are defined d_{ij} between an object i and an object j as well as d_{iB} between an object i and the beam. They are given by the following equations

$$d_{ij} = \min\left(\frac{1}{k_{t_i}^2}, \frac{1}{k_{t_j}^2}\right)\frac{\Delta_{ij}^2}{R^2} \ , \tag{5.1}$$

$$d_{iB} = \frac{1}{k_{t_i}^2}, \tag{5.2}$$

with the angular distance R and $\Delta_{ij} = (\phi_i - \phi_j)^2 + (y_i - y_j)^2$ where ϕ is the azimuthal angle, y the rapidity, and k_t the transverse momentum. Variants of this algorithm exist where the exponent of the transverse momentum k_t is either 2 (k_t algorithm) [82, 83] or 0 (Cambridge/Aachen algorithm) [84, 85] instead of -2 for the anti-k_t algorithm.

The anti-k_t algorithm starts with the determination of the closest distance between any two input objects including the distances to the beam. In the case where the smallest distance is between two objects, those will be clustered by adding their four-momenta into a new object which replaces them in the input collection. In the case where the smallest distance is the one between an object and the beam, the object will be identified as a jet and removed from the collection. This procedure continues until no objects are left in the input collection.

The distance d_{ij} between a soft and a hard jet constituent is driven by the momentum of the hard particle and their angular separation whereas the distance between two soft particles, which have a comparable angular displacement, have a larger overall distance. This ensures that soft particles cluster typically first with hard particles before they get combined with each other. Additionally, if a hard particle is only surrounded by soft particles within $2\,R$ those within a radius of R will be clustered onto the hard particle and form a conical jet in the azimuth-rapidity plane. Two hard objects are merged into one jet if the angular distance between them is smaller than the jet radius R.

The anti-k_t algorithm with a radius of $R = 0.4$ is used in this analysis and takes topological calorimeter clusters [86] and charged particle tracks as inputs to build so-called particle flow jets [87]. This is discussed in the following paragraphs.

Topological Calorimeter Clusters

The calorimeters allow a three-dimensional reconstruction of the shapes of particle showers from energy depositions in the calorimeter cells. The topo-clustering algorithm is seeded by cells exceeding the signal-to-noise ratio by four standard deviations. The noise is determined by the sum of squares of noise stemming from fluctuations of the baseline cell signals due to pile-up and electronic noise. Seed cells are iteratively expanded by adding all cells with energies twice the noise threshold. This expansion spans over the calorimeter layer in the lateral direction and over different calorimeter layers as long as they overlap in the $\eta-\phi$-plane. In a final step, all cells are added to the clusters adjacent to the selected cells. Clusters containing more than one seed cell can be split exactly once which is sufficient to differentiate between electromagnetic and hadronic showers.

An origin correction [88] is performed for every topo-cluster as jets are expected to originate from the primary vertex[1] [89] as they should be produced in the hard-scatter process.

Topo-clusters are in addition used for the reconstruction of electromagnetic objects such as electrons and photons and are calibrated to the electromagnetic scale matching the response of these particles. The topo-clusters of hadronic showers, therefore, need to be calibrated to the hadronic scale after the jet clustering.

Charged Particle Tracks

Charged particle tracks are reconstructed from the inner detector for the jet reconstruction. They are required to leave hits in the silicon detector and the pixel detector. The geometry of the inner detector prescribes a cut-off on their pseudorapidity of $|\eta| < 2.5$. Single track momenta need to fulfil $p_{\mathrm{T}} > 500$ MeV to suppress noise. A reduction of pile-up contributions is achieved by requiring the track and the primary vertex to be close. Tracks associated to electrons or muons fulfilling medium selection requirements are rejected for the reconstruction of jets. Tracks passing the above selections are fed into the sequential jet clustering algorithm [90].

Particle Flow Jets

The inclusion of tracks in the reconstruction of hadronic jets leads to a better momentum resolution as charged particle tracks with low transverse momenta can be measured

---

[1] The primary vertex is defined as the vertex with the largest $\sum_{\text{tracks}} p_{\mathrm{T}}^2$ which has at least two tracks with $p_{\mathrm{T}} > 500\,\mathrm{MeV}$ associated to it.

with a higher precision compared to the energy deposits in the calorimeter of the topo-clusters. The precision of the low transverse momenta tracks is due to the relatively large curvature of the particle tracks on which these particles traverse the detector as they are impacted by the magnetic field.

Moreover, the range of particles considered in the clustering is extended as they can be reconstructed for a transverse momentum of $p_{\mathrm{T}} > 500$ MeV where energy deposits in the calorimeter do not exceed the noise thresholds for seeding a topo-cluster. The angular resolution of particles reconstructed by the tracker can be more precisely measured than the one obtained from the calorimeters. An additional improvement is an increased suppression of charged particles originating from pile-up vertices.

The particle flow algorithm, therefore, combines the excellent momenta measurements of charged, low-energy particle tracks with the topo-clusters for neutral particles, highly energetic charged particles and particles going in the forward direction outside the tracking acceptance. Energy deposits from charged particles in the calorimeter are replaced by the tracks which are matched to the corresponding topo-clusters. The contribution from tracks is damped for larger track momenta and tracks with a momentum above 100 GeV are not considered as at such high energies the calorimeter energy measurement is expected to have higher precision than track momentum measurement [87, 88]. Tracks, topo-clusters, and combined objects are used in the jet clustering algorithm to reconstruct the jets and to calculate the soft activity of the event which is a constituent of the missing transverse momentum described in Section 5.6. The calibration of the reconstructed jets is described in the next section.

Jet Energy Scale Calibration

The reconstructed jet energy after the jet clustering differs significantly from the true jet energy. This can be studied in Monte Carlo simulations where the jet energy is derived by the same anti-k_t algorithm taking all stable final state particles except neutrinos and muons from the hard-scatter event as input. Several sequential calibration steps [88] are required as sketched in Figure 5.1.

Pile-up Correction

The dependence of the jet energy on both in-time pile-up from interactions in the same bunch crossing and out-of-time pile-up from either previous or subsequent bunch crossings can be reduced by a correction which depends on the jet area A and the event median p_{T} density ρ. The density is determined from central jets with $|\eta| < 2$ which are

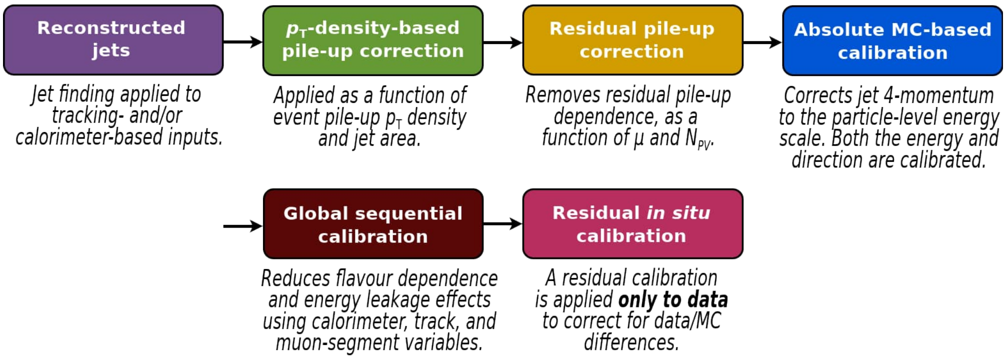

Figure 5.1: Jet energy scale calibration procedure for particle flow jets [88].

constructed by the k_t algorithm as here soft jets are formed first, which often have their origin in pile-up. The correction is applied as a scale factor on the jet four-momentum while leaving the direction of the jet unaffected. A residual pile-up dependence remains which depends on the number of primary vertices N_{PV} and the mean number of interactions per bunch crossing μ.

Jet Energy Scale and η Calibration

Isolated and truth matched ($\Delta R < 0.3$) reconstructed jets are used to derive a calibration factor to correct the jet energy scale (JES) for several effects. These include the non-compensating response of the calorimeter, effects due to non-active material and energy deposits leaking outside of the jet cone. In addition, a η calibration is applied to reduce biases stemming from discontinuities in the uniformity of the calorimeter technology and the changing size of the corresponding cells correcting the jet p_{T} and η. These corrections calibrate the jets to the PFlow+JES scale.

Global Sequential Calibration

The previous calibration steps are independent of the intrinsic properties of the jets such as the flavour, energy, and momentum distributions of the jet constituents. Quark and gluon initiated jets typically differ in their shower shapes and their particle compositions. Gluon jets usually produce more soft hadrons leading to wider but less deep showers than jets originating from quarks due to a larger colour factor. The global sequential calibration aims to improve the jet resolution while keeping the average jet energy response stable by reducing the dependence on the underlying jet structure. This is done by sequentially correcting several observables. Among others, these are the number and the width of tracks targeting the reduction of the dependence on the jet flavour, the relative distribution of energies in the different calorimeter layers, and the number of muon track segments correcting the punch-through of jets with high transverse momenta.

In-situ Calibration

In a final calibration step discrepancies between the MC simulation and the data are corrected via reference objects balancing the jet p_{T}. These non-accurate descriptions in the MC simulation chain can range from the hard-scatter interaction to the energy deposits of the particles in the detector. Therefore, the response $\mathcal{R} = \langle p_{\mathrm{T}}^{\mathrm{jet}}/p_{\mathrm{T}}^{\mathrm{ref}} \rangle$ is measured in data and in simulation and the corresponding double ratio $\mathcal{R}^{\mathrm{data}}/\mathcal{R}^{\mathrm{sim}}$ is considered as the correction factor. Central jets are used as a reference object to calibrate the energy scale of forward jets which is called the η-intercalibration as the following in-situ calibrations are only applicable to central jets. In Z+jet and γ+jet events, the calibrated Z boson and the photon balance the jet and the full hadronic recoil is taken as an input in the calibration to suppress pile-up and jet reconstruction threshold effects. A third recoiling reference object is a set of several already calibrated low p_{T} jets balancing one high p_{T} jet. The Z/γ+jet and the multijet in-situ calibrations are statistically combined to cover a range from 17 GeV to 2.4 TeV. The Z boson in the electron and muon decay channels drive the precision up to 500 GeV where this channel slowly runs out of statistics. The γ+jet calibration is the most important component in the intermediate range up to 1 TeV as the γ+jet cross section is about an order of magnitude larger than the Z+jet cross section [91]. The multijet balancing method dominates the combination for very high p_{T} jets as this process has the highest cross section [92].

Jet Energy Resolution

The jet energy resolution (JER) does influence the precision with which the jet energy is measured and can be described by the following functional form which is partially motivated by the calorimeter resolution

$$\frac{\sigma(p_{\mathrm{T}})}{p_{\mathrm{T}}} = \frac{N}{p_{\mathrm{T}}} \oplus \frac{S}{\sqrt{p_{\mathrm{T}}}} \oplus C\ . \tag{5.3}$$

Here N represents pile-up as well as electrical noise of the detector which is independent of the jet p_{T} and hence dominates the resolution at low p_{T}. The pile-up contribution to the noise is estimated using random cone measurements in unbiased data [88] whereas the electronic component is derived from pile-up free simulation samples. In the range from 30-400 GeV the stochastic (S) term mainly influences the JER due to statistical fluctuations of the energy deposits in the calorimeter. The energy resolution of high p_{T} jets is dominated by fluctuations scaling with p_{T} which are mainly energy deposits in inactive detector material, the starting position of the jet shower, and varying detector response due to different detector systems and geometry. The JER is extracted from the p_{T} asymmetry of the two jets in dijet events. A similar resolution in data and simulation is obtained by correcting the simulation samples to match the resolution in data. In the case where the resolution in the simulation is smaller than in the data. Otherwise, no correction is applied to the data to avoid degrading the data.

Jet Vertex Tagging

Rejecting pile-up jets is important to this analysis as the aim is to measure low $E_{\mathrm{T}}^{\mathrm{miss}}$ to profit from larger statistics and from better control of some of the systematic uncertainties where $E_{\mathrm{T}}^{\mathrm{miss}}$ can be influenced by pile-up. In particular, can a pile-up jet introduce an artificial momentum imbalance leading to $E_{\mathrm{T}}^{\mathrm{miss}}$ pointing in the opposite direction of this jet.

Pile-up jets in the central ($|\eta| < 2.4$) and forward ($|\eta| > 2.5$) region are identified by two specialised jet vertex taggers which do not differentiate between in- and out-of-time pile-up. The jet vertex tagger (JVT) [93] combines two tracking observables to differentiate between central hard-scatter jets and pile-up jets.

The first variable of the multivariate combination is the pile-up corrected jet vertex fraction. The jet vertex fraction is defined as the p_{T} scalar sum of tracks of the jet associated to the hard-scatter vertex divided by the scalar sum of all jet track momenta. The ratio of the hard-scatter vertex track p_{T} sum and the calibrated jet p_{T} is the second key observable which is typically 0 for pile-up jets as the pile-up jets are not related to the primary vertex. Both variables are then combined in a single variable stating the probability of a jet to originate from a hard-scatter interaction.

Forward jets require an adapted tagger, the forward jet vertex tagger (fJVT) [94, 95], as these jets exceed the coverage of the tracker. Momentum conservation of every pile-up vertex is used to identify forward pile-up jets instead of the JVT variables.

In the central region, two types of pile-up jets need to be differentiated. Stochastic pile-up jets should not be fully considered for the analysis of momentum conservation as they are built from particles coming from several pile-up vertices instead of a single vertex. In contrast, most of the tracks from QCD pile-up jets can be matched to exactly one pile-up vertex as these jets originate from a single pile-up interaction. Therefore, the sum of the track momenta associated to the vertex of the jet divided by the calibrated jet p_T must exceed 0.1 to suppress the stochastic central pile-up jets. All central hard-scatter jets of the pile-up vertex under study can be rejected by requiring JVT < 0.2. The missing transverse momentum of the vertex i, $\mathbf{p}_{\mathrm{T},i}^{\mathrm{miss}}$, is calculated by summing the jet $\mathbf{p}_\mathrm{T}$ of all central jets with $p_\mathrm{T} > 20$, the track momenta of jets with p_T below the prior threshold and the track momenta matched to this vertex of jets which failed the stochastic pile-up suppression cut. The fJVT discriminant is then defined as the maximum of the set of normalised projections of $\mathbf{p}_{\mathrm{T},i}^{\mathrm{miss}}$ onto the corresponding forward jet $\mathbf{p}_\mathrm{T}^{\mathrm{fj}}$ for all pile-up vertices i

$$\mathrm{fJVT} = \mathrm{max}_i \left(\frac{\mathbf{p}_{\mathrm{T},i}^{\mathrm{miss}} \cdot \mathbf{p}_\mathrm{T}^{\mathrm{fj}}}{|\mathbf{p}_\mathrm{T}^{\mathrm{fj}}|^2} \right). \tag{5.4}$$

The forward jet vertex tagger can separate forward pile-up jets from hard-scatter jets as the former are expected to be balanced by $\mathbf{p}_{\mathrm{T},i}^{\mathrm{miss}}$ leading to fJVT values close to 1 for pile-up jets in the forward direction and values closer to 0 for forward jets from the hard-scatter interaction.

5.2 Electrons

Electrons leave tracks in the inner detector and deposit their energy typically in a concise shower in the electromagnetic calorimeter. This shower is formed by electrons and photons which are produced via bremsstrahlung by electrons interacting with the detector material or the beam pipe. The photons can annihilate into electron-positron pairs which again can radiate photons thereby forming an electromagnetic shower. It can happen that more than a single track belongs to the corresponding energy deposit in the calorimeter as these collimated showers can already be formed inside the inner detector. This is considered in the electron reconstruction algorithm which can assign several tracks via a ΔR matching to the same electromagnetic energy cluster of a single prompt electron candidate within the coverage of the inner detector of $|\eta| < 2.47$.

Electromagnetic topo-clusters are formed from the same topo-clusters used in the jet reconstruction with the difference that they are not seeded by presampler cells or cells in the first layer of the electromagnetic calorimeter to suppress noise clusters. In general, only energy depositions in the cells of the electromagnetic calorimeter are considered to derive the electromagnetic energy of the cluster except for the transition region where energies from the presampler and from a scintillator in front of the calorimeter are also added. The fraction of the electromagnetic energy over the entire cluster energy needs to exceed 0.5 to reject about 60% of pile-up clusters [96]. Tracks are reconstructed from hits in the inner detector and are fitted in several iterations thereby taking energy losses due to bremsstrahlung into account [97]. The tracks are matched to the respective clusters and the primary track is mainly determined by the closest distance to the barycentre of the cluster in the second calorimeter layer where most of the energy of the shower is deposited.

A characteristic of the electron shower is that energies can be deposited in additional clusters formed by large angle radiations falling outside the cluster which need to be assigned to the main cluster of the electron. The main clusters are called the supercluster seeds and are identified from energy ordered electromagnetic topo-clusters if those pass a 1 GeV threshold and are assigned a track with a minimum of four hits in the SCT. Clusters within $\Delta\eta \times \Delta\phi = 0.075 \times 0.125$ (0.125×0.300) of the barycentre of the seed cluster (and if a track is the primary track for both clusters) are classified as satellite clusters. The supercluster energy is determined from the associated cells in the first three calorimeter layers and the presampler of the respective seed. Satellite clusters are restricted in size in η to suppress pile-up effects. Before the track matching is adapted to superclusters these clusters undergo a first energy calibration and only afterwards the final calibration is performed [98]. The charge of the electron is determined from the supercluster track curvature due to the magnetic field in the inner detector [96].

To distinguish prompt electrons from electrons originating from either photon conversion or a heavy flavour decay as well as from mis-identified hadronic jets [96] a likelihood-based identification approach is used. An extensive list of variables focused on the shower shape of the supercluster, the primary track and their compatibility form the input of this multivariate discrimination. Depending on the chosen working point, defined by their identification efficiency of 93% (80%) 'Loose' ('Tight'), additional fixed requirements need to be fulfilled besides the likelihood score to improve the rejection of converted photons. The working points are constructed in such a way that they are subsets of each other.

Prompt electrons in contrast to jets or electrons from heavy flavour decays are isolated and typically do not deposit energy in the hadronic calorimeter. $E_{\mathrm{T}}^{\mathrm{cone20}}$ is introduced to quantify the activity in the calorimeter around the electron within a cone of $\Delta R = 0.2$. The transverse energies of all positive topo-clusters are summed to form $E_{\mathrm{T,raw}}^{\mathrm{cone20}}$ from which the energy of the electron itself given by a 5×7 grid of cells in $\eta \times \phi$ is subtracted.

As this grid does not necessarily contain the entire energy of the electron a simulation-based leakage correction is applied before finally a pile-up correction is performed [90],

$$E_{\mathrm{T}}^{\mathrm{cone20}} = E_{\mathrm{T,raw}}^{\mathrm{cone20}} - E_{\mathrm{T,core}} - E_{\mathrm{T,leakage}}(E_{\mathrm{T}}, \eta, \Delta R) - E_{\mathrm{T,pile\text{-}up}}(\eta, \Delta R). \tag{5.5}$$

Isolated electrons need to fulfil the 'HighPtCaloOnly' working point which has a strong fake rejection rate above $E_{\mathrm{T}} > 100$ GeV by requiring $E_{\mathrm{T}}^{\mathrm{cone20}} < \max(0.015 \times p_{\mathrm{T}}, 3.5\ \mathrm{GeV})$. Pile-up contributions and electrons from either heavy flavour decays or photon conversion are suppressed by applying track-to-vertex association (TTVA) requirements. The transverse impact parameter significance must satisfy $|d_0|/\sigma(d_0) < 5$ to pass the TTVA selection, where d_0 is the closest distance between the electron track and the beamline in the transverse plane. To compensate for the varying resolution of d_0 the corresponding uncertainty $\sigma(d_0)$ is also considered which includes an uncertainty on the beam width as well as an uncertainty on the track obtained from the fit. The longitudinal impact parameter z_0 measures the distance between the electron track closest approach to the beamline and the primary vertex along the beam axis. The second TTVA requirement is $|z_0| \sin\theta < 0.5$ mm, where θ is the angle between the track and the beamline and $\sin\theta$ compensates a reduced accuracy with which z_0 can be measured for forward tracks. Both impact parameter criteria increase the probability that the electron stems from the primary vertex.

Efficiency scale factors are derived for reconstruction, identification, isolation, and trigger correcting for observed efficiency differences between data and MC simulations in $Z \to ee$ and $J/\Psi \to ee$ decays. They are applied as multiplicative event weights for each electron as they are determined in dependence on the electron transverse energy and pseudorapidity. The electron energy scale and resolution in the MC simulation are corrected by studying the same resonance decays as for the efficiency derivation to match the data [98].

5.3 Photons

Photons deposit their energy similar to electrons mainly in the electromagnetic calorimeter. In contrast to electrons, prompt unconverted photons leave no tracks in the inner detector as they are not charged. Prompt photons stem from production sources which are not related to hadron decays [99]. A relatively large fraction of the photons are converted to electron-positron pairs within the inner detector. This fraction ranges from around 20% in the central region of the detector to 65% at $|\eta| \approx 2.3$ [96]. Photons are reconstructed from the same superclusters used in the electron reconstruction with the difference that no tracks are assigned to the clusters [96]. Topo-clusters are added to conversion photons if they can be associated with the same conversion vertex as the supercluster. Clusters with opposite signed tracks compatible with a conversion vertex of a massless particle are considered converted photon candidates.

Photons are restricted to be contained within the coverage of the inner detector. An ambiguity resolution procedure is applied to identify a supercluster as either a photon or an electron as the respective superclusters are formed independently [96]. Identification requirements are placed on the shower shapes to reject non-prompt photons from hadron decays or from mis-identified hadronic jets. This separation can be further improved by applying isolation criteria to the energy contained within a cone around the photon including tracking and calorimeter information which is sensitive to hadronic activity in close vicinity of the photon. The final energy calibration is performed with data and MC simulations studying the final state photon radiation of leptonic Z boson decays [98].

5.4 Muons

Muons are mainly reconstructed from their tracks in the inner detector and the muon spectrometer as they only deposit little energy in the calorimeter [100].

The tracks in the inner detector are similarly reconstructed as in the jet reconstruction. To reconstruct the muon track, tracks in the spectrometer are partially constructed by combining the hits in the individual monitored drift tube chambers, the surrounding trigger chambers and the cathode strip chambers for $|\eta| > 2$. The spectrometer track is obtained from a fit of those track segments considering the bending of the muon track due to the magnetic field, possible misalignment between chambers, and potential interactions of the muons in the detector. Five muon definitions exist which differ in the composition of detector information used in the reconstruction of which three are explained in the following and more information is given in [100]. Combined muons are of particular interest in this analysis. They are identified by a combined track fit of the inner detector hits and the muon spectrometer hits allowing a potential energy loss in the calorimeters. The relevant hits are found by extracting the spectrometer tracks to the inner detector hits. The spectrometer hits can get exchanged during the fitting procedure. A looser muon selection includes calorimeter muons, which are reconstructed from tracks in the inner detector and energy deposits in the calorimeter, and segmented muons, whose inner detector tracks are expanded to the spectrometer where at least one track segment is required in close angular proximity.

Several working points are defined to quantify the quality of muon candidates. They differ in the efficiency to identify prompt muons and in the rejection rate of non-prompt muons. The rejection mainly focuses on the suppression of semileptonic decays of light hadrons. Those particles in general have a lower track quality as their trajectory through the detector changes because of the decay. In contrast, muons from heavy flavour decays have typically well reconstructed trajectories but can be rejected via isolation requirements as they tend to be surrounded by more activity in the inner detector and the calorimeters. The 'Medium' identification working point selects combined muons which have at least three hits in two out of the three spectrometer chambers with looser criteria for muons within $|\eta| < 0.1$. Those muons must have a compatible charge over momentum property for the inner detector and the spectrometer. 'Loose' muons include in addition segment-tagged and calorimeter-tagged muons within $|\eta| < 0.1$ where the muon spectrometer has no complete coverage.

Pile-up contributions as well as muons from cosmic and hadron decays are suppressed by applying TTVA selections. The transverse impact parameter significance, $|d_0|/\sigma(d_0)$, needs to be smaller than three and the longitudinal impact parameter must satisfy $|z_0| \sin\theta < 0.5\,\text{mm}$, where d_0, $\sigma(d_0)$, z_0 and θ are defined analogous to the electron parameters, to reject a majority of the non-prompt muons.

Tracking and calorimeter information is combined to define the 'FixedCutLoose' isolation which is required for isolated muons. The transverse track four momenta with $p_{\mathrm{T}} > 1$ GeV are summed within a variable cone $p_{\mathrm{T}}^{\mathrm{varcone30}} = \min(10\ \mathrm{GeV}/p_{\mathrm{T}}^{\mu}, 0.3)$ around the muon, excluding the muon track, and $p_{\mathrm{T}}^{\mathrm{varcone30}}/p_{\mathrm{T}}^{\mu}$ must be smaller than 0.15. The transverse energy deposits in the calorimeters are summed in a fixed cone of radius $R = 0.2$ around the extrapolated muon track subtracting the cluster of the muon and a pile-up correction using the jet area method [90] is performed. $E_{\mathrm{T}}^{\mathrm{cone20}}$ obtained in this way divided by the muon p_{T} needs to be below 0.3 to suppress non-isolated muons, in particular from heavy flavour decays.

Efficiency scale factors are derived for reconstruction, identification, track to vertex association and isolation correcting for observed efficiency differences between the data and the MC simulations in $Z \to \mu\mu$ and $J/\Psi \to \mu\mu$ decays. The momentum scale and resolution in the MC simulation are corrected with the same two resonance decays used to derive the efficiencies to match the data [101, 102]. In addition, $Z \to \mu\mu$ events are used to evaluate a bias in the muon momentum measurement which is dependent on the muon charge and related to misalignment of detector components [102].

5.5 Hadronically Decaying Taus

Taus have a very short lifetime which results in their decays occurring typically already before they reach the first detector layer. Taus can therefore only be reconstructed via their decay products. These are in 65% of the cases sets of hadrons which commonly contain either one (72%) or three (22%) charged pions and are referred to as either one- or three-prong taus. These taus can include any number of additional neutral pions. Their signature is hence similar to a concise jet with either one or three tracks with an absolute charge of 1. The rest of the taus decay mostly leptonically and are reconstructed as either electrons or muons. The energy and momentum of the neutrino of the hadronic tau decay cannot be measured by the detector and the observed part of the tau candidate is referred to as $\tau_{\text{had, vis}}$. Taus are reconstructed from anti-k_t jets with $\Delta R = 0.4$, $p_{\mathrm{T}} > 10\,\mathrm{GeV}$ and $|\eta| < 2.5$ build from topo-clusters [86] which are calibrated via the local hadronic calibration procedure [103]. A boosted decision tree identifies the prong tracks within $\Delta R = 0.4$ of the reconstructed tau trajectory via track p_{T}, impact parameters, and number of hits in the tracking detectors. The hadronic tau energy calibration features a pile-up correction followed by a response correction of the already calibrated topo-clusters [16, 104].

Tau candidates are removed if they are in close vicinity ($\Delta R < 0.4$) of a reconstructed electron as energy depositions of electrons can be falsely reconstructed as one-prong taus. Taus can be distinguished from quark- or gluon-initiated jets by a recurrent neural network trained with tracking and calorimeter information which classifies taus into four overlapping working points depending on the background rejection efficiency. Two separate networks are designed for the one and three-prong hadronic taus as they feature distinct decay patterns. The 'Loose' identification working point with a signal efficiency of 85% (75%) for one- (three-)prong taus [105] is sufficient for this analysis as taus are only used to veto events containing hadronically decaying taus.

5.6 Missing Transverse Momentum

Neutrinos are very weakly interacting particles and typically leave no signatures in the detector in terms of energy deposits which makes an explicit reconstruction impossible. Instead, one can make use of the fact that the two neutrinos coming from a Z boson decay lead to a momentum imbalance in the transverse plane as the colliding protons have negligible momenta in this direction. An observable that quantifies the momentum carried away by the to the detector invisible particles is the missing transverse momentum, $E_{\mathrm{T}}^{\mathrm{miss}}$[2]. Conservation of the momentum in the transverse plane justifies defining $E_{\mathrm{T}}^{\mathrm{miss}}$ as the negative vectorial sum of the transverse momenta of all visible final state particles.

The missing transverse momentum vector is hence defined as the negative vectorial p_{T} sum of reconstructed and calibrated electrons (e), photons (γ), hadronically decaying taus (τ), muons (μ) and jets as well as a soft track component which is given by tracks stemming from the hard-scatter vertex not associated to any particle. Along the x and y coordinates spanning the transverse plane, the $E_{\mathrm{T}}^{\mathrm{miss}}$ vector components can be calculated as

$$E_{x(y)}^{\mathrm{miss}} = E_{x(y)}^{\mathrm{miss},e} + E_{x(y)}^{\mathrm{miss},\gamma} + E_{x(y)}^{\mathrm{miss},\tau} + E_{x(y)}^{\mathrm{miss},\mu} + E_{x(y)}^{\mathrm{miss,\ jets}} + E_{x(y)}^{\mathrm{miss,\ soft}}, \tag{5.6}$$

where every component is derived from the negative vectorial sum of all transverse momenta of the constituent type in the event [106]. Potential ambiguities need to be resolved by an overlap removal as energy deposits can be reconstructed as several different particle candidates [107]. The order of their occurrence in Equation 5.6 determines the priority with which the particles are considered where the subsequent candidates are removed. The magnitude of the missing transverse momentum vector is defined as $E_{\mathrm{T}}^{\mathrm{miss}} = \sqrt{\left(E_x^{\mathrm{miss}}\right)^2 + \left(E_y^{\mathrm{miss}}\right)^2}$ which per definition is always positive.

A precise knowledge of the particles, pile-up and detector acceptance is required as the missing transverse momentum is sensitive to any miscalibrations and noise resulting in a non-linear response.

---

[2] Outside the ATLAS collaboration $E_{\mathrm{T}}^{\mathrm{miss}}$ is often referred to as $p_{\mathrm{T}}^{\mathrm{miss}}$.

6 Analysis Dataset, Event Selection and Signal Region Definitions

The R^{miss} measurements are based on the selection of proton-proton collision events containing Z boson decays into either pairs of neutrinos or charged leptons. The reconstructed objects as defined in Chapter 5 in an event are hence required to fulfil certain criteria. These are defined in this chapter. The events get classified into so-called signal regions which are in contrast to control and validation regions used to study background processes. These selections are in the following referred to as detector level selections. Three signal regions are defined in this chapter which are constructed to select $Z \rightarrow \nu\nu+\text{jets}$, $Z \rightarrow ee+\text{jets}$ and $Z \rightarrow \mu\mu+\text{jets}$ processes[1]. This chapter starts with a description of the collision events used in this measurement which are referred to as the dataset (Section 6.1), discusses the specific requirements placed on the reconstructed objects to select the signal processes and to enhance their overall contributions compared to backgrounds (Section 6.2), and finally defines the common observable in the three signal regions as well as the regions themselves (Section 6.3).

6.1 The Dataset of the Analysis

The dataset used in this analysis was collected in 2015-2016 with the ATLAS detector from proton-proton collisions at a centre-of-mass energy of $s = \sqrt{13}\,\text{TeV}$. The use of this partial Run-2 data set is motivated by the access to lower $E_{\text{T}}^{\text{miss}}$ trigger thresholds and lower pile-up [19, 108]. The time between two bunch crossings was 25 ns. Solely data are considered which were taken during stable LHC beam conditions and fulfil data quality requirements [19] excluding periods where the detector or its sub-components were malfunctioning. This dataset has an integrated luminosity of $36.65 \pm 0.32\,\text{fb}^{-1}$ [109] which was among others determined with the LUCID-2 detector [110]. The average number of simultaneous collisions in a single bunch crossing, referred to as pile-up, was 13.4 for $3.24\,\text{fb}^{-1}$in 2015 and increased to 25.1 in 2016 [19] where $33.40\,\text{fb}^{-1}$were recorded.

---

[1] The following notation is motivated by the fact that in the SM the invisible Z decays are decays into pairs of neutrinos: $Z \rightarrow \nu\nu+\text{jets}$ for $Z(\rightarrow \text{invisible})$+jets, and analogously $Z \rightarrow \ell\ell+\text{jets}$ is used to denote $Z/\gamma^{*}(\rightarrow \ell^{+}\ell^{-})$+jets throughout this thesis.

The vertex with the largest sum of squares of associated track momenta is considered the hard-scatter primary vertex. Events are required to have at least one primary vertex. This vertex must have at least two tracks with $p_{\mathrm{T}} > 500\,\mathrm{MeV}$ which can be traced back to the beam spot where the proton-proton collisions take place to reduce the contribution of secondary vertices [89].

6.2 Object and Event Selection

This section discusses both the criteria on objects in collision events and on the collision events themselves that need to be fulfilled such that an event is assigned to a corresponding signal process.

Triggers used to select the Events

The event topology of $Z \to \nu\nu + \mathrm{jets}$ can be selected by either a jet or a missing transverse momentum trigger. The $E_{\mathrm{T}}^{\mathrm{miss}}$ triggers [108], which solely use calorimeter information, are used to select the collision events. The missing transverse momentum in the trigger is calculated from the negative transverse momentum vector sum of hadronic jets with a $p_{\mathrm{T}} > 7\,\mathrm{GeV}$. Those jets are calibrated and corrected for pile-up contributions with the jet-area method. Nevertheless, increasing pile-up between the different run periods makes a raise in the trigger $E_{\mathrm{T}}^{\mathrm{miss}}$ thresholds necessary which are set to 70 GeV in 2015 and to 90 and later increased to 110 GeV in 2016. These triggers become fully efficient above 170 GeV.

The second possibility to select these events are jet triggers. The large cross section of inclusive di-jet production at the LHC sets stringent requirements on potential jet triggers. The main lowest unprescaled jet trigger for the 2016 run period, the HLT_j380, places a threshold of 380 GeV on the p_{T} for the jet candidate found by the trigger system and becomes fully efficient above 436 GeV [111] for reconstructed jets with larger p_{T} due to resolution effects. This would strongly boost the Z boson and its corresponding decay products as the jet and the Z boson momenta are correlated which reduces the statistics.

Events including muons are triggered with the same $E_{\mathrm{T}}^{\mathrm{miss}}$ triggers as these triggers do not take any information from the tracker and the muon system into account. The HLT $E_{\mathrm{T}}^{\mathrm{miss}}$ hence contains no muons as they deposit almost no energy in the calorimeters. The simultaneous production of a muon pair and jets then leads to a momentum imbalance in the transverse plane in the calorimeter system which is considered by the $E_{\mathrm{T}}^{\mathrm{miss}}$ triggers.

Single-electron triggers [112] are used to select events containing at least one electron.

The lowest-p_{T}, unprescaled electron triggers require a p_{T} threshold of 24 or 26 GeV, either a 'Medium' or 'Tight' likelihood identification and for 2016 a 'Loose' tracking-only isolation. The corresponding upstream Level-1 triggers include hadronic vetos and an isolation requirement for objects with $E_{\mathrm{T}} < 50\,\mathrm{GeV}$ in 2016. Less stringent criteria are placed by high-p_{T} electron triggers which remove the isolation requirement and change to a 'Loose' identification for $p_{\mathrm{T}} > 120$ (140) for 2015 (2016). An intermediate trigger selects 'Medium' electrons with $p_{\mathrm{T}} > 60\,\mathrm{GeV}$. The 2016 electron triggers do not consider the transverse impact parameters in their decisions. The restrictions on the electrons are placed to keep the rates at a manageable level as only a total bandwidth of 1 kHz is available at which the events can be saved (Section 3.2.4). In 2016 a decrease in the efficiency at very high transverse momentum is partially restored with an additional trigger which requires $E_{\mathrm{T}} > 300\,\mathrm{GeV}$ for the topo-clusters but places no selection criteria on tracks [112]. The introduced single-electron triggers are run as logical or and events are selected as soon as they pass any of those triggers. Trigger efficiencies are derived via the tag-and-probe method selecting $Z \to ee$ decays and respective scale factors are obtained by comparing data and MC simulations [112]. The corresponding uncertainties on those scale factors are propagated onto the final result.

Jet Selection

The missing transverse momentum from $Z \to \nu\nu + \mathrm{jets}$ processes needs to be balanced by an energetic jet. The transverse momentum of the jet must be larger than 110 GeV. This leaves some margin for resolution effects and for additional radiation compared to the $E_{\mathrm{T}}^{\mathrm{miss}} > 130\,\mathrm{GeV}$ requirement which ensures a sufficient trigger efficiency for the $Z \to \nu\nu + \mathrm{jets}$ events. This leading jet must be central, $|\eta| < 2.4$, to be within the coverage of the tracking detector which allows the rejection of non-collision backgrounds.

Additional jets are defined as objects with a $p_{\mathrm{T}} > 30\,\mathrm{GeV}$ and an absolute rapidity smaller than 4.4 to be within the coverage of the forward detectors.

Three dominant background sources can mimic jets [113, 114]. Those are the beam-induced background, which occurs due to beam gas scattering or secondary cascades of protons interacting with the collimators far away from the interaction point, cosmic rays overlapping with collision events, and calorimeter noise. The first two are also often referred to as non-collision backgrounds where a high-p_{T} muon fakes a jet signature. The calorimeter noise originating from coherent noise or electronic noise bursts is often already rejected by the data quality requirements [19] and the residual background can be further suppressed by inspecting the characteristic LAr signal pulse shapes.

Energy and p_{T} ratio quantities are used to further reject all three background sources as these mainly spread longitudinally in the calorimeter and leave no tracks in the inner detector. This is included amongst other selections in a set of loose quality criteria [113] which every selected jet needs to pass. If any jet fails these requirements the entire event is rejected. A significant amount of the non-collision background remains present after this selection. The ratio of the charge fraction, f_{ch}[2], and the maximum sampling fraction, f_{max}, which is defined as the maximal fractional energy deposited in a single calorimeter layer, is found to be a powerful discriminant between hard-scatter jets and fake jets and is required to exceed 0.1 for the leading jet. The charge fraction is only available within the coverage of the tracker which restricts the leading jet to be within $|\eta| < 2.4$. A residual non-collision background remains although the efficiency of the fake jet reduction is very high. The derivation of the corresponding background estimate is presented in Section 7.1.

Pile-up jets are suppressed by applying the most stringent standard (forward) jet-vertex-tagger requirements available within ATLAS which act on all jets with a p_{T} in the range from 30-60 GeV. In well balanced dijet events the false removal of a hard-scatter jet failing the (f)JVT criteria creates artificial $E_{\mathrm{T}}^{\mathrm{miss}}$ resulting in events passing the $Z \to \nu\nu +$jets selection. This event category is reduced by rejecting all events where at least one jet is tagged as a pile-up jet. These are mainly events with rather low $E_{\mathrm{T}}^{\mathrm{miss}}$ as there the relative contribution of a removed jet becomes a relevant constituent of $E_{\mathrm{T}}^{\mathrm{miss}}$ to exceed the 130 GeV threshold. This is discussed in more depth in Section 7.2.

Signal and Baseline Lepton Definitions

Two categories of leptons are defined in this analysis which are the baseline and the signal leptons. The baseline leptons are inclusive in all three charged lepton families and thereby contain hadronically decaying taus. They need to pass only permissive selection criteria since they are used to reject (veto) events which contain at least one additional baseline lepton and for the estimation of the fake lepton background (Section 7.4). Signal leptons are restricted to electrons and muons and need to fulfil further requirements compared to the baseline leptons to suppress background sources. They are selected in the $Z \to \ell\ell +$jets lepton signal and $W \to \ell\nu +$jets control regions (Section 7.3). Leptonically decaying taus can be reconstructed as either electrons or muons. The

---

[2] The charge fraction is defined as the scalar sum of the transverse track momenta which are associated with the primary vertex of the jet divided by the transverse momentum of the jet: $f_{\mathrm{ch}} = \sum p_{\mathrm{T}}^{\mathrm{track}}/p_{\mathrm{T}}^{\mathrm{jet}}$.

background contribution from taus in the $Z \rightarrow \nu\nu+$jets signal region is estimated by a data-driven method using electrons and muons presented in Section 7.3.

Baseline electron candidates are required to have a p_{T} larger than 7 GeV to ensure a sufficient reconstruction efficiency. In addition, they must be within $|\eta| < 2.47$ to guarantee track reconstruction while the transition region $1.37 < |\eta| < 1.52$ is excluded due to its poor reconstruction efficiency resulting from the high material budget (Section 5.2) and must pass the 'Loose' identification selection. Signal electron candidates in addition need to fulfil the 'Tight' identification, isolation and track to vertex association criteria defined in Section 5.2 to reject background electrons. The leading signal electron transverse momentum is required to be larger than 50 GeV. This high p_{T} lepton requirement allows the rejection of background processes. This is possible as the leading electrons are boosted by the p_{T} of the Z boson and thereby typically have transverse momenta above the lowest single electron trigger thresholds which are around 30 GeV. The sub-leading signal electron p_{T} needs to be larger than 25 GeV to suppress contributions from lepton fake backgrounds (Section 7.4) which are accompanied by relatively large uncertainties.

Baseline muon candidates are selected if they fulfil the 'Loose' identification requirements, have a p_{T} exceeding 7 GeV to ensure a high reconstruction efficiency and are reconstructed within $|\eta| < 2.5$ for track reconstruction. Signal muon candidates must pass the 'Medium' identification, isolation, as well as track to vertex association selections, described in Section 5.4 in addition to the baseline selection to reject background muons. The (sub-)leading muon needs to fulfil $p_{\mathrm{T}} >$(25) 50 GeV to reject fake backgrounds.

Hadronically decaying tau candidates are selected if they have a p_{T} larger than 20 GeV and either one or three tracks with an absolute charge of 1, are within $|\eta| < 2.47$ and pass the 'Loose' identification requirement (Section 5.5).

The detector level baseline and signal lepton definitions are summarised in Table 6.1

Overlap Removal

Jet, electron, muon, and tau candidates are all reconstructed independently by their respective algorithms and the same detector signatures can therefore be reconstructed as several different particle types. This ambiguity needs to be resolved with an overlap removal procedure which uniquely identifies every particle following the recommendations in [115].

Baseline Selection	**Electron**	**Muon**	**Tau**
p_{T}	> 7 GeV	> 7 GeV	> 20 GeV
$\lvert\eta\rvert$	$0 < \lvert\eta\rvert < 1.37$ or $1.52 < \lvert\eta\rvert < 2.47$	$\lvert\eta\rvert < 2.5$	$\lvert\eta\rvert < 2.47$
Identification	'Loose'	'Loose'	'Loose'
Signal Selection	**Electron**	**Muon**	
p_{T}	> 25 GeV	> 25 GeV	
$\lvert\eta\rvert$	$0 < \lvert\eta\rvert < 1.37$ or $1.52 < \lvert\eta\rvert < 2.47$	$\lvert\eta\rvert < 2.5$	
Identification	'Tight'	'Medium'	
Isolation	'FCHighPtCaloOnly'	'FCLoose'	
TTVA	$\lvert z_0 \times \sin\theta\rvert < 0.5$mm & $\lvert d_0\rvert/\sigma(d_0) < 5$	$\lvert z_0 \times \sin\theta\rvert < 0.5$mm & $\lvert d_0\rvert/\sigma(d_0) < 3$	

Table 6.1: Detector level baseline and signal lepton selections.

Tau candidates are removed if they are within $\Delta R < 0.2$ of either an electron or a muon candidate. This is necessary as muons can fake taus with one track if they deposit energy in the calorimeter which typically coincides with some mis-alignment between the tracks measured in the muon spectrometer and the inner detector. The tau identification already applies an intrinsic overlap removal if they are close to an electron (Section 5.5). Any remaining tau candidate is rejected if an electron is in close proximity.

Electrons and muons can be reconstructed from the same object if the muon radiates a hard photon which is reconstructed in the calorimeter. They can be efficiently separated from real close-by leptons if they share the same track in the inner detector. In the case of a calorimeter muon candidate the electron candidate is rejected and vice versa in the case of a combined or segmented muon. Often this object is also reconstructed as a jet candidate which is removed in a subsequent step.

The electron-jet overlap removal resolves the ambiguity of prompt electrons and jets which can stem from a semi-leptonically decaying heavy-flavour jet or a light-flavour jet faking an electron as both objects are clustered from energy deposits in the calorimeter cells. The reconstructed jet candidate is removed if it is within $\Delta R < 0.2$ of the electron candidate and otherwise, the electron candidate is removed if within $\Delta R < 0.4$.

Muons are charged and therefore can radiate photons which might seed jet candidates. This can lead to a signature with a track in the inner detector from the muon and an energy deposit in the calorimeter from the photon and can therefore be reconstructed as an electron or a jet candidate. These jets have a small number of tracks and can be well separated from hadronic jets. Jet candidates with less than three tracks which are within $\Delta R < 0.2$ of a muon candidate are rejected to suppress these fake jets from radiation. Muons from light meson and heavy-flavour decays are non-isolated, have small momenta and have their origin in a secondary vertex. These non-prompt muons are rejected against jets if they are within $\Delta R < 0.4$ of a reconstructed jet.

In a last step jet candidates within $\Delta R < 0.2$ of a tau candidate are removed as they are used in the reconstruction of the tau.

The particle candidates passing the overlap removal procedure are the baseline and signal leptons or jets. This approach introduces an inefficiency in the case where a prompt lepton is close to a real hadronic jet which is considered in the detector correction.

A similar overlap removal procedure is employed during the $E_{\mathrm{T}}^{\mathrm{miss}}$ calculation [106].

Proxy of the Z Boson Transverse Momentum

In the $Z \rightarrow \nu\nu+$jets region $E_{\mathrm{T}}^{\mathrm{miss}}$ can be a valid proxy for the Z boson p_{T}. In this analysis $p_{\mathrm{T},Z}$ is introduced as a proxy for the p_{T} of all vector bosons independent of their decay channels. It is defined as the vector sum of $E_{\mathrm{T}}^{\mathrm{miss}}$ and the p_{T} of the prompt electrons or muons associated with the vector boson. This defines an inclusive observable for all three signal regions, where for the neutrino channel only the $E_{\mathrm{T}}^{\mathrm{miss}}$ component is considered and in the case of Z boson decays into two charged leptons it can be derived as

$$p_{\mathrm{T},Z} = \sqrt{\left(E_{\mathrm{x}}^{\mathrm{miss}} + p_{\mathrm{x},\ell_1} + p_{\mathrm{x},\ell_2}\right)^2 + \left(E_{\mathrm{y}}^{\mathrm{miss}} + p_{\mathrm{y},\ell_1} + p_{\mathrm{y},\ell_2}\right)^2}\ . \tag{6.1}$$

This consistent definition for leveraging correlations between the systematic uncertainties related to the measurement of the jet system in the numerator and the denominator of the R^{miss} ratios which is shown in Chapter 10.

6.3 Signal Region Definitions

All three orthogonal signal regions are required to have a $p_{\mathrm{T},Z}$ larger than 130 GeV which is balanced by at least one jet with a $p_{\mathrm{T}} > 110$ GeV within $|\eta| < 2.4$ which needs to pass the above described selection criteria and the overlap removal. The QCD multijet background (Section 7.2) is suppressed by enforcing an angular separation between all selected jets and the $p_{\mathrm{T},Z}$ of $\Delta\phi\,(\mathrm{jet}, p_{\mathrm{T},Z}) > 0.4$. The event is rejected if any jet fails this requirement. Even if this background is only significant in the $Z \rightarrow \nu\nu+$jets signal region, the angular separation is also applied in the two-lepton signal regions to achieve consistent phase space for the construction of the ratio. Any additional baseline lepton, including taus, besides the expected number of signal leptons leads to a rejection of the event. The $Z \rightarrow \nu\nu+$jets signal region, the numerator of the ratio, is defined by the above selections. They also need to be fulfilled for the electron and muon $Z \to \ell\ell+$jets signal regions.

The $Z \to ee+$jets signal region requires exactly two oppositely charged signal electrons in addition to the above requirements. The invariant mass of the two signal electrons needs to be within a 50 GeV mass window around the mass of the Z boson, $66 < m_{ee} < 116$ GeV, to suppress combinatorial backgrounds and contributions from virtual photons which are divergent for small invariant masses.

The $Z \to \mu\mu+$jets signal region requires two additional oppositely charged signal muons alongside the common selection criteria. The invariant mass of the di-muon system needs to be within $66 < m_{\mu\mu} < 116$ GeV to suppress various background sources.

The main detector level event selection criteria defining the $Z \to \nu\nu+$jets and the two $Z \to \ell\ell+$jets signal regions are summarised in Table 6.2.

Common Event Selection	
$p_{\mathrm{T},Z}$	> 130 GeV
Leading jet p_T	> 110 GeV
Leading jet $\lvert\eta\rvert$	< 2.4
Additional jet $\lvert y\rvert$	< 4.4
Additional jet p_T	> 30 GeV
$\Delta\phi$(jet, $E_\mathrm{T}^\mathrm{miss}$)	> 0.4, for every jet
Additional baseline lepton (e, μ, τ)	None
Additional $Z \to \ell\ell+$jets Selection	
Number of signal leptons	2 same flavour opposite charge (e^-e^+ or $\mu^-\mu^+$)
Leading lepton p_T	> 50 GeV
Sub-leading lepton p_T	> 25 GeV
$m_{\ell\ell}$	66-116 GeV

Table 6.2: Main detector level event selections for the $Z \to \nu\nu+$jets and $Z \to \ell\ell+$jets signal regions.

7 Backgrounds

The $Z \to \nu\nu+$jets and the two $Z \to \ell\ell+$jets signal regions, which are used to construct the numerator and the denominators of the R^{miss} ratios, contain background events which are not related to the Z boson plus jets signal processes these regions are designed to select. A precise knowledge of their contributions and their corresponding uncertainties is crucial. Only then an exact subtraction of the background events from the measured data is possible to obtain the correct number of signal events stemming from Z boson decays into either pairs of neutrinos, electrons or muons. In particular, in the $Z \to \nu\nu+$jets signal region about half of the selected events are classified as background processes despite the dedicated event selection. The relative contributions of signal and background processes to the signal regions are sketched in Figure 7.1.

The relative contributions to the $Z \to ee+$jets and $Z \to \mu\mu+$jets signal regions are identical at the percent level and therefore visualised together as $Z \to \ell\ell+$jets represented by the inner ring in the sketch. They are both very pure in the sense that 94% of the events are expected to stem from leptonic Z boson decays into either two electrons or two muons. Minor contributions arise from di-/triboson and electroweak V+jets production as well as semileptonic $t\bar{t}$ decays. These can be directly taken from MC simulations as their corresponding normalisation uncertainties, which are typically relatively large, only have a minor impact on the final result. Background events related to fake leptons are not well described within the MC simulation and therefore their contribution is derived via a data-driven technique.

The signal contribution to the $Z \to \nu\nu+$jets signal region in contrast is only 47% which can be seen in the outer ring of the sketch. About 38% of the events in the $Z \to \nu\nu+$jets signal region are attributed to $W \to \ell\nu+$jets processes, where the lepton is not properly reconstructed and identified. The sizeable renormalisation and factorisation uncertainties related to these SM predictions require a data-driven approach to get a handle on these uncertainties related to the normalisation of the corresponding cross sections. Dedicated control regions are defined to normalise the $W \to \ell\nu+$jets background processes in the $Z \to \nu\nu+$jets signal region. Contributions from processes including single-top or $t\bar{t}$ decays, di-/triboson or electroweak V+jets production, and Z boson decays into charged lepton pairs which are not correctly identified or found

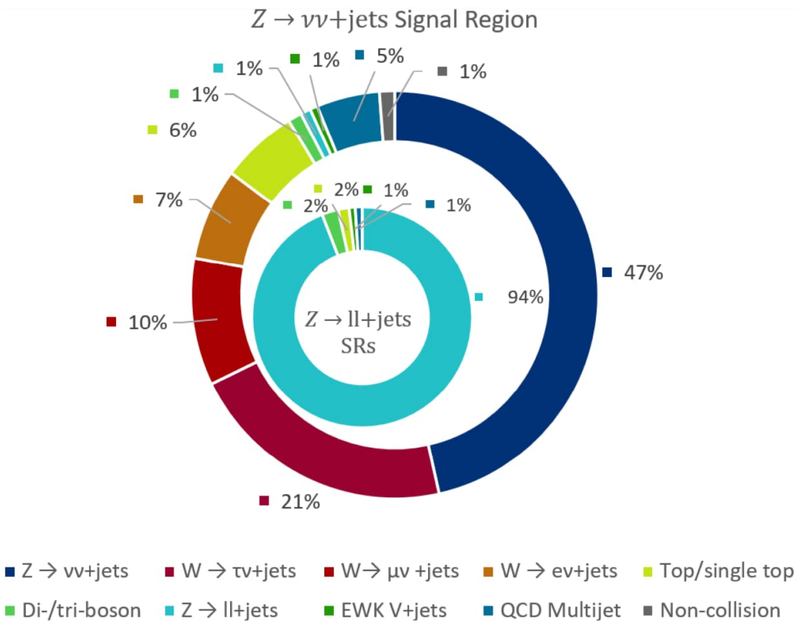

Figure 7.1: Sketch of the relative process contributions to the $Z \to \nu\nu+$jets (outer ring) and $Z \to ee+$jets/$Z \to \mu\mu+$jets (inner ring) signal regions. The composition of the two lepton signal regions is identical within the shown precision and therefore represented by $Z \to \ell\ell+$jets.

within the selected phase space are directly taken from the MC simulations. This is possible as the contributions of those processes are mainly at the percent level except for the leptonic $t\bar{t}$ decays, which contribute about 5%. The respective uncertainties partially cancel in the construction of the R^{miss} ratios as these processes appear in both the numerator and the denominators and therefore are no dominant source of uncertainty on the final result. Background processes either due to mis-measurements of transverse jet momenta in QCD multijet events or due to sources not related to the collisions need to be derived via data-driven methods and contribute about 5% and 1%, respectively.

The background processes which are not taken directly from MC simulations are discussed within this chapter. These include for the $Z \to \nu\nu+$jets signal region the non-collision (Section 7.1) and the QCD multijet (Section 7.2) backgrounds as well as data-driven estimates for $W \to \ell\nu+$jets events (Section 7.3). Finally, fake lepton backgrounds, which are relevant for the estimation of the $W \to \ell\nu+$jets contributions to the $Z \to \nu\nu+$jets signal region and for both $Z \to \ell\ell+$jets signal regions (Section 7.4), are presented.

7.1 Non-Collision Backgrounds

Backgrounds from sources that are not directly related to the collisions in the detector play a crucial role in the $Z \to \nu\nu + \text{jets}$ region. These are able to mimic events with jets and $E_{\mathrm{T}}^{\mathrm{miss}}$, which necessitates an understanding of the corresponding sources, to apply efficient suppression criteria, and to estimate the remaining background contribution.

Beam-induced background events are one of the three main sources of these backgrounds and will be discussed in the following section. The other two sources are cosmic muons and calorimeter noise clusters. The latter are already well suppressed by the applied data quality checks and are further reduced during the jet cleaning by the application of pulse shape requirements [114] and are therefore not further considered. Cosmic muon and beam-induced background events both include energetic muons as these are the only visible particles which are reliably able to evade the heavy shielding of the detector.

Muons from cosmic showers deposit energy in the calorimeters via radiative processes such as bremsstrahlung and leave no tracks in the inner detector if they traverse the detector sufficiently far away from the interaction point. These cosmic muons appear independently of the timing of the collisions and in a constant pattern in contrast to the beam-induced backgrounds which have a clear ϕ dependence. Muons from cosmic showers have to pass through about 60 m of rock, where they deposit around 40 GeV of energy [116]. The amount of material is in general sufficient to stop almost every other particle type from the shower which leave signatures in the detector. The energy deposition of the muons in the detector needs to be sizeable to exceed the $E_{\mathrm{T}}^{\mathrm{miss}}$ trigger thresholds. The cosmic muon background is expected to be an order of magnitude smaller than the beam-induced backgrounds at the lower end of the $p_{\mathrm{T},Z}$ spectrum and rises to approximately equal size in the high-p_{T} tail where the non-collision backgrounds overall become negligible [116]. The cosmic muon background is to a certain extent reduced by the selection criteria used for the suppression of the beam-induced background. Remaining events are partially considered in the beam-induced background estimate as they can have similar signatures, but are otherwise not treated individually. The discussion of the beam-induced background is based on [116–118].

Beam-induced Backgrounds

The beam-induced backgrounds originate from three main sources which are indicated in Figure 7.2. These include muons from showers produced by tertiary beam halos, which contain protons evading the primary and secondary collimators of the momentum and

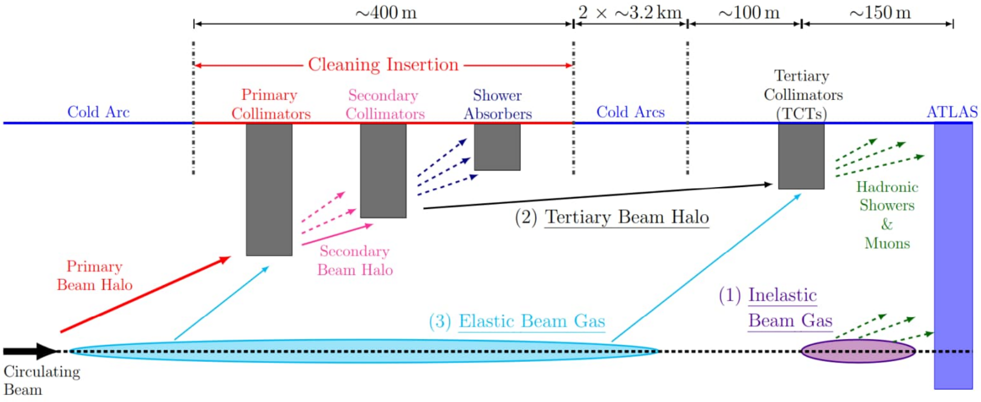

Figure 7.2: Sketch of the LHC collimator system and the sources of beam-induced backgrounds which are inelastic (purple) and elastic (azure) beam-gas scattering of the protons and interactions of the tertiary beam halo with the tertiary collimators (black) [117].

betatron cleaning, interacting with the tertiary collimators (TCTs) protecting the beam-focusing quadrupole magnets at 145-148 m from the interaction point [117]. Another source are elastic beam-gas collisions which are partially stopped at the TCTs before they can be removed by the cleaning systems. The last source is inelastic scattering of protons with the beam-gas leading to showers of secondary particles. These particles are often stopped by the shielding material in front of the detector. Muons, especially with large energies, are still able to reach the detector even from the accelerator arcs if they are emitted tangentially or are bent by the dipole magnets to be reconstructed within the calorimeters. High-p_T muons produced by beam-induced effects deposit large fractions of their energies via electromagnetic and in rare occasions via hadronic showers which often have a longitudinal profile along the beam axis and are contained within a single layer of a calorimeter.

Beam halos are generated by many different processes. These include, among others, elastic scatterings of protons with beam-gas, noise in the accelerating cavities, scattering between the two beams as they share the same beam pipe up to the neutral absorbers in front of the TCTs blocking neutrons and photons emitted at small angles, resonances, and instabilities [117]. The two beams are cleaned in two sectors which are both two arcs away from the detector. The primary collimators in these two sectors either remove protons which have an off-momentum or drifted out of the betatronic beam trajectory [117]. A secondary halo is formed by particles which scatter at the primary collimators. These are stopped by a secondary collimator which is followed by a tungsten absorber. The rate of the protons lost in the cleaning procedure is of the same order of magnitude as the loss due to the interaction rate [118]. A remaining tertiary halo is often able to hit the tertiary collimators close to the experiments even if the cleaning system is very efficient, as the number of protons in the primary halo which need to be removed is very high. Protons stopped close to the experiment can induce particle showers in which highly energetic muons are created on the straight sector of the accelerator complex. These muons are able to penetrate the heavy shielding which protects the detector and become a considerable background source. They mostly enter the detector at radii below 2 m [118] and are partially within the coverage of the electromagnetic calorimeter barrel which reaches from 1.5-2 m. The rate of protons hitting the TCTs after the betatron cleaning procedure is different for the two beams as they must pass through either two or six octants.

Muon production by interactions of the tertiary halo with the TCTs cannot easily be differentiated from elastic beam-gas scattering muon production as this process significantly contributes to the evolution of the tertiary halo. The elastic scattered protons are often stopped at the TCTs before they reach the cleaning stations and can contribute at the same order of magnitude as the tertiary halo to the generation of energetic muons [118].

The beam-induced backgrounds were studied in detail in isolated, unpaired bunches which lead to no intrinsic proton-proton collisions [116–118]. These studies show that a large fraction of the beam-induced backgrounds come from inelastic scatterings of protons with beam-gases leading to muons which arrive at lower radii if produced within the inner triplet quadrupole magnets focusing the beams. The rate of inelastic scattering scales linearly with the pressure in the vacuum chamber and the beam intensity [118]. Muons produced via inelastic interactions between protons and beam-gas can reach the detector even from distances as large as 500 m. These muons can fake jet signatures if they are produced far away from the interaction point and thereby are bent to sufficiently large radii to reach the calorimeters.

Suppression of Beam-induced Backgrounds

Muons leading to beam-induced background events are often deflected by magnetic fields introduced by the beam separation and recombination dipole magnets which are situated at 59-83 m and 153-162 m from the interaction point. This leads to pronounced peaks at $|\phi| = 0, \pi$ in their azimuthal distribution. As these muons are expected to mimic jet signatures, these peaks are also expected to be visible for jets. The ϕ distribution of the leading jet with a $p_{\mathrm{T}} > 110\,\mathrm{GeV}$ within the coverage of the tracking detector is shown

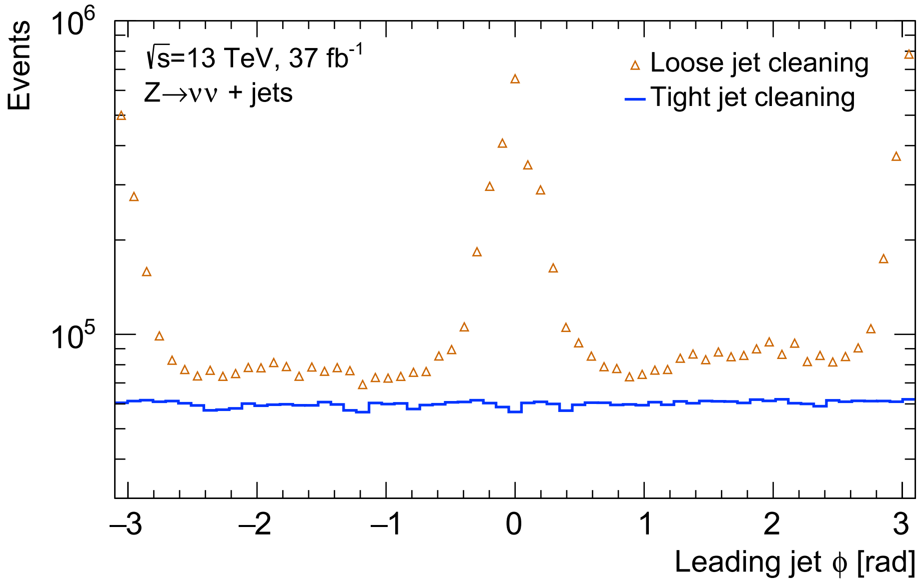

Figure 7.3: Leading jet ϕ distribution in data with the loose jet cleaning (orange) and with an additional tight cleaning criteria applied to the leading jet (blue) in the $Z \to \nu\nu+$jets signal region. The tight cut removes the two peaks which are related to beam-induced background events where the muons are bent by the beam splitting and recombining dipole magnets.

in Figure 7.3 with only loose jet cleaning criteria [113] applied. The two-peak structure is indeed present, and the magnitude of the peaks already provides an indication of the required size of the reduction to suppress the beam-induced background to the percent level to make it subdominant. A slight asymmetry is visible between positive and negative ϕ values in the region enclosed by the two maxima, which is related to different amounts of free space between the tunnel floor and ceiling from the beam pipe. This translates into different volumes in which pions and kaons from hadronic showers can decay into muons. The beam pipe is only 1 m above the ground whereas the distance to the ceiling is about 2 m [118].

A distinct pattern of the beam-induced background events is that they deposit most of their energy in a single layer in the electromagnetic calorimeter and typically have no tracks associated with the energy clusters in the calorimeter. This is in contrast to features of hard-scatter jets even if the background events have some track activity due to minimum bias events occurring at the same time. A selection criterion on the charge fraction and maximum sampling fraction defined in Section 6 which incorporates the two characteristics was found to be efficient in rejecting those backgrounds [116]. The requirement of $f_{\mathrm{ch}}/f_{\mathrm{max}} < 0.1$ for the leading jet provides a reasonable balance between a strong background rejection and a high signal efficiency. Adding this requirement to the loose jet selection for the leading jet defines the tight jet cleaning. The ϕ distribution of the leading jet after the application of this tight selection is shown in Figure 7.3. It can be seen that the two peaks are removed, and the distribution is evenly distributed as expected since there should be no intrinsic preferred direction in ϕ for the leading jet. The reduction in the peaks is more than an order of magnitude whereas the regions which are less populated by the beam-induced background are about 25% reduced.

The jet timing, which is defined as the weighted average cell timing of the calorimeter cell square energy with a nanosecond time resolution, is not used as a discriminant to suppress beam-induced backgrounds but is instead used to define a background-enriched control region. The cell timing is calibrated such that energy deposits of particles originating from proton-proton collisions in the interaction point occur at time zero. Beam-induced backgrounds are expected to arrive early as will be explained in the following section.

Beam-induced Background Estimate

The timing of the leading jet has very distinct characteristics for beam-induced background events compared to hard-scatter events. The beam-induced backgrounds arrive approximately at the same time at the detector as the protons in the bunches and they travel parallel to the beam but at larger radii compared to the beam pipe.

The calorimeter-cell timing is calibrated such that particles generated at the interaction point arrive at time zero at any point in the calorimeter. The distance to the interaction point in z and radial (r) direction defines the time of flight, $t_{\mathrm{ToF}} = \sqrt{r^2 + z^2}/c$, of the particles which are assumed to traverse the detector with the speed of light from which in turn the relative time difference between calorimeter cells can be derived. The timing of the leading jet is shown as a function of the jet's pseudorapidity in Figure 7.4 for events which pass the 'loose' jet cleaning. The flat red band at 0 ns over the entire η range of the leading jet shows that the calorimeter timing is well calibrated as most jets arrive in time with a small spread of 1-2 ns. These in-time jets are mainly hard-scatter jets. Two arcs are associated with beam-induced background events. They span from $|\eta|$ around ± 2 to ∓ 1 and from 0 to -12.5 ns and cross each other in the centre of the detector at $\eta = 0$. These two arcs arise as the beam-induced backgrounds have to cover shorter distances as they are not required to travel to the interaction point and from

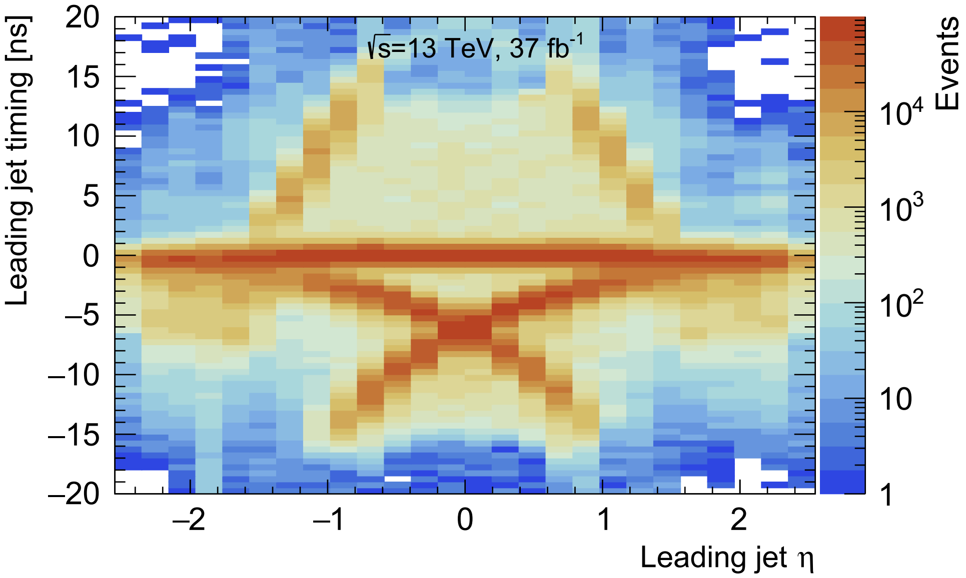

Figure 7.4: Leading jet timing as a function of leading jet η. The flat band at 0 ns is mainly attributed to the hard-scatter jets arriving in-time. The fake jets from the beam-induced background are reflected in the two arcs at negative times reaching up to -12.5 ns depending on where in the detector the muon is reconstructed as a jet. The timing cut-off at -12.5 ns is related to the trigger window which associates earlier times to the next bunch crossing where they occur as late jets.

there outwards. If they deposit their energy at the outermost parts of the calorimeter barrel before traversing the entire detector and assuming they arrive at small radii which can be neglected compared to the distance along the beamline, they can arrive as early as $t \approx -2|z|/c$. In the opposite case where they first traverse the entire detector and then interact with the calorimeter, they arrive approximately in time. This shows that the time offset with respect to the expected collision time depends on the position in the detector where the muon loses its energy via radiative processes. The time difference between the beam-induced background and the hard-scatter collision particles can hence be quantified as $\Delta t = \pm z/c - t_{\mathrm{ToF}}$ depending on the direction in which the detector is traversed. The curvature of the arcs depends on the radial distance between the interaction point and the position of the reconstructed jet within the calorimeter.

The sharp cut-off at -12.5 ns can be explained by the trigger which defines the maximum time window in which the jet is matched to the bunch crossing. Jets that arrive before this cut-off are associated with the following bunch crossing in which they arrive late. These jets can be seen in the two arcs spanning from about $0.8 < |\eta| < 1.5$ for positive values of the jet timing.

The timing information of the reconstructed jets is used to estimate the remaining background contribution after the application of the tight jet cleaning requirement. Following the approach outlined in [119] a background-enriched control region is defined in which the tight jet cleaning criterion is inverted. The leading jet timing in this background-enriched control region is shown in Figure 7.5. Two main features can be

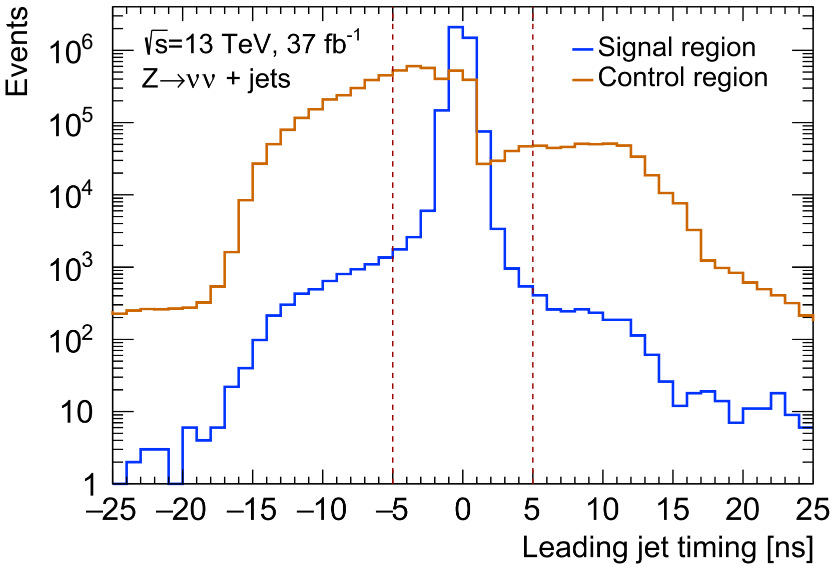

Figure 7.5: Leading jet timing in the $Z \to \nu\nu +$ jets signal region (blue) which is dominated by hard-scatter jets and in a beam-induced background enriched control region (orange) which is obtained by inverting the tight jet cleaning requirement. Beam-induced fake jets arrive typically early and are out-of-time. A tagging efficiency of jets falling outside of the $|t| > 5\,\text{ns}$ boundary indicated by the dashed red lines is derived to estimate the beam-induced background in the signal region.

extracted from this distribution. The number of events decreases exponentially for an increasing time difference to the expected arrival time and the arising shoulders have a clear asymmetry between negative and positive timing offsets. This is expected as the late jets correspond to early jets matched to the next bunch crossing.

These shoulders can also be observed in the signal region which indicates that some background events circumvent the tight cleaning selection. A tagging efficiency is there-

$p_{\mathrm{T},Z}$ Bin [GeV]	BIB Estimate	Relative Contribution [%]
130-170	36764	1.70
170-210	7641	0.83
210-250	1871	0.48
250-300	648	0.33
300-380	134	0.13
380-470	33	0.10
>470	<4	0.02
Combined	47095	1.26

Table 7.1: Beam-induced background estimate in the $Z \to \nu\nu+$jets signal region to which a conservative uncertainty of 100% is assigned.

fore derived in the background-enriched region by comparing the number of out-of-time jets defined as the jets which fall outside the time interval from -5 to 5 ns to the overall number of events in this control region. The tagging efficiency is determined separately for early ($t < -5\,\mathrm{ns}$) and for late jets ($t > 5\,\mathrm{ns}$) which are reconstructed in the next bunch crossing. These tagging efficiencies are used to scale the out-of-time events in the signal region. The equation for the background estimation of the early jets is given by the following equation and the late beam-induced background estimate follows analogously:

$$n_{\mathrm{BIB}}(t < -5\,\mathrm{ns}) = n_{\mathrm{SR}}(t < -5\,\mathrm{ns}) \times \frac{n_{\mathrm{CR}}(\mathrm{inclusive})}{n_{\mathrm{CR}}(t < -5\,\mathrm{ns})} \ . \tag{7.1}$$

The combined number of estimated beam-induced background events together with the relative contribution of this background to the $Z \to \nu\nu+$jets yield is summarised in Table 7.1 as a function of $p_{\mathrm{T},Z}$. It can be seen that this background contribution falls exponentially as the muons faking the jet plus $E_{\mathrm{T}}^{\mathrm{miss}}$ signature are required to deposit significantly more energy to populate the higher $p_{\mathrm{T},Z}$ region. Following the approach taken in [119], a conservative uncertainty of 100% is assigned to this background estimate which has a small impact on the final result as the background drops rapidly with $p_{\mathrm{T},Z}$.

7.2 QCD Multijet Background

Events with several jets and no reconstructed leptons are able to pass the $Z \to \nu\nu +$jets signal region selection even if no weak interaction or top decays take place in these collisions. This mainly happens when at least one jet in a multijet event either carries a relatively large fraction of its energy in the form of neutrinos from a heavy flavour decay or is mis-measured due to some detector effect. The fact that these two processes only happen rarely in such a strength that they produce sufficient $E_{\mathrm{T}}^{\mathrm{miss}}$ to populate the signal region is compensated by the very high cross section of the multijet production [92].

A distinct feature of this background however is that it is typically related to a fluctuation of a single jet and therefore $E_{\mathrm{T}}^{\mathrm{miss}}$ is often aligned with one of the jets, as depicted in the sketch in Figure 7.7 (b). This can be seen in data in Figure 7.6 where the azimuthal angular difference between $E_{\mathrm{T}}^{\mathrm{miss}}$ and the jet momentum in ϕ direction is shown for the leading (left) and sub-leading (right) jet in the $Z \to \nu\nu +$jets signal region without the selection requirement suppressing this background being applied. In the lower panels of the two distributions, it can be seen that the data overshoot the MC simulation by up to one order of magnitude in the region where the jet is closely aligned with $E_{\mathrm{T}}^{\mathrm{miss}}$ leading to $\Delta\phi$ values close to zero.

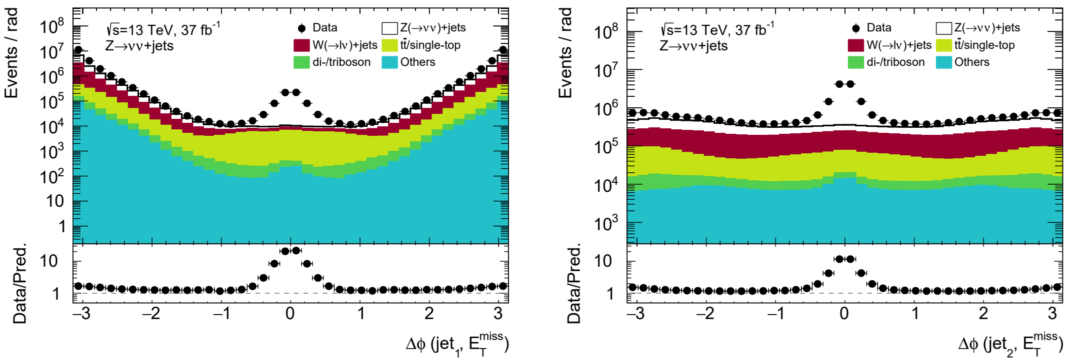

Figure 7.6: Comparison of the azimuthal angular difference of the leading (left) and sub-leading (right) jet and $E_{\mathrm{T}}^{\mathrm{miss}}$ between data and the MC simulation in the $Z \to \nu\nu +$jets signal region without the application of the angular cut suppressing the multijet contribution. The leading jet points in the opposite direction as $E_{\mathrm{T}}^{\mathrm{miss}}$ in most of the events. The lower panel shows the ratio of the data to the MC simulation where a clear deviation can be observed in the case where a jet is aligned with $E_{\mathrm{T}}^{\mathrm{miss}}$ which can be mostly attributed to the multijet background.

For events with at least one jet about 40% of the events observed in the data are not described by the considered MC simulations. This indicates the importance of a strong rejection of the described background together with a proper description of the remaining background. In the left panel of Figure 7.6 it can be seen that the leading jet points preferably in the opposite direction of $E_{\mathrm{T}}^{\mathrm{miss}}$. This can be understood as the vector boson in general recoils against a highly energetic jet to obtain a sufficient boost to pass the event selection. The sub-leading jet has a more homogeneous spectrum where a back-to-back topology is still preferred for the modelled processes whereas the data peaks around zero. In a multijet event where the leading jet is reconstructed with a strong downward fluctuation in its response, the leading jet can become the sub-leading jet with the $E_{\mathrm{T}}^{\mathrm{miss}}$ vector pointing in the same direction. For a small angular separation of the leading jet and $E_{\mathrm{T}}^{\mathrm{miss}}$ the largest SM contribution is $t\bar{t}$ pair production. In these events either the most energetic jet from the top decays has a smaller reconstructed momentum than the true jet momentum or the jet pointing in the opposite direction is reconstructed with a too large response. This is partially driven by semileptonic heavy flavour decays of tops, where neutrinos carry a significant fraction of the jet momentum.

The correlation between the jet and the $E_{\mathrm{T}}^{\mathrm{miss}}$ directions motivates the application of a $\Delta\phi\left(\text{jet}, E_{\mathrm{T}}^{\mathrm{miss}}\right) > 0.4$ separation requirement between $E_{\mathrm{T}}^{\mathrm{miss}}$ and any jet. This requirement rejects the majority of the multijet background by removing the event if any jet falls within this $\Delta\phi$ range, while this selection only rejects about 7.5% of the signal events.

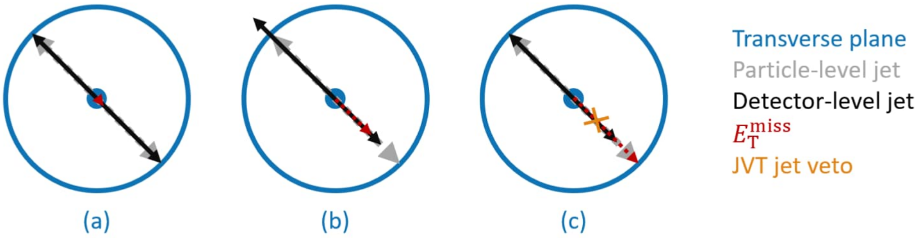

Figure 7.7: Sketch of a well-measured dijet event used as seed event (a), a multijet event with $E_{\mathrm{T}}^{\mathrm{miss}}$ from mis-measured jet momenta (b), and a multijet background event from a combination of a mis-measured jet momentum and a false removal of this hard-scatter jet via the jet vertex tagging (c), in the transverse plane of the detector. The magnitudes of the dashed grey arrows indicate the size of the true transverse jet momenta (particle level) whereas the black arrows indicate the reconstructed p_{T} of the jets. The magnitude of $E_{\mathrm{T}}^{\mathrm{miss}}$ is represented by the dotted red arrows. The orange cross depicts the removal of the black hard-scatter jet pointing downwards.

In particular, at small values of $p_{\mathrm{T},Z}$ an additional source of background becomes relevant which is related to inefficiencies of the (forward) jet vertex tagging enabling multijet events to pass the $Z \to \nu\nu + \text{jets}$ signal region selection. A combination of a fluctuation in the jet response with a related false removal of a hard-scatter jet by the (f)JVT cleaning can lead to sufficient $E_{\mathrm{T}}^{\mathrm{miss}}$ to pass the $Z \to \nu\nu + \text{jets}$ signal region selection. This is indicated in the right sketch of Figure 7.7 where the jet momentum is first reconstructed with a too small momentum such that the jet vertex tagger can falsely remove the hard-scatter jet if the reconstructed p_{T} falls within the application range of the JVT below 60 GeV. This background is not rejected by the $\Delta\phi\left(\mathrm{jet}, E_{\mathrm{T}}^{\mathrm{miss}}\right)$ requirement as the jet aligned with $E_{\mathrm{T}}^{\mathrm{miss}}$ is removed. The above signature can also be generated by the false removal of several low p_{T} jets recoiling against a high p_{T} jet or by the removal of a jet and a down (up) fluctuation in the momentum reconstruction of a jet pointing in the same (opposite) direction. These background sources which manifest themselves in particular at low $E_{\mathrm{T}}^{\mathrm{miss}}$ are suppressed by an event veto which rejects all events in which a jet is removed by any vertex tagging requirement. This event veto rejects an additional amount of 4% of the data in the first $p_{\mathrm{T},Z}$ bin, which ranges from 130-170 GeV, compared to a 6% baseline reduction of the $Z \to \nu\nu + \mathrm{jets}$ signal sample and the overall data. The introduced inefficiency is later corrected by the detector correction. The case where a pile-up jet circumvents the vertex tagging selection cannot be easily identified in data but is in principle also expected to provide a small contribution to this background.

A simulation-based estimate of the remaining background due to fluctuations in the jet response is because of two reasons not feasible. The large multijet cross section is directly related to an impractical large set of simulated events which are required to achieve a reasonable modelling of these events. Furthermore, MC simulations lack a precise description of high jet multiplicity environments and, more importantly, the detector effects are not well enough known and modelled at a sufficient precision to capture the non-Gaussian response effects which drive this background. The jet smearing method [120] is therefore employed as a data-driven estimation technique of this background and is introduced in the following section.

The Jet Smearing Method

The main idea of the jet smearing method is to generate a pseudodata set from well-measured seed events in which every jet momentum is smeared according to a derived jet response function which is tuned to correctly describe the data. The characteristics of such a seed event are sketched in Figure 7.7 (a), where the measured jet p_{T} is in agreement with the truth (particle level) jet p_{T} and where the event only has a minimal amount of $E_{\mathrm{T}}^{\mathrm{miss}}$. From the pseudo-dataset, two templates are extracted for the signal region and for a background enriched control region. For the control region the separation between the jets and $E_{\mathrm{T}}^{\mathrm{miss}}$ is inverted to select events where at least one jet is within $\Delta\phi < 0.3$

of $E_{\mathrm{T}}^{\mathrm{miss}}$. The templates are then normalised in the control region and a transfer factor is used to obtain the normalisation in the signal region.

The rejection of the main component of the multijet background related to jet vertex tagging supports the assumption that $E_{\mathrm{T}}^{\mathrm{miss}}$ is mainly related to fluctuations in the jet response for this background. The method relies on the independence of the response on the event topology which justifies the uncorrelated smearing of every jet in an event. Further, it is assumed that both fluctuations due to detector effects and the invisible component of heavy flavour decays can be expressed in a single response function which is applicable to all jets. These assumptions are checked by the construction of a validation region which lies between the signal and the control region.

The response is derived from isolated jets ($\Delta R > 0.2$) which are matched within $\Delta R < 0.1$ to a truth (particle level) jet. MC simulations of multijet events are used as they overall describe the response measured in data which is defined as

$$\mathcal{R} = \frac{p_{\mathrm{T}}^{\mathrm{reco}}}{p_{\mathrm{T}}^{\mathrm{truth}}} , \tag{7.2}$$

where the truth jet p_{T} is calculated from all stable final state particles in a cone of radius 0.4 with the anti-k_t clustering algorithm. These truth jets in particular also include neutrinos to quantify the response due to the invisible part of the jet. The jet response is known to be broader in data than in the MC simulation and is smeared by a Gaussian function to match the data [88]. The MC simulation lacks the ability to describe the non-Gaussian tails with a sufficient precision. A multijet enriched control region is therefore employed to adjust the response in the MC simulation to the one measured in the data. This is important as the low rate at which jets are smeared by these tail responses is compensated by the size of the resulting fluctuations in the jet momentum. These sizeable fluctuations lead to $E_{\mathrm{T}}^{\mathrm{miss}}$ values which are large enough to pass the $Z \to \nu\nu +$jets signal region selection. The corresponding response function is determined and provided by the ATLAS collaboration as a function of the truth jet p_{T} and is shown in Figure 7.8. The presented response function slightly indicates that jets are more likely smeared towards lower momenta. The small discontinuities seen in the response function are related to a sliced production of the MC simulation in truth jet p_{T} to ensure adequate statistics, especially at high jet momenta.

The seed selection of events used in the smearing method including studies showing that the selection does not introduce any significant bias was intensively studied in [23] and the key characteristics are summarised in the following. The principal objective is

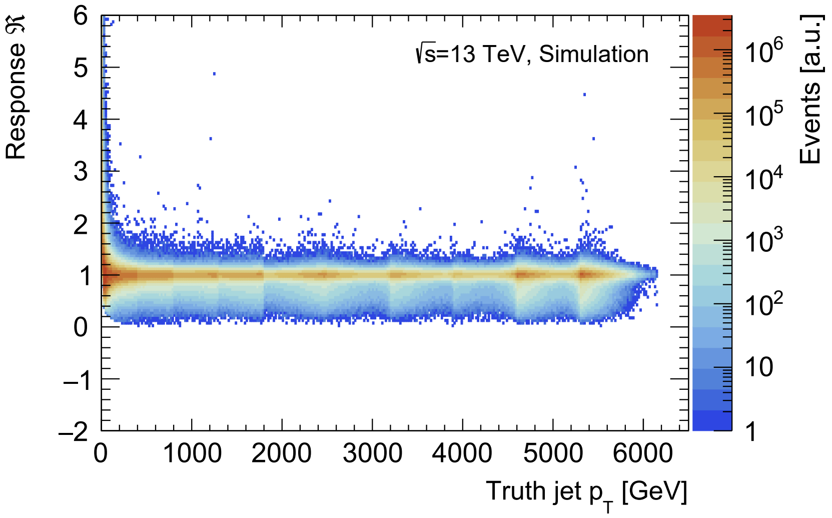

Figure 7.8: Corrected jet response $\mathcal{R}$ as a function of the truth jet p_T used to smear the jets in the seed data set. The production of the MC simulation is sliced in several samples in truth jet p_T which can be seen as small discontinuities on the slice boundaries.

to find a data set of multijet events where all jets have only minor fluctuations in their respective responses.

Events are required to contain at least two jets and no reconstructed lepton. The transverse momentum requirement of objects to be reconstructed as a jet is loosened to 20 GeV as such low energetic objects can pass the 30 GeV jet p_T threshold if multiplied by a sufficiently large response during the jet smearing. The minimum p_T of the leading jet needs to be larger than 50 GeV. This provides sufficient space for jets being smeared such that they exceed the $p_\mathrm{T} > 110\,\mathrm{GeV}$ threshold to pass the signal region selection. Jets below this threshold pass this requirement only to a negligible fraction. Single jet triggers which are fully efficient above 50 GeV are used to select the events. The lowest jet trigger satisfying this requirement is the HLT35 jet trigger which becomes fully efficient at 49.5 GeV. Additional jet triggers are chained to obtain a statistically adequate data set as the low p_T jet triggers are heavily prescaled. The lowest unprescaled jet trigger which is considered is the HLT380 trigger which only becomes fully efficient at 436 GeV [111]. Events selected by prescaled jet triggers are corrected by the multiplication of the inverse of the smallest prescale weight which still triggers the event.

A straightforward approach to ensure that the response of every jet in an event is within the Gaussian core of the response function is the introduction of a requirement on $E_{\mathrm{T}}^{\mathrm{miss}}$. Selecting events with almost no $E_{\mathrm{T}}^{\mathrm{miss}}$ would typically guarantee that the reconstructed jet p_{T} is close to the true jet. This in turn ensures that no fluctuations in the jet response are smeared which would lead to a biased pseudodata set. In [120] it is however shown that a cut on $E_{\mathrm{T}}^{\mathrm{miss}}$ itself introduces a bias of the p_{T} distribution of the selected jets. This can be understood as the $E_{\mathrm{T}}^{\mathrm{miss}}$ resolution is correlated with the transverse energy scalar sum of the event, $\sum E_{\mathrm{T}}$. The $E_{\mathrm{T}}^{\mathrm{miss}}$ significance S is shown to reduce this dependence [120] and is used to select events with small $E_{\mathrm{T}}^{\mathrm{miss}}$:

$$S = \frac{E_{\mathrm{T}}^{\mathrm{miss}}}{\sqrt{\sum E_{\mathrm{T}}}} < 0.5\,\mathrm{GeV}^{1/2}. \tag{7.3}$$

The presence of a smooth jet p_{T} spectrum in the seed sample, in particular, due to the trigger prescales and the absence of any bias in the p_{T} and jet multiplicity was studied by following the approach outlined in [23].

The pseudodata set is generated by multiplying the four-momentum of each jet in a seed event by a randomly chosen value from the response function. Every selected seed event is used 2000 times to generate a sufficiently large set as the fluctuations in the response which typically drive a multijet background event occur only rarely. These rare fluctuations related to responses outside the Gaussian core mainly lead to large shifts in the jet momenta. This pseudodata set is then used to derive shape templates for the $Z \to \nu\nu +$jets signal region as well as for a background enriched control region which is used to determine the corresponding normalisation of the template.

The control region differs from the $Z \to \nu\nu +$jets signal region by the inversion of the angular separation requirement to suppress the multijet background. The multijet control region with at least one jet within $\Delta\phi\,(\mathrm{jet}, p_{\mathrm{T},Z}) < 0.3$ is shown in Figure 7.9. The disagreement between the data and the MC simulation without the inclusion of the multijet background estimate can be seen in blue in the lower panel. This shows in particular that the majority of the multijet background is located at low $E_{\mathrm{T}}^{\mathrm{miss}}$. In the first bin, the control region is dominated by about 80% of multijet background events. The multijet template is normalised such that the integral of the template matches the total number of events measured in data from which the Standard Model processes considered in Figure 7.9 are subtracted. The template represents the shape of the multijet background well as no large deviations between data and MC simulation are observed in the black ratio in the lower panel which includes the normalised multijet background.

A validation region is used to verify the normalisation obtained in the control region

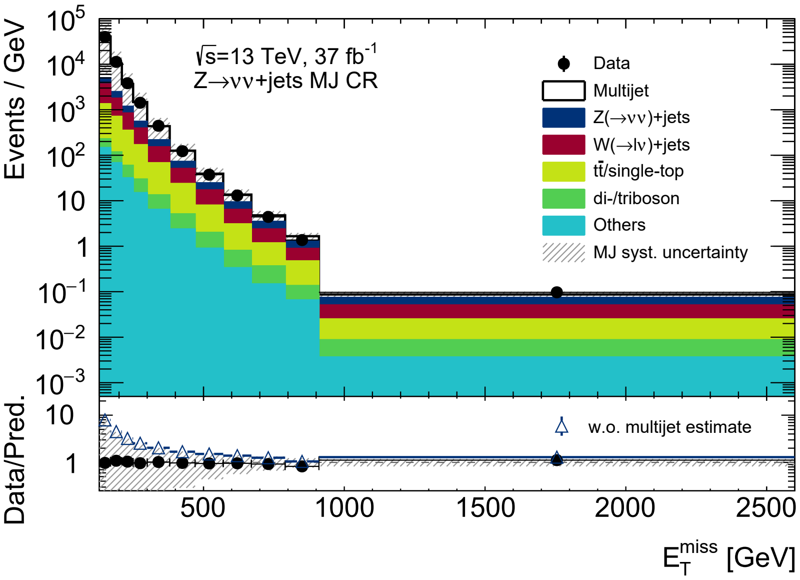

Figure 7.9: $E_{\mathrm{T}}^{\mathrm{miss}}$ distribution in the multijet enriched control region used to derive the multijet background normalisation. The multijet background is shown in white and the corresponding uncertainty is shown as the grey hashed bands whereas error bars on the data represent the statistical uncertainty. The agreement between the data and the MC simulation is shown in the lower panel in black (blue) including (excluding) the multijet estimate. The nearly perfect agreement between the data and the MC simulation including the multijet background comes by construction.

by selecting events where a jet falls within the range of $0.3 < \Delta\phi\,(\mathrm{jet}, p_{\mathrm{T},Z}) < 0.4$. The corresponding template is normalised by the same scale factor derived in the control region and also used in the $Z \to \nu\nu +$jets signal region. The $E_{\mathrm{T}}^{\mathrm{miss}}$ dependence of the multijet background in the validation region can be seen in Figure 7.10. It accumulates at small $E_{\mathrm{T}}^{\mathrm{miss}}$ values where the data overshoots the MC simulation by a factor of about three if the multijet background is not considered as can be seen in the lower panel in blue indicating that the validation region is also enriched in multijet events. The overall agreement between the data and the MC simulation is good and within the systematic uncertainties of the background estimate as soon as the multijet contribution is considered as shown by the black ratio in the lower panel. The deviation in the high $E_{\mathrm{T}}^{\mathrm{miss}}$ tail is covered within the statistical uncertainties of the measured distribution.

The multijet background in the $Z \to \nu\nu +$jets signal region, $N_{\mathrm{MJ}}^{\mathrm{SR}}$, is analogously derived as in the validation region and the estimate in bin i is calculated as

$$N_{\mathrm{MJ}}^{\mathrm{SR,i}} = \frac{N_{\mathrm{MJ}}^{\mathrm{CR}}}{N_{\mathrm{MJ,\ temp}}^{\mathrm{CR}}} \times N_{\mathrm{MJ,\ temp}}^{\mathrm{SR,i}}\ . \tag{7.4}$$

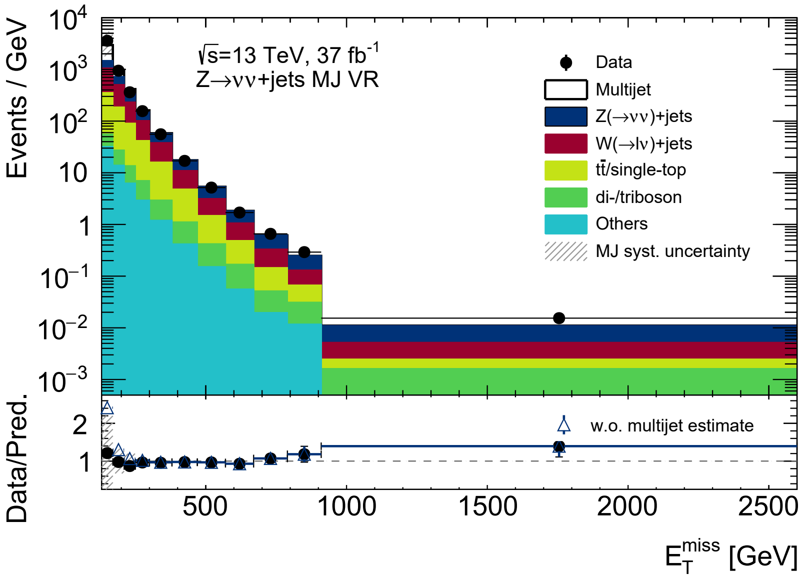

Figure 7.10: $E_{\mathrm{T}}^{\mathrm{miss}}$ distribution in the multijet validation region used to verify the multijet background normalisation. The multijet background is shown in white and primarily accumulates at low $E_{\mathrm{T}}^{\mathrm{miss}}$. The corresponding uncertainty is shown as the grey hashed bands whereas error bars on the data represent the statistical uncertainty. The agreement between the data and the MC simulation is shown in the lower panel in black (blue) including (excluding) the multijet estimate. The good agreement between the data and the MC simulation within the respective uncertainty serves as validation of the multijet template and the corresponding normalisation factor.

The transfer factor from the control to the signal region is defined as the total number of events in the control region measured in data from which the SM background MC simulations are subtracted, $N_{\mathrm{MJ}}^{\mathrm{CR}}$, divided by the integral of the multijet template in the control region, $N_{\mathrm{MJ,\ temp}}^{\mathrm{CR}}$. The multijet background estimate is obtained by multiplying the signal region multijet template with the transfer factor. The result is presented in Table 7.2. In addition to the absolute number of estimated background events the relative contribution of this background is also stated. From the relative contribution, it becomes evident that the relevance of this background decreases exponentially and falls below 1% for $p_{\mathrm{T},Z}$ above 250 GeV. The total contribution of this background to the $Z \to \nu\nu +$jets signal region is 5.26% which is mainly driven by the first bin which also contains the largest overall number of events. The estimated background contribution in the first $p_{\mathrm{T},Z}$ bin is non-negligible (7.71%) and an enlargement of the $\Delta\phi\left(\mathrm{jet}, E_{\mathrm{T}}^{\mathrm{miss}}\right)$ cut to 0.6 was studied for this first bin to potentially reduce the background contribution but no significant improvement was found.

A conservative uncertainty of 100% of the event yield of the multijet background is

$p_{\mathrm{T},Z}$ Bin [GeV]	Multijet Estimate $N_{\mathrm{MJ}}^{\mathrm{SR,i}}$	Relative Contribution [%]
130-170	167163	7.71
170-210	22104	2.40
210-250	4614	1.19
250-300	1493	0.75
300-380	121	0.11
380-470	22	0.07
470-570	5	0.05
>570	<1	0.01
Combined	195522	5.26

Table 7.2: Multijet background estimate in the $Z \to \nu\nu +$jets signal region to which a conservative uncertainty of 100% is assigned.

assigned to the estimate to cover systematic uncertainties associated with the smearing method following [119] which are among others related to the non-Gaussian tails, the general response function or biases in the seed selection [120].

7.3 The $W \to \ell\nu+$jets Background in the $Z \to \nu\nu+$jets Signal Region

The $Z \to \nu\nu+$jets signal region contains only about 47% signal events, where a Z boson decays into a pair of neutrinos. A vast number of events assigned to this signal region stem from $W \to \ell\nu+$jets processes, where the lepton is either not contained within the selected phase space (out-of-acceptance) or not correctly reconstructed and identified as a baseline electron (out-of-efficiency). Both can result in events passing the $Z \to \nu\nu+$jets signal region requirements as these leptons are not able to activate the event veto. The required $E_{\mathrm{T}}^{\mathrm{miss}}$ for passing the signal region selection is mainly coming from the transverse momentum of the four-vector sum of the neutrino and the non-reconstructed lepton. The leptonic W boson decays contribute roughly 38% to the total number of events in the $Z \to \nu\nu+$jets signal region as shown in Figure 7.1. The uncertainties on the cross section of the W+jet production from the renormalisation and factorisation scale uncertainties range between 13-20% from low to high $p_{\mathrm{T},Z}$. This necessitates a dedicated treatment of these background events as unconstrained they would lead to an uncertainty of at least 5% on the final result which is above the targeted precision of this measurement.

The $W \to \ell\nu+$jets events are not similarly distributed among the three fermion generations. This is in contrast to their similar production cross sections which are a result of the very similar branching ratios of leptonic W boson decays besides minimal effects related to the different fermion masses [1]. The contribution of W boson decays into taus is with about 21% two to three times larger than decays into muons (10%) and electrons (7%). This is a result of the lower identification efficiency for hadronic taus compared to the other two leptons [102, 105, 121], which leads to fewer event rejections in the $Z \to \nu\nu+$jets signal region from the lepton veto. The contribution of muons is slightly larger than for electrons, even if the muons have a higher identification efficiency, due to the $E_{\mathrm{T}}^{\mathrm{miss}}$ trigger requirement which is seldom fulfilled for electrons as these leave signatures in the calorimeter in contrast to muons (Chapter 6). In addition, the muons are able to populate a slightly larger phase space due to the transition region constraint applicable to the electrons (Section 5.2).

Two dedicated control regions enriched in either $W \to e\nu+$jets or $W \to \mu\nu+$jets events are defined to derive normalisation scale factors which are applied to the SM predictions obtained from the MC simulation in the $Z \to \nu\nu+$jets signal region. Both control regions require exactly one signal lepton with the same selections as the corresponding leading lepton in the $Z \to \ell\ell+$jets signal regions. The lepton p_{T} is required to be larger than 50 GeV to suppress background contributions. The events are therefore either selected by single electron triggers or in the case of the muon selection by the same $E_{\mathrm{T}}^{\mathrm{miss}}$ triggers used for the $Z \to \nu\nu$ + jets and $Z \to \mu\mu$ + jets signal regions. The lepton p_{T} is analogous to the $Z \to \ell\ell$ + jets signal region added to $E_{\mathrm{T}}^{\mathrm{miss}}$ to define $p_{\mathrm{T},Z}$ in the two control regions which actually represents a proxy for the transverse momentum of the W boson. The requirements on $p_{\mathrm{T},Z}$, the jet kinematics including the $\Delta\phi$ criteria between the jets and $p_{\mathrm{T},Z}$, and the event veto in the case of any additional baseline lepton are inherited from the $Z \to \nu\nu$ + jets signal region to reduce differences between these phase spaces. Both control regions restrict the transverse mass of the W boson, $m_{\mathrm{T}} = \sqrt{2p_{\mathrm{T}}^{\ell}E_{\mathrm{T}}^{\mathrm{miss}}(1 - \cos(\phi^{\ell} - \phi^{E_{\mathrm{T}}^{\mathrm{miss}}}))}$, to be within the interval ranging from $50 \leq m_{\mathrm{T}} \leq 110\,\mathrm{GeV}$ to enhance the relative contribution of $W \to \ell\nu$ + jets events. An additional selection of $E_{\mathrm{T}}^{\mathrm{miss}} < 50\,\mathrm{GeV}$ is necessary for the $W \to e\nu$ + jets control region to reduce background events related to electrons which cannot be attributed to direct boson decays, so-called fake lepton backgrounds which are described in the next section.

Figure 7.11 shows the $p_{\mathrm{T},Z}$ spectra for the $W \to e\nu$ + jets control region on the left panel and for the $W \to \mu\nu$ + jets control region on the right panel. The signal contribution in both regions is with 76% (78%) for W boson decays into electrons (muons) relatively high. The largest background contribution of roughly 18% (15%) are semileptonic single-top and $t\bar{t}$ decays, which intrinsically contain a W boson and are therefore difficult to reject. Other background processes are at the 1-2% level and originate from W decays into taus, di-/triboson processes and electroweak V+jet production. In the $W \to \mu\nu$ + jets control region, Z boson decays into muons are about 2% of the selected events. All these backgrounds combined contribute less than 23% of the total number of events and are directly taken from the MC simulations. The fake lepton backgrounds are derived via a data-driven technique and are at the 1% level in both regions. The lower panels present the agreement between the data and the predictions from MC simulations including the fake background contributions. The data are in good agreement with the MC simulation within the respective combined statistical and systematic uncertainties. The agreement is at the percent level at low $p_{\mathrm{T},Z}$ and the MC simulation exceed the data by up to 10% for some of the high $p_{\mathrm{T},Z}$ bins.

The scale factors are derived for each bin of the $p_{\mathrm{T},Z}$ spectra by dividing the number of background-subtracted data by the number of simulated signal events. Both the $W \to e\nu$ + jets and $W \to \mu\nu$ + jets distributions in the $Z \to \nu\nu$ + jets signal region are then scaled by the respective scale factors determined in the corresponding control region. They range from up to 1% for low values of $p_{\mathrm{T},Z}$ to about 10% in the high $p_{\mathrm{T},Z}$ tail. The number of data-driven events in the $Z \to \nu\nu$ + jets signal region in a bin i for

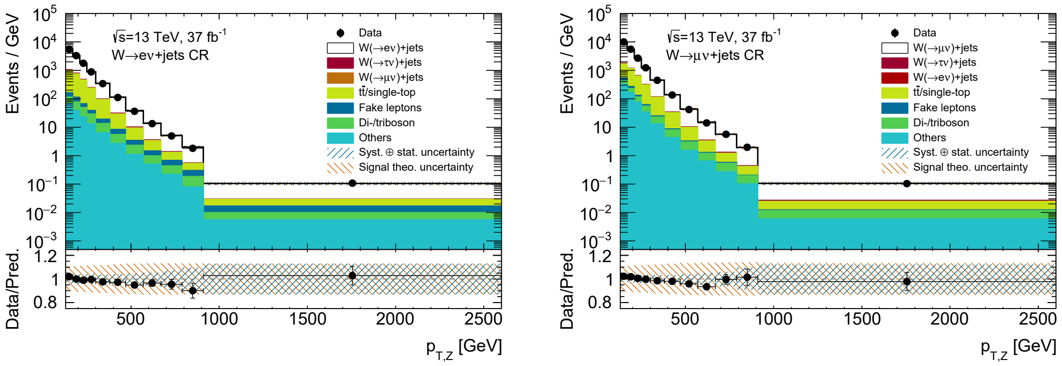

Figure 7.11: The $p_{\mathrm{T},Z}$ spectra are displayed for both the data and the MC simulation in the $W \to e\nu+$jets (left) and $W \to \mu\nu+$jets (right) control regions. The error bars on the data represent the statistical uncertainties, while the blue-hashed bands depict the combined statistical and systematic uncertainties. The theory uncertainties on the signal processes, presented in white, are shown as hashed orange bands. The lower panels illustrate the agreements between the data and the MC simulation, which lay within the corresponding uncertainty bands.

the $W \to \ell\nu+$jets process l is hence given by

$$N^{\text{data-drv}}_{\mathrm{SR}_i}\left(W \to \ell\nu+\text{jets}\right) = N^{\mathrm{MC}}_{\mathrm{SR}_i}\left(W \to \ell\nu+\text{jets}\right) \times \frac{N^{\text{data}}_{\mathrm{CR}_{\ell,i}} - N^{\text{bkg}}_{\mathrm{CR}_{\ell,i}}}{N^{\mathrm{MC}}_{\mathrm{CR}_{\ell,i}}\left(W \to \ell\nu+\text{jets}\right)} \ . \quad (7.5)$$

The event yields for the MC simulation of the $W \to \ell\nu+$jets process in the signal and (control) region are $N^{\mathrm{MC}}_{\mathrm{SR}_i(\mathrm{CR}_{l,i})}\left(W \to \ell\nu+\text{jets}\right)$, the number of measured events in the data in the $W \to \ell\nu+$jets control region is denoted as $N^{\text{data}}_{\mathrm{CR}_{l,i}}$ and the background events in this particular region are written as $N^{\text{bkg}}_{\mathrm{CR}_{l,i}}$.

For $W \to \tau\nu+$jets it is challenging to define a dedicated control region and the averages of the electron and muon scale factors are used instead. This is in parts motivated by the leptonic tau decays which can contribute to either the electron or muon $W \to \ell\nu+$jets control region. The larger contribution is nevertheless expected from hadronically decaying taus where the final-state neutrinos generate sufficiently large $E_{\mathrm{T}}^{\text{miss}}$ to pass the signal selection. The hadronic component of a non-reconstructed tau decay is often mis-identified as a hadronic jet and is therefore considered in the $E_{\mathrm{T}}^{\text{miss}}$ calculation similar to mis-identified electrons. The invisible component carried by the neutrino on the other side is similar to a missed muon which will not deposit much energy in the calorimeters. In this sense hadronically decaying taus can be seen as the midpoint between electrons and muons as they contribute to both the $E_{\mathrm{T}}^{\text{miss}}$ in the form of neutrinos and the jet activity via the hadrons. A validation region is hence defined which selects hadronically decaying taus passing a medium identification [104] to verify that the averaged scale factors are also applicable to the hadronic tau decays. This validation region is identical to the $Z \to \nu\nu +$jets signal region with the following adoption: exactly one hadronically decaying tau with medium identification and a $p_{\mathrm{T}} > 30\,\mathrm{GeV}$ is required. A subtle but important difference to any other control or signal region is that the p_{T} of the tau is not added to the $E_{\mathrm{T}}^{\mathrm{miss}}$ to obtain $p_{\mathrm{T},Z}$. This requirement is expected to reduce the number of fake hadronically decaying tau events which are difficult to estimate otherwise. The $E_{\mathrm{T}}^{\mathrm{miss}}$ distribution of this validation region is presented in Figure 7.12. The majority of the events selected in this region are attributed to $W \to \tau\nu +$jets events where the tau decays hadronically. The corresponding spectrum is weighted by the averaged scale factors. This is also the case for the minor background related to W boson decays into either electrons or muons. The single-top and $t\bar{t}$ decays, the di-/triboson processes as well as the remaining minor background contributions are directly taken from the MC simulations. In the lower panel, the ratio between the data and the MC simulation is shown which is overall in good agreement. In addition, the agreement is shown without the application of the scale factors. A slight improvement is seen with the scale factors applied, in particular at lower values of $E_{\mathrm{T}}^{\mathrm{miss}}$, which brings the MC simulation into better agreement with the data. This justifies the assumption that the averaged scale factors can be applied to the $W \to \tau\nu +$jets MC simulation in the $Z \to \nu\nu +$jets signal region.

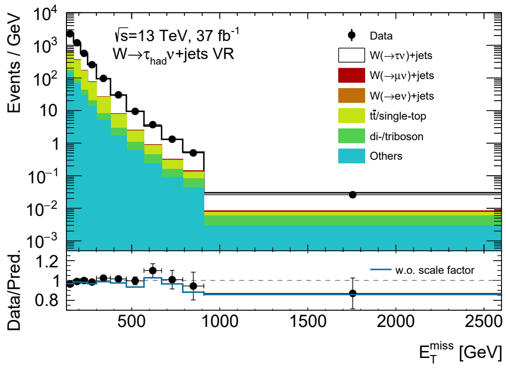

Figure 7.12: The $E_{\mathrm{T}}^{\mathrm{miss}}$ spectra are displayed for both the data and the MC simulation in the $W \to \tau\nu +$jets validation region. The error bars on the data represent the statistical uncertainties. The lower panel illustrate the agreement between the data and the MC simulation with (black) and without (blue) the scale factors being applied.

Statistical uncertainties on the scale factors are propagated onto the final result. In addition, an uncertainty on the definitions of the control regions is derived to account for differences between the signal and control regions. These differences are related to the phase space selection of the leptons as the hadronic recoil is in general expected to be similar in both regions besides effects where the lepton is close to a jet or out-of-acceptance. The stability of the scale factors is checked by varying the m_{T} selection to $30\,\mathrm{GeV} < m_{\mathrm{T}} < 100\,\mathrm{GeV}$. The corresponding uncertainty is derived by repeating the measurement with the varied scale factors. Variations of the lepton p_{T} are also tested but only have a negligible impact on the final result and are hence not considered. Table 7.3 states the total normalisation scale factor for each $W \to \ell\nu+\mathrm{jets}$ process including the corresponding statistical and systematic uncertainties. The total scale factors are close to 1 which indicates an overall good normalisation of the $W \to \ell\nu+\mathrm{jets}$ MC simulations.

Background	Normalisation
$W \to e\nu+\mathrm{jets}$	1.001 ± 0.004 (stat.) ± 0.005 (syst.)
$W \to \mu\nu+\mathrm{jets}$	1.012 ± 0.004 (stat.) ± 0.005 (syst.)
$W \to \tau\nu+\mathrm{jets}$	1.006 ± 0.004 (stat.) ± 0.005 (syst.)

Table 7.3: Total normalisation scale factors with statistical and systematic uncertainties for the data-driven $W \to \ell\nu+\mathrm{jets}$ background estimation in the $Z \to \nu\nu+\mathrm{jets}$ signal region.

Experimental and theoretical uncertainties on the scale factors are propagated onto the final result by repeating the derivation of the scale factors with the correspondingly varied spectra. These uncertainties are reduced as the $W \to \ell\nu+\mathrm{jets}$ MC simulations for the signal and the control region will be affected by the same systematic uncertainties with only subtle differences due to the slightly different phase spaces. They cancel to a large degree as becomes evident in the ratio $N^{\mathrm{MC}}_{\mathrm{SR}_i}/N^{\mathrm{MC}}_{\mathrm{CR}_{l,i}}$ encoded in the derivation of the data-driven estimates via Equation 7.5. Within this data-driven approach, sizeable systematic uncertainties on the $W \to \ell\nu+\mathrm{jets}$ MC simulations are replaced by smaller uncertainties on the ratio of the two MC simulations in the related signal and control region with an additional statistical component from the control region.

Finally, only the differences of the uncertainties between the signal and the control region and contributions from the subtracted background estimates via MC simulations remain, which are typically smaller than the uncertainties which would otherwise be directly attributed to the $W \to \ell\nu+\mathrm{jets}$ MC simulations in the $Z \to \nu\nu+\mathrm{jets}$ signal region. This indicates the strength of the application of such control regions to handle experimental and theoretical uncertainties as long as these regions are highly enriched in the respective signal processes.

7.4 Fake Lepton Backgrounds in the Lepton Signal and Control Regions

Both electrons and muons can be reconstructed from sources other than direct (prompt) decays of electroweak bosons selected in the signal and the control regions. Dedicated selection requirements are put in place to suppress leptons from hadron decays, photon conversions or jets faking the lepton signatures. A substantial fraction of these so-called 'fake' leptons still fulfil the lepton selection criteria for the signal and control regions containing leptons thereby making it necessary to estimate their corresponding background contributions.

A data-driven method is required to describe the fake lepton backgrounds as these are either induced by rare processes such as particle mis-identification, produced by particle decays during the showering or by particle interactions with the detector components, which makes it challenging to describe them by MC simulations with an adequate precision. The matrix method is used to derive estimates for the fake lepton backgrounds in the two lepton $Z \to ee+\text{jets}$ and $Z \to \mu\mu+\text{jets}$ signal regions as well as in the one lepton control regions ($W \to e\nu+\text{jets}$ & $W \to \mu\nu+\text{jets}$) introduced in Section 7.3. Before an introduction to the matrix method is given [121], the sources of fake leptons are discussed in more detail in the next section based on [121]. This follows a description of the extraction of the real and fake efficiencies required by the matrix method before the final estimate of this background with its respective uncertainties is laid out.

7.4.1 Fake Leptons

Identification, isolation and primary vertex requirements are placed on signal electron and muon candidates to reject leptons which do not have their direct origin in the hard-scatter interaction or are the direct decay products of a boson decay produced within the primary collision. These fake leptons can be assigned to two separate classes.

The first category includes mis-identified objects which are reconstructed as leptons. A prime example is a hadronic jet which deposits most of its energy already in a concise shower in the electromagnetic calorimeter with almost no leakage into the hadronic calorimeter. This ensures hadronic isolation and can therefore result in a reconstruction of this jet as an electron candidate. This mis-identification is often related to light flavour decays inside the tracking detector. Isolation requirements and shower shape variables in general show a strong rejection of contributions from hadronic jets during the electron identification. The very high rate at which multijet events are produced at the LHC still leads to a sizeable fraction of these events contributing to the overall background.

Neutral pions decaying into pairs of photons are a significant part of the hadrons faking electrons. The two photons can be collimated and reconstructed as a single electromagnetic cluster for a highly energetic pion. Photon conversions of one or both photons into electron pairs are able to provide the track matched to the electromagnetic cluster. A large fraction of these signatures are specifically suppressed in the particle identification by checking for a single instead of a two-peak structure in the energy cluster in the calorimeter [96], but some of those events remain present after this selection.

Hadronic jets are only rarely mis-identified as muons as these typically deposit minimal amounts of energy in the calorimeters. Additionally, hadrons need to penetrate through the calorimeter to reach the muon spectrometer to be identified as muons. This class of muons is called punch-through hadrons which is rejected via the jet-muon overlap removal, where muon candidates close to jet candidates with three or more tracks are removed, and by requiring the muons to be isolated.

In the second category physical leptons are present but they are part of a larger structure and are therefore assigned to an object differing from the true particle. Examples are semileptonic light or heavy flavour decays and photon conversions into lepton pairs. These leptons are referred to as non-prompt leptons as they stem from secondary vertices.

Muon candidates from light flavour decays mostly originate from in-flight semileptonic decays of charged kaons as most pions and kaons are already stopped within the calorimeter before they reach the muon spectrometer. These contributions are suppressed by isolation requirements as well as the compatibility of tracks reconstructed in the calorimeter and in the muon spectrometer. Also, electron candidates are produced non-promptly in hadron decays but otherwise have very similar signatures as prompt mis-identified jets.

Heavy flavour decays of bottom and charm quarks often produce non-prompt electrons or muons within the remnant of the corresponding jet. These non-prompt leptons can be separated from signal leptons by requesting that they originate from the primary vertex and fulfil isolation criteria.

The products of photon conversions into pairs of electrons and positrons in front of the tracking detector can be mis-identified as signal electrons if the leptons carry very asymmetric energy fractions or if one lepton does not leave enough hits for the track to be reconstructed. Both prevent the reconstruction of the conversion vertex which allows the distinction between electrons and photons. The origin of the photon itself is important to categorise the resulting electron as a fake candidate. Photons from initial-state radiation or jet fragmentation count as a potential source of non-prompt electrons in contrast to photons radiated from electrons due to bremsstrahlung or QED corrections which are considered to be part of the electrons.

In addition, leptonic tau decays are reconstructed as either muons or electrons where their reconstructed momenta are reduced by the momenta carried by the two neutrinos produced within the decay. The normalisation of hadronic decaying tau contribution is corrected using data (Section 7.3) and the MC simulation is assumed to be rigid enough that the same normalisation can be applied to the MC simulation of leptonically decaying taus.

Leptons falling either into the non-prompt or into the mis-identified category will be referred to as fake leptons in contrast to the electrons from the direct electroweak production of bosons with short-live times, such as the Z boson, which will be called real leptons.

In Figure 7.13 simulated relative contributions of electron (left) and muon (right) fakes to a Drell-Yan process with a very loose lepton selection are shown, where in particular no lepton-jet overlap removal is applied nor are the leptons required to be isolated or matched to the primary vertex [121]. The samples are further enriched in fake leptons by requesting two reconstructed leptons with the same electrical charge where the fake leptons have significant contributions as their charges tend to be uncorrelated.

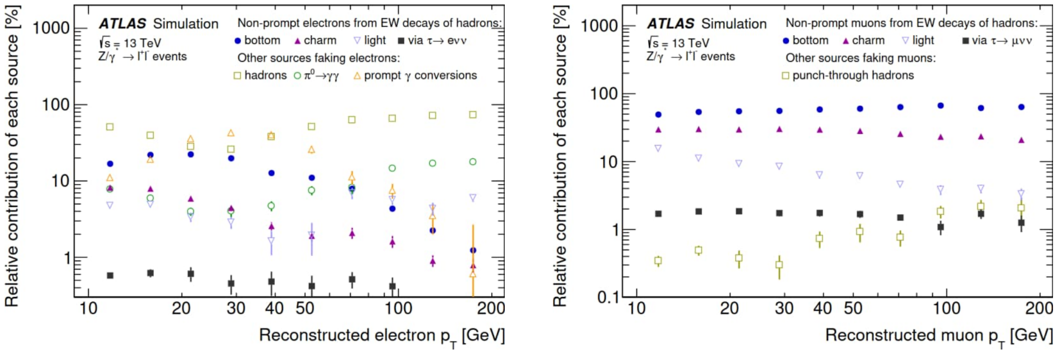

Figure 7.13: Relative composition of the main sources of electron (left) and muon (right) fakes in terms of the lepton p_{T} for a fake enriched Drell-Yan process. Statistical uncertainties are shown as error bars. Figures adopted from [121].

Muon fakes stem almost exclusively from non-prompt sources in particular from heavy flavour decays of bottom and charm quarks. Electron fakes on the contrary are more often related to the mis-identifications of hadrons or prompt photon conversions and for higher electron p_{T} also to π^0 decays into two photons. Non-prompt contributions of heavy and light flavour decays reach up to 30% and occur preferably at lower electron transverse momenta. The contributions are in general process dependent in addition to the dependence on the applied selection criteria [121]. Therefore, the fake efficiencies need to be determined specifically for every analysis and the fake enriched control regions should be close to the region for which the fake lepton background is derived. The various components of the fake leptons are difficult to model, in particular as they partially include non-perturbative QCD effects or depend on precise modelling of the interactions with the detector material. The restrictive selection criteria on the signal leptons lead in addition to a very limited rate of events passing the selections. These two limitations make the usage of a data-driven approach necessary. The matrix method is chosen as the primary method and is presented in the following.

7.4.2 Matrix Method

The matrix method allows the estimation of the number of fake leptons via a linear set of equations. These include the number of events passing the respective signal region selections, the number of events in the same signal region with loosened lepton selections requiring baseline leptons (Table 6.1) which explicitly fail the signal lepton criteria leading to a region with a higher fraction of fake leptons, as well as the efficiencies of real and fake baseline leptons to pass the signal lepton criteria, ϵ_{r} and ϵ_{f}.

The additional requirements placed on signal leptons compared to the baseline leptons are more restrictive identification criteria, isolation criteria, and track-to-vertex association ensuring that the lepton originates from the primary vertex. Signal leptons are hence a subset of the baseline leptons. Leptons which fulfil all baseline criteria defined in Section 5.2 and 5.4 but fail the more stringent signal lepton criteria are called Baseline-not-Signal (BnS) leptons. Both signal and baseline leptons contain fake leptons and the fraction of lepton fakes is expected to be larger in the baseline sample than in the signal sample as less restrictive selection criteria are applied. The real and fake efficiencies depend on the exact definitions of the signal and baseline leptons and will be derived in the next section.

In the $W \to e\nu+$jets and $W \to \mu\nu+$jets control regions, which select events with exactly one signal lepton and reject any events with an additional baseline lepton, the quantity of interest for the lepton fake estimate is the number of fake leptons passing the signal lepton selections in these control regions, $N_{\mathrm{f}}^{\mathrm{S}}$. This number is not directly accessible but can be written as the product of the number of events in the baseline sample N_f^B times the fake efficiency

$$N_\mathrm{f}^\mathrm{S} = \epsilon_\mathrm{f} N_\mathrm{f}^\mathrm{B} \ . \tag{7.6}$$

The number of events with a fake lepton in the baseline sample is not directly accessible from data but the following matrix relation provides a connection to the number of all events passing the signal lepton selection, N^S, and the number of events where the leptons fulfil the baseline but not the signal criteria, N^BnS, which both can be measured in data

$$\begin{pmatrix} N^\mathrm{S} \\ N^\mathrm{BnS} \end{pmatrix} = \begin{pmatrix} \epsilon_\mathrm{r} & \epsilon_\mathrm{f} \\ 1-\epsilon_\mathrm{r} & 1-\epsilon_\mathrm{f} \end{pmatrix} \begin{pmatrix} N_\mathrm{r}^\mathrm{B} \\ N_\mathrm{f}^\mathrm{B} \end{pmatrix} \ . \tag{7.7}$$

By inverting the matrix in Equation 7.7 N_f^B can be expressed as

$$N_\mathrm{f}^\mathrm{B} = \frac{1}{\epsilon_\mathrm{r} - \epsilon_\mathrm{f}} \left[\left(\epsilon_\mathrm{r} - 1 \right) N^\mathrm{S} + \epsilon_\mathrm{r} N^\mathrm{BnS} \right] \ . \tag{7.8}$$

This enables the assignment of weights to every event, w_evt, falling either in the signal or Baseline-not-Signal lepton category

$$w_\mathrm{evt} = \begin{cases} \frac{\epsilon_\mathrm{f,evt}(\epsilon_\mathrm{r,evt}-1)}{\epsilon_\mathrm{r,evt}-\epsilon_\mathrm{f,evt}}, & \text{if lepton fulfils signal criteria} \\ \frac{\epsilon_\mathrm{f,evt}\epsilon_\mathrm{r,evt}}{\epsilon_\mathrm{r,evt}-\epsilon_\mathrm{f,evt}}, & \text{if lepton fulfils Baseline-not-Signal criteria} \ , \end{cases} \tag{7.9}$$

where the efficiencies are selected to match the transverse momentum and pseudorapidity of the lepton in the event. The estimated numbers of fake lepton events in the $W \to \ell\nu + \mathrm{jets}$ control regions are then given by the sum of all event weights

$$N_\mathrm{f}^\mathrm{S} = \sum_\mathrm{evt} w_\mathrm{evt}. \tag{7.10}$$

Events with a signal lepton obtain negative weights as the real efficiencies are restricted to values below 1 and are therefore effectively subtracted from the Baseline-not-Signal estimate. The statistical uncertainty of this estimate is given by the square root of the sum of squares of the event weights which is a valid approximation in the limit of a large number of events. The statistical components of the related uncertainties to these fake background estimates are typically sub-leading compared to the systematic uncertainties related to the derivation of the efficiencies.

The 2 × 2 matrix in Equation 7.7 is extended to a higher dimensionality for the

$Z \rightarrow ee+$jets and $Z \rightarrow \mu\mu+$jets signal regions as here either one of the two signal leptons can be of fake origin. All three cases, where either the p_{T} ordered leading, the sub-leading or both leptons are fake, are attributed to the fake background, thereby modifying Equation 7.6 to

$$N_{\mathrm{f}}^{\mathrm{S}} = \epsilon_{\mathrm{r}_1}\epsilon_{\mathrm{f}_2}N_{\mathrm{r}_1,\mathrm{f}_2}^{\mathrm{B}} + \epsilon_{\mathrm{f}_1}\epsilon_{\mathrm{r}_2}N_{\mathrm{f}_1,\mathrm{r}_2}^{\mathrm{B}} + \epsilon_{\mathrm{f}_1}\epsilon_{\mathrm{f}_2}N_{\mathrm{f}_1,\mathrm{f}_2}^{\mathrm{B}} \ , \tag{7.11}$$

where the index 1 or 2 indicates the leading or sub-leading lepton. The number of events in the baseline sample in Equation 7.11 are now obtained by the inversion of the following 4×4 matrix using the same approach as in the one lepton case and by introducing the notation $1 - \epsilon = \tilde{\epsilon}$

$$\begin{pmatrix} N^{\mathrm{S,S}} \\ N^{\mathrm{S,BnS}} \\ N^{\mathrm{BnS,S}} \\ N^{\mathrm{BnS,BnS}} \end{pmatrix} = \begin{pmatrix} \epsilon_{\mathrm{r}_1}\epsilon_{\mathrm{r}_2} & \epsilon_{\mathrm{r}_1}\epsilon_{\mathrm{f}_2} & \epsilon_{\mathrm{f}_1}\epsilon_{\mathrm{r}_2} & \epsilon_{\mathrm{f}_1}\epsilon_{\mathrm{f}_2} \\ \epsilon_{\mathrm{r}_1}\tilde{\epsilon}_{\mathrm{r}_2} & \epsilon_{\mathrm{r}_1}\tilde{\epsilon}_{\mathrm{f}_2} & \epsilon_{\mathrm{f}_1}\tilde{\epsilon}_{\mathrm{r}_2} & \epsilon_{\mathrm{f}_1}\tilde{\epsilon}_{\mathrm{f}_2} \\ \tilde{\epsilon}_{\mathrm{r}_1}\epsilon_{\mathrm{r}_2} & \tilde{\epsilon}_{\mathrm{r}_1}\epsilon_{\mathrm{f}_2} & \tilde{\epsilon}_{\mathrm{f}_1}\epsilon_{\mathrm{r}_2} & \tilde{\epsilon}_{\mathrm{f}_1}\epsilon_{\mathrm{f}_2} \\ \tilde{\epsilon}_{\mathrm{r}_1}\tilde{\epsilon}_{\mathrm{r}_2} & \tilde{\epsilon}_{\mathrm{r}_1}\tilde{\epsilon}_{\mathrm{f}_2} & \tilde{\epsilon}_{\mathrm{f}_1}\tilde{\epsilon}_{\mathrm{r}_2} & \tilde{\epsilon}_{\mathrm{f}_1}\tilde{\epsilon}_{\mathrm{f}_2} \end{pmatrix} \begin{pmatrix} N_{\mathrm{r}_1\mathrm{r}_2}^{B} \\ N_{\mathrm{r}_1\mathrm{f}_2}^{B} \\ N_{\mathrm{f}_1\mathrm{r}_2}^{B} \\ N_{\mathrm{f}_1\mathrm{f}_2}^{B} \end{pmatrix} . \tag{7.12}$$

Events are classified into four disjoint categories ($N^{\mathrm{S,S}}, N^{\mathrm{S,BnS}}, N^{\mathrm{BnS,S}}, N^{\mathrm{BnS,BnS}}$) depending on their affiliation of the two leptons to signal or Baseline-not-Signal categories. Weights are then assigned to each event and all event weights are summed to derive the final fake lepton background estimates in the $Z \rightarrow \ell\ell+$jets signal regions.

The determination of real and fake efficiencies is evidently a key ingredient of the matrix method and will hence be discussed next.

7.4.3 Determination of Real and Fake Lepton Efficiencies

The real efficiencies for electrons and muons are derived in both the $W \rightarrow e\nu+$jets and $W \rightarrow \mu\nu+$jets control regions defined in Section 7.3 as they are assumed to be only marginal influenced by the event topology. The lepton p_{T} threshold is lowered from 50 GeV to 25 GeV in these control regions to also derive real efficiencies for the sub-leading lepton in the $Z \rightarrow ee+$jets and $Z \rightarrow \mu\mu+$jets signal regions. The fake efficiencies for the $W \rightarrow \ell\nu+$jets control regions are determined by slightly altering these two regions to increase the fractions of fakes.

Possible fake enriched regions which are close to the $Z \rightarrow \ell\ell+$jets signal regions are obtained by requiring either two same charge leptons in the $Z \rightarrow \ell\ell+$jets signal region or a third lepton in addition to the charged lepton pairs from the Z boson decay. These fake enriched regions have only minor SM contributions from mainly diboson processes.

However, they have very limited statistical precision and for the same charge region a non-negligible background contribution from leptons with a mis-reconstructed charge. The in these two regions obtained fake efficiencies are compatible within their statistical uncertainties with the fake efficiencies derived in the fake enriched $W \to \ell\nu + \text{jets}$ control regions. The control and the signal regions are in a sense kinematically close to each other as they both contain a highly energetic jet recoiling against a weak boson. For this reason, the modified $W \to \ell\nu + \text{jets}$ control regions are also used for the determination of the fake efficiencies for the fake lepton background estimates in the $Z \to \ell\ell + \text{jets}$ signal regions.

Real Lepton Efficiencies

The efficiencies of real leptons are well described in the MC simulation as they are calibrated for the specific identification and isolation working points via a tag-and-probe method relying for example on leptonic Z boson decay measurements [96, 100]. The residual differences between efficiencies determined in data and in MC simulations are corrected via dedicated scale factors which are applied as event weights for every lepton in the event. The MC simulation is therefore used to derive the real efficiencies in the required phase space. The $W \to e\nu + \text{jets}$ and $W \to \mu\nu + \text{jets}$ control regions defined in Section 7.3 are extended towards lower lepton p_{T} and used to derive the real efficiencies. Both baseline and signal leptons are required to be matched to a real prompt electron or muon in the truth event record of the MC simulation within $\Delta R < 0.2$. This ensures that no reconstructed fake leptons are considered in the calculation of the real efficiencies as the MC simulations contain some fake contributions. The efficiencies are binned in p_{T} and pseudorapidity of the leptons where the binning is set such that it matches the one from the fake efficiencies which in turn is set by constraints on the statistical precision. The efficiencies are then determined by the ratio of the number of events with the electron or muon passing the signal lepton criteria in the $W \to e\nu + \text{jets}$ and $W \to \mu\nu + \text{jets}$ control regions, $N_{\mathrm{r}}^{\mathrm{S}}$, to the number of events where the leptons fulfil the looser baseline criteria, $N_{\mathrm{r}}^{\mathrm{B}}$.

The left panel in Figure 7.14 presents the real efficiency, ϵ_{r}, as a function of p_{T} for electrons and muons. Several distinct features can be observed in the lepton p_{T} spectra. The most pronounced one is that the muon real efficiency is overall higher than the electron one as it increases from 96% at 25 GeV to 99% around 100 GeV. This is related to the fact that overall the muon identification is very efficient (above 97% for the signal identification [100]) and only changes by a relative 1-2% between the two different

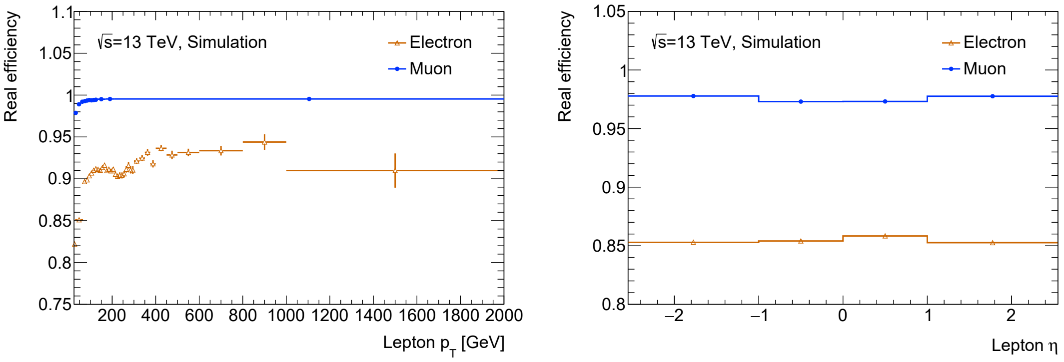

Figure 7.14: Real electron (orange) and muon (blue) efficiencies are presented as a function of the lepton p_{T} (left) and η (right).

identifications of the baseline and signal muons depending on the muon p_{T}. Between 25 GeV and 100 GeV the isolation efficiency of signal muons is 97% and increases above 99% for muons with larger transverse momenta [100]. The cited muon identification and isolation efficiencies were studied in top anti-top samples with high hadronic activity and can therefore be slightly higher in the $W \to \mu\nu +$jets environment.

The electron real efficiency rises from 82% at 25 GeV up to 94% at higher p_{T}. This is mainly attributed to the higher discrimination against the background for increasing electron p_{T} in the identification which rises faster for the tight identification than for the loose identification [98, 122]. The overall lower identification efficiency compared to muons results from the fact that electrons are mainly reconstructed from energy depositions in the electromagnetic calorimeter, where many other particles, in particular jets, leave similar signatures which need to be distinguished. Muons on the other side are mainly reconstructed from tracks inside the muon spectrometer where almost all other visible particles are stopped beforehand. The drop in the efficiency curve around 200 GeV is assigned to the calorimeter isolation which drops by several % in this transverse momentum range [97]. The efficiency rises again for electrons with p_{T} above 275 GeV where the p_{T} dependent definition of the isolation (Section 5.2) supersedes the static 3.5 GeV requirement on the allowed transverse energy in the cone around the electron [123].

The right panel in Figure 7.14 shows the real efficiencies as a function of the lepton η for electrons and muons. For electrons, ϵ_{r} is slightly larger in the central region ($|\eta| < 1$) compared to the forward region. Two competing effects lead to a slightly larger central efficiency. The identification efficiency has a convex shape which also propagates into the difference between the two identifications of the signal and baseline electrons [98].

The slightly higher identification efficiency in the central region is mainly related to the construction of the detector where less material distorting the electron showers is in front of the barrel than in the electromagnetic end-cap. The isolation efficiency in contrast has a concave shape which is slightly smaller in the central slice as the isolation selection is constructed such that it rejects mainly high p_{T} electrons which typically tend to be more central. It should be noted that even if the transition region lies within the outer η region, electrons falling within this region are neither considered in the baseline nor in the signal lepton selection due to the large amounts of passive material in this area leading to overall lower reconstruction efficiencies.

The muon efficiency in contrast is smaller in the central region than in the outer region which can be explained by the absence of combined muons in the very central region due to the up to 2 m wide gap in the centre of the muon spectrometer for the maintenance of the other detector systems (Section 3.2.3). In this central area, only calorimeter muons and segmented muons are reconstructed as part of the baseline lepton sample which per definition fail the signal region selection where only combined muons are considered (Section 5.4).

The real efficiencies for both electrons and muons are symmetric with respect to the centre of the detector which motivates the determination of the efficiencies in terms of the absolute η to improve the statistical precision of the real and fake efficiencies. The two-dimensional real efficiency maps for electrons (left) and muons (right) are shown in Figure 7.15. The statistical precision in the central region is typically higher. The real efficiencies required in Equations 7.7 and 7.12 to derive the estimate of the fake lepton background are taken from those maps depending on the momentum and $|\eta|$ position of each individual lepton.

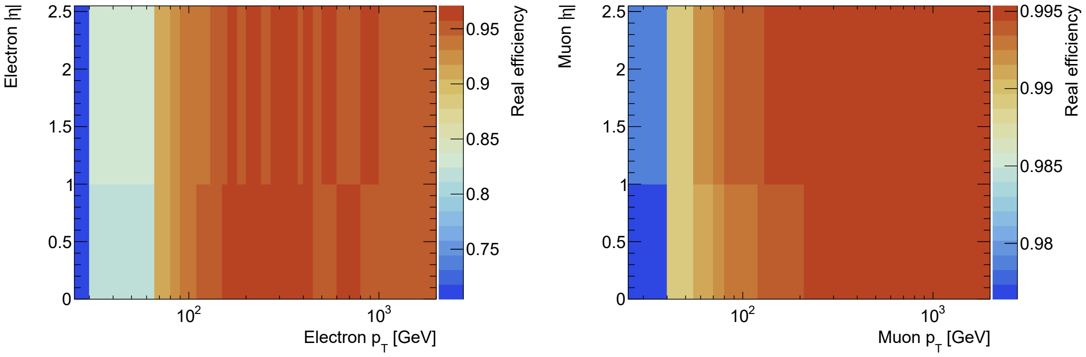

Figure 7.15: Real electron (left) and muon (right) efficiencies are presented as a function of the lepton p_{T} and $|\eta|$.

Fake Lepton Efficiencies

The fake efficiencies for electrons and muons are determined in control regions with enhanced contributions from fake leptons. Events with single leptons are chosen to derive the respective fake efficiencies and these fake enriched control regions are inspired by the $W \to \ell\nu +$ jets control regions defined in 7.3 which are modified such that the fraction of real leptons is reduced. Both fake enriched control regions will contain sizeable fractions of events with real leptons which are estimated via MC simulations for the baseline and the signal samples. These real events are subtracted from the data measured in the fake enriched control regions to calculate the ratio of the number of events with fake leptons passing the signal lepton selections over the number of events where the fake leptons pass the baseline lepton requirements.

The rate of fake leptons passing the signal lepton selection criteria depends among the identification, isolation, and primary vertex matching, on the momentum and the position of the particle. The efficiencies are derived in two pseudorapidity slices, a central ($|\eta| < 1.$) and a forward slice which ensures a sufficient statistical precision. They are not split in the azimuthal direction where the detector response is considered homogeneous. In addition, the efficiencies are determined as a function of the momenta of the lepton candidates with a finer binning for particles with smaller momenta where the fake and signal statistics are higher.

Fake Electron Efficiency

The number of events, in particular for electrons with small p_{T}, is increased in the fake enriched control region by dropping the $p_{\mathrm{T},Z}$ criterion of the $W \to e\nu +$ jets control region. The fraction of fake electrons compared to electrons from $W \to e\nu +$ jets production is additionally raised by not applying a selection on the invariant transverse mass of the W boson. The fake contributions are further enhanced by inverting the $E_{\mathrm{T}}^{\mathrm{miss}}$ criterion to $E_{\mathrm{T}}^{\mathrm{miss}} < 50\,\mathrm{GeV}$ which rejects parts of the W boson events as well as semileptonic top decays of $t\bar{t}$ events. The p_{T} requirement of the electron is lowered from 50 GeV to 25 GeV to derive fake efficiencies which can be applied to the sub-leading electron in the $Z \to ee +$ jets signal region.

The low electron p_{T} in combination with the loose identification requirement of the baseline lepton selection necessitates dedicated triggers. The main electron triggers used in this analysis are listed in Table 7.4. These single-electron triggers are all seeded by the same L1_EM22VHI Level-1 trigger. This trigger applies an E_{T} threshold of 22 GeV, a hadronic veto, a varying E_{T} threshold as a function of η to cope with the change of passive

Unprescaled Electron Triggers	E_T Threshold [GeV]	Identification	Isolation
HLT_e24_lhtight_nod0_ivarloose	24	tight	yes
HLT_e60_lhmedium_nod0	60	medium	-
HLT_e140_lhloose_nod0	140	loose	-
HLT_e300_etcut	300	-	-

Table 7.4: Main unprescaled electron triggers used in 2016 to select events in the $Z \to ee +$ jets ($W \to e\nu +$ jets) signal (control) region. Triggers with the 'nod0' tag apply no restrictions on the transverse impact parameters. The threshold of the trigger with the tight identification was increased to 26 GeV during the 2016 data-taking period to cope with a higher pile-up. The e300_etcut trigger is special as it only requires $E_T > 300$ GeV without placing any criteria on potential electron tracks.

material in front of the calorimeter, and an isolation requirement [57]. The hadronic veto and the isolation criterion are not applied for E_T values exceeding 50 GeV. The lowest unprescaled single electron trigger with loose identification requirements in 2016 is the HLT_e140_lhloose_nod0. This trigger is used to collect events containing an electron with $p_T > 150$ GeV where the trigger is fully efficient [112]. This trigger is chained with the HLT_e300_etcut trigger which places looser requirements on potential electron candidates. A set of support triggers with very loose identification requirements is used to collect events with low p_T baseline electrons to obtain a fake background enriched sample. These triggers are prescaled as the rates to collect these events are very high and are summarised in Table 7.5. Large weights of strongly prescaled triggers are reduced by restricting the triggers to the range until the trigger with the next higher E_T threshold guarantees a high trigger efficiency. The HLT_e60_lhvloose_nod0 trigger can be used even if it is seeded by the same isolated Level-1 trigger as the unprescaled single electron triggers as the interval in which this trigger is applied is above the threshold requiring isolation at Level-1. In 2015 low p_T triggers with loose identification were not constantly run with the same p_T thresholds throughout the corresponding data-taking period. The fake lepton estimate is therefore determined for the 2016 dataset and scaled via the

Prescaled Electron Trigger	Level-1 Seed	p_T Application Range [GeV]
HLT_e20_lhvloose	L1EM15VH	25-30
HLT_e26_lhvloose_nod0	L1EM20VH	30-66
HLT_e60_lhvloose_nod0	L1EM22VHI	66-150

Table 7.5: Prescaled single-electron triggers used to select events containing electrons with p_T below 150 GeV with their respective Level-1 seeds and the range of application in regard of the electron p_T.

measured integrated luminosity to provide an estimate for the $37\,\mathrm{fb}^{-1}$ considered in this measurement.

The transverse mass (top), $E_{\mathrm{T}}^{\mathrm{miss}}$ (mid) and the electron p_{T} (bottom) are shown in Figure 7.16 for the baseline (left) and signal electron (right) fake enriched control regions. The omission of the requirement of m_{T} to be within a $\pm\,30\,\mathrm{GeV}$ interval of the W boson mass increases the contribution of fake electron events which are not described by the considered MC simulations at small and large m_{T} in both regions. Events fulfilling the signal electron criteria have the largest fake contribution at low m_{T} values which are attributed to reconstructed low p_{T} electrons which are harder to differentiate from background sources such as hadronic jets. The increase to larger m_{T} values of the fake electron contribution is related to electrons with high transverse momenta due to the inversion of the $E_{\mathrm{T}}^{\mathrm{miss}}$ requirement which restricts $E_{\mathrm{T}}^{\mathrm{miss}}$ to values below $50\,\mathrm{GeV}$. These electrons often have their origin in mis-identified hadronic jets which pass the isolation requirements in the case of signal electrons.

Both baseline and signal electron fakes contribute most at very low $E_{\mathrm{T}}^{\mathrm{miss}}$. Events with almost no $E_{\mathrm{T}}^{\mathrm{miss}}$ are once more an indication of hadronic jet mis-identification. In contrast to heavy flavour decays, no energy is carried by invisible particles. The only sources of $E_{\mathrm{T}}^{\mathrm{miss}}$ in these events are small mis-measurements in the energies of the particles and a mis-calibration of the electron energy which is calibrated to the expected electromagnetic response instead of the hadronic response which has a marginal impact. Fake events with some amount of $E_{\mathrm{T}}^{\mathrm{miss}}$ can be an indication of non-prompt electrons from heavy-flavour decays where some of the energy is carried by the neutrinos present in the final state. These are partially included in the form of $t\bar{t}$ processes for which the contribution to the total SM prediction from MC simulation slightly increases towards higher $E_{\mathrm{T}}^{\mathrm{miss}}$.

At low baseline electron p_{T} the data is a factor of 20 larger than the MC simulation which indicates the presence of a large amount of fake electrons. For the signal electrons, this factor is smaller but still, the data exceeds the MC simulation by a factor of 5. These events are likely to be related to the mis-identification of hadronic jets which are stronger suppressed by the more restrictive identification criteria and isolation requirements. At very high transverse momenta this ratio increases to 30 in the baseline electron selection and is reduced to 2 for the signal electron selection. The corresponding fake electrons are quite efficiently suppressed with the signal electron selection. This is expected to be related to the isolation requirement which for example effectively rejects energetic jets and π^0 decays with hadronic activity around the lepton. In the intermediate range

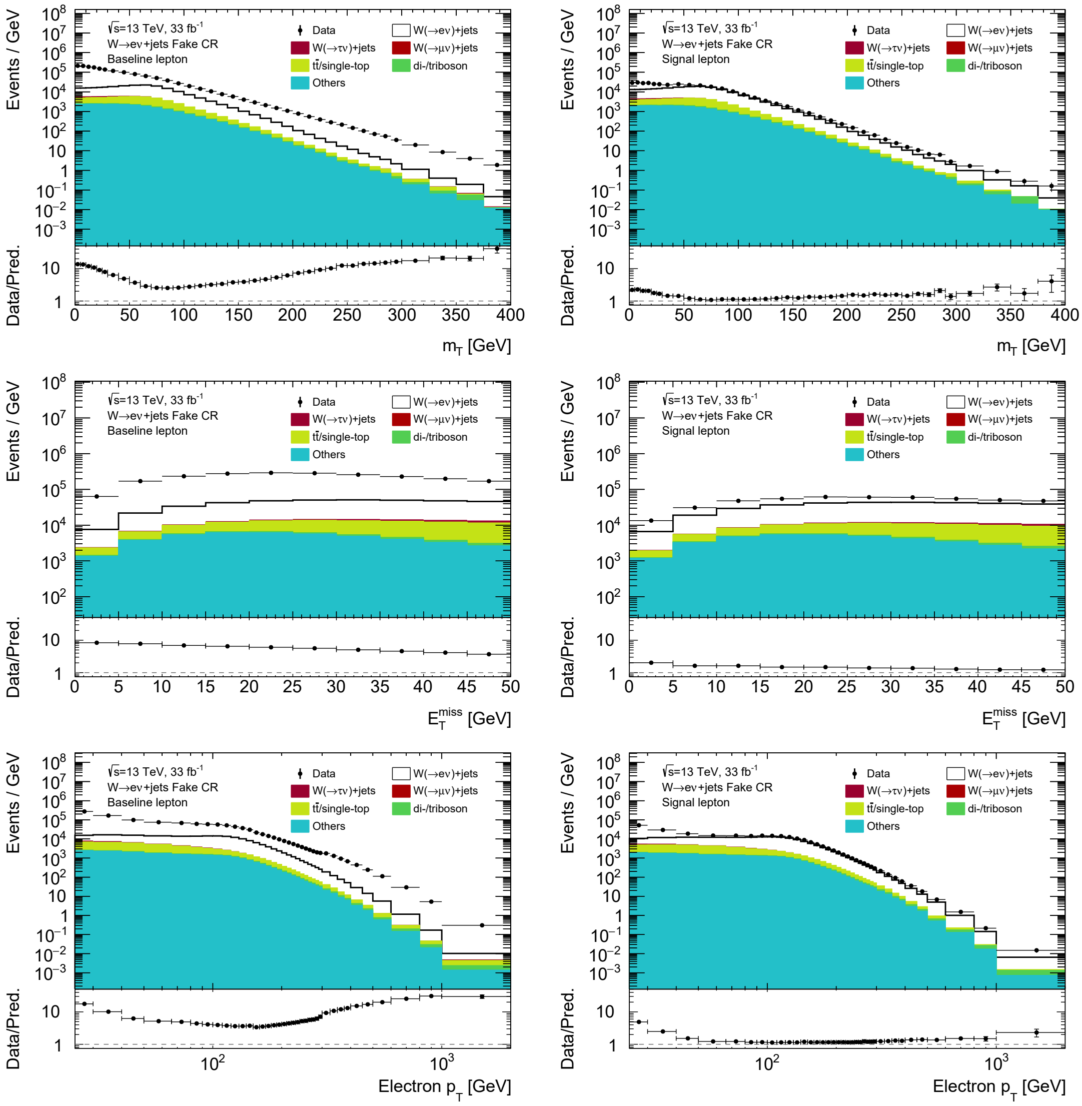

Figure 7.16: m_{T} (top), $E_{\mathrm{T}}^{\mathrm{miss}}$ (middle) and the electron p_{T} (bottom) spectra for data and the MC simulation in the fake enriched control region with a baseline electron (left) or a signal electron (right). The lower panels show the ratios of the data to the MC simulation where large deviations can be observed which are more pronounced for the baseline electrons. These differences between the data and MC simulation are attributed to the fake electron contributions which are present in the data. These fake electrons are used to derive the corresponding fake efficiencies.

from 80-300 GeV, almost no fake contributions are observed in the signal samples and for the baseline sample the ratio between data and MC simulation drops to a minimum of 3.5. The transverse momentum spectra of the electrons are also influenced by the applied electron triggers. In the spectrum of the baseline selection, a change of the exponentially falling slope can be observed for transverse momenta exceeding 300 GeV. This is attributed to the HLT_e300_etcut trigger which places less stringent requirements on the electrons. For the signal electrons, the rise due to this trigger is reduced by the overall stricter selection requirements.

The fake electron efficiency is obtained by dividing the number of fake events in the signal lepton control region by the number of fake events in the baseline lepton control region binned in p_{T} and $|\eta|$. The number of fake events is derived by subtracting the MC simulation event yields in the respective region from the corresponding observed events in the data. The binning is chosen such that every bin has sufficient statistics to calculate the fake efficiency. The fake efficiencies as a function of p_{T} and $|\eta|$ are shown in the left panel of Figure 7.17 and the projections onto the electron p_{T} are presented in the left panel of Figure 7.18 and for the electron η on the right panel. The projections are compared to the muon fake efficiencies.

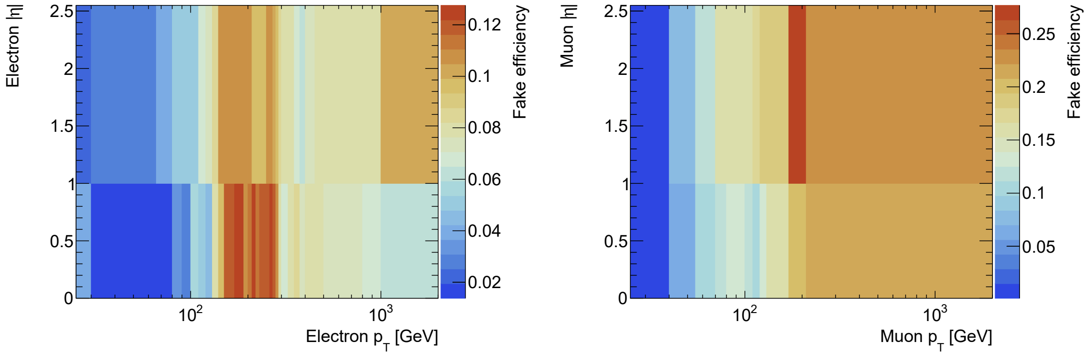

Figure 7.17: Fake electron (left) and muon (right) efficiencies are presented as a function of the lepton p_{T} and $|\eta|$.

For low electron p_{T} the fake efficiency reaches its maximum as the distinction between electrons and low energetic jets becomes more ambiguous. The efficiency drops for increasing electron p_{T} in the range covered by the prescaled triggers which have very loose identification requirements. The jump to a higher fake efficiency at 150 GeV is a feature of the change to the unprescaled HLT_e140_lhloose_nod0 trigger which applies a loose identification criterion and thereby slightly reduces the baseline sample as the trigger and reconstruction identification algorithms are not exactly identical. An additional increase is attributed to a decrease in the isolation efficiency around 275 GeV [96, 123] before the fake efficiency decreases around 300 GeV due to an increase in the baseline

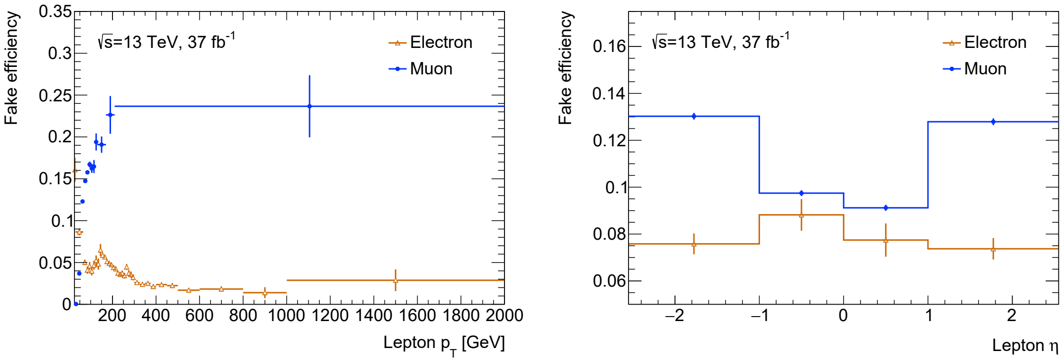

Figure 7.18: Fake electron (orange) and muon (blue) efficiencies are presented as a function of the lepton p_{T} (left) and η (right).

region resulting from the inclusion of the less restrictive HLT_e300_etcut trigger. The various used triggers, which influence the fake efficiencies due to mainly variations in the size of the baseline fake region, do not impact the final fake estimate if they are consistently treated in the baseline and signal fake regions [23].

The electron fake efficiencies as a function of η have a tendency to be slightly higher in the central region compared to the forward region. The change is caused by the varying detector instrumentation. They are symmetric in η within their statistical uncertainties and therefore only the absolute η ranges are considered. The relatively large error bars of the efficiencies are a result of the large prescale weights applied to low p_{T} electrons.

Fake Muon Efficiency

Events containing muons are selected in this analysis using $E_{\mathrm{T}}^{\mathrm{miss}}$ triggers with varying thresholds of 70-110 GeV. Removing the $p_{\mathrm{T},Z}$ requirement similar to the electron fake control region allows the selection of events with strong mismatches between the $p_{\mathrm{T},Z}$ reconstructed within the trigger system and the offline reconstructed $p_{\mathrm{T},Z}$ as the $E_{\mathrm{T}}^{\mathrm{miss}}$ triggers only consider calorimeter information where the muons typically only deposit minimal amounts of energy. This is not a feature which can be specifically attributed to fake muons and the $p_{\mathrm{T},Z}$ selection criterion is kept. In the $W \to \mu\nu+$jets region as defined in Section 7.3 no $E_{\mathrm{T}}^{\mathrm{miss}}$ cut is applied as the contribution from muon fakes is much smaller than for electrons in the corresponding $W \to e\nu+$jets region without applying the $E_{\mathrm{T}}^{\mathrm{miss}}$ selection criterion. The introduction of an inverted $E_{\mathrm{T}}^{\mathrm{miss}}$ cut to enhance the fake muon contribution is not applied as fake muons are expected to often stem from heavy flavour decays in which sizeable fractions of the jet momenta can be carried by neutrinos. Moreover, only muons with high p_{T} are able to pass the $E_{\mathrm{T}}^{\mathrm{miss}}$

trigger selection without a sizeable $E_{\mathrm{T}}^{\mathrm{miss}}$ in the event as they are invisible to the $E_{\mathrm{T}}^{\mathrm{miss}}$ triggers. To avoid such a bias only the requirement on the invariant transverse mass of the W boson, m_{T}, is removed in the fake enriched control region and the lepton p_{T} threshold is lowered to 25 GeV. Otherwise, the fake enriched region is identical to the $W \to \mu\nu +$jets control region. The $E_{\mathrm{T}}^{\mathrm{miss}}$ spectra in the fake enriched region are shown for the baseline muons (left panel) and signal muons (right panel) in the top panels of Figure 7.19. Most events attributed to fake muons have $E_{\mathrm{T}}^{\mathrm{miss}}$ values below 130 GeV. The broadened m_{T} distributions which selects additional events not related to W boson decays into muons, are presented in the middle panels. The fake contributions rise towards lower and higher m_{T} for both the baseline and the signal muons. The muon p_{T} is displayed in the lower two panels and most muon fakes have a p_{T} below 100 GeV. An increase in the number of events is seen in the muon p_{T} distributions at 55 GeV. This is related to the unprescaled HLT_mu40 (2015) and HLT_mu50 (2016) triggers used in addition to the $E_{\mathrm{T}}^{\mathrm{miss}}$ triggers which increases the efficiency of selecting events containing muons.

The muon fake efficiencies are obtained analogously to the electron ones as a function of p_{T} and $|\eta|$, but with a coarser binning as the baseline and signal muon fake enriched control regions contain lower fake contributions. They are presented in the right panel of Figure 7.17 and the respective projections are shown in Figure 7.18 for the muon p_{T} (left) and η (right). The muon fake efficiency as a function of p_{T} increases for increasing p_{T}. Most of the fake muons are expected to be of a non-prompt heavy flavour decay origin. The rejection rate of the track and calorimeter isolation requirements, with which these non-prompt muons are suppressed, drastically decreases with increasing muon p_{T} [100]. This leads to a larger fraction of muons passing the signal selection and thereby to a higher muon fake efficiency.

In the central region, the muon fake efficiency is smaller compared to the forward region. In the very central region ($|\eta| < 0.1$) no combined muons can be reconstructed due to the gap in the muon spectrometer. In particular, the remaining calorimeter or segmented muons in the baseline sample are rejected in the signal selection as only combined muons are an allowed signal muon candidate. This results in a reduced fake efficiency as non-prompt muons are expected to leave some signatures in the calorimeter and can therefore be reconstructed as calorimeter muons in the baseline selection.

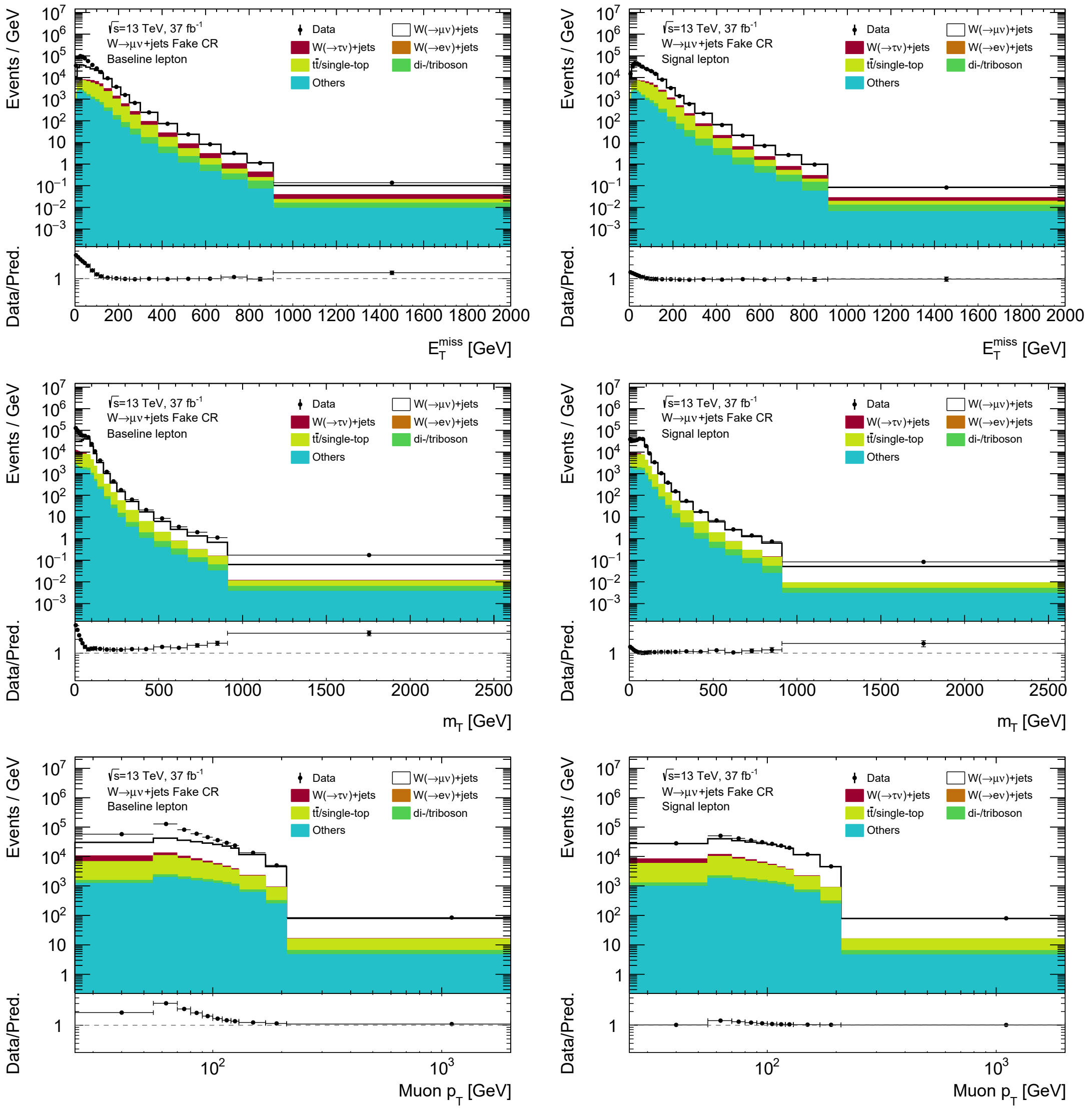

Figure 7.19: E_T^{miss} (top), m_T (middle) and the muon p_T (bottom) spectra for data and the MC simulation in the fake enriched control region with a baseline muon (left) or a signal muon (right). The lower panels show the ratios of the data to the MC simulation where deviations can be observed which are more pronounced for the baseline muons. These are attributed to fake muon contributions present in the data which are used to derive the muon fake efficiencies.

7.4.4 Systematic Uncertainties on the Fake Lepton Background Estimates

Both the real and the fake efficiencies contribute to the overall uncertainty of the background estimates obtained via the matrix method. These can be assigned to three distinct categories: statistical uncertainties due to the sample size, a potential bias of the fake efficiencies between the regions for which the fake background estimates are derived and the fake enriched control regions, and modelling uncertainties of the SM contributions in the determination of the fake efficiencies [121].

The statistical uncertainties of the real and the fake efficiencies are propagated through the assigned event weights and for the bulk of the $p_{\mathrm{T},Z}$ spectra are a minor source of uncertainty compared to the other two components.

The selection criteria on the fake enriched control regions are varied to consider potential biases due to different compositions of the various sources of fake leptons between the region in which the fake efficiencies are derived and the region for which the fake estimate is determined as each fake source can have a different fake efficiency [121]. The electron fake region is varied by restricting $E_{\mathrm{T}}^{\mathrm{miss}}$ to either values below 20 GeV or values between 20 and 50 GeV motivated by the approach in [23]. For the muon fake efficiencies, two separate regions are defined which are split into events with m_{T} below or above 10 GeV. For every variation the fake efficiencies are determined and the background estimate is repeated. The real lepton efficiencies are only mildly affected by the event topology [121] and thoroughly calibrated such that no additional uncertainty is assigned to them.

The contributions of real leptons to the fake enriched control regions are subject to several modelling and object uncertainties. The uncertainties related to the renormalisation and factorisation scale used in the MC simulation are significant and are considered in the electron and muon signal regions.

7.4.5 Fake Lepton Background Estimates

The estimated fake background contributions to both the $W \to \ell\nu$ + jets control and $Z \to \ell\ell$ + jets signal regions are summarised in Table 7.6. In addition to the number of fake lepton background events and the corresponding combined statistical and systematic uncertainties for every bin in the $p_{\mathrm{T},Z}$ spectra, the relative contributions to the predicted event yields are given. The fake lepton background contributions in all four regions are of comparable size around 1%. They are marginally smaller for the $Z \to ee$ + jets (1.0%) and $Z \to \mu\mu$ + jets (0.7%) signal regions compared to the control region with the same lepton flavour, $W \to e\nu$ + jets (1.1%) and $W \to \mu\nu$ + jets (0.9%), and tend to be smaller in the muon regions compared to electron regions. These fractions reflect to a certain degree the relative fractions at low $p_{\mathrm{T},Z}$ as these have the highest event yields due to the exponentially falling $p_{\mathrm{T},Z}$ spectra. The contribution of the fake lepton background estimate rises for increasing $p_{\mathrm{T},Z}$ for the $W \to e\nu$ + jets channel, reaching up to 6.6%

$p_{\mathrm{T},Z}$ [GeV]	$Z \to ee + \text{jets}$		$Z \to \mu\mu + \text{jets}$		$W \to e\nu + \text{jets}$		$W \to \mu\nu + \text{jets}$	
	Est.	Frac.[%]	Est.	Frac.[%]	Est.	Frac.[%]	Est.	Frac.[%]
130-170	504±186	1.1	431±138	0.7	1982 ±1027	0.9	4411 ±594	1.1
170-210	275±136	1.1	283±115	0.8	1451±564	1.1	1745±236	0.8
210-250	157±80	1.3	147±67	0.8	698±276	1.0	672±122	0.6
250-300	69±63	1.0	95±67	0.9	464±181	1.1	324±59	0.5
300-380	58±37	1.3	49±30	0.8	400±112	1.6	170±31	0.5
380-470	20±13	1.2	22±14	0.9	247±68	2.5	59±11	0.5
470-570	7.2±4.4	1.1	6.2±4.0	0.7	106±30	2.9	22±5	0.5
570-670	2.7±2.0	1.2	0.9±1.0	0.3	48±13	3.6	7.1±1.8	0.5
670-790	0.4±0.4	0.4	3.5±2.9	2.7	28±3	4.7	4.8±1.6	0.7
790-910	0.3±0.3	0.7	0.3±0.4	0.8	14±3	5.7	0.9±0.6	0.4
910-2600	0.4±0.3	1.4	0.0±0.0	0.0	12±6	6.6	1.0±0.5	0.6
Combined	1092.7±522.0	1.0	1037.7±439.6	0.7	5448.8±2283.5	1.1	7417.0±1061.8	0.9

Table 7.6: Fake lepton background estimates in the $Z \to ee + \text{jets}$ & $Z \to \mu\mu + \text{jets}$ signal regions and the $W \to e\nu + \text{jets}$ & $W \to \mu\nu + \text{jets}$ control regions with the corresponding total uncertainties. In addition, the relative contributions of those backgrounds in the respective signal or control regions are stated.

in the tail of the $p_{\mathrm{T},Z}$ distribution, in contrast to the other fake lepton background estimates. This rise is in parts related to the isolation which is more inclusive for electrons with high p_{T}. In the $Z \to ee + \text{jets}$ signal region, this is not such a pronounced feature due to the different event topology and the energy dependence of the isolation.

The $W \to e\nu + \text{jets}$ fake electron background estimate is validated by deriving an alternative estimate using a data-driven template fit approach. Templates of the shape of the fake background are derived both for $p_{\mathrm{T},Z}$ and $E_{\mathrm{T}}^{\mathrm{miss}}$. They are obtained by inverting the identification requirement and removing the track-to-vertex association criterion from the $W \to e\nu + \text{jets}$ control region. Events in the data in this region which are not described by the respective MC simulation are attributed to the fake background and form the two templates. Both templates are normalised by fitting the $E_{\mathrm{T}}^{\mathrm{miss}}$ template in the $W \to e\nu + \text{jets}$ control region together with the SM processes which are allowed to float but are constrained by considering their theory uncertainties to the data. The $E_{\mathrm{T}}^{\mathrm{miss}}$ observable is used to derive the normalisation as it has a distinct shape compared to the SM processes as seen in Figure 7.16. The obtained relative fraction of the fake contribution of $1.6 \pm 1.2\%$ is consistent within uncertainties with the result from the matrix method. In addition, the background estimates obtained via the matrix method and the template fit approach are checked in a validation region which is enriched in electron fakes. The validation region is obtained by removing the m_{T} and $E_{\mathrm{T}}^{\mathrm{miss}}$ selection criteria from the $W \to e\nu + \text{jets}$ control region which enhances the fake background contribution by roughly one order of magnitude. Both estimates improve the description of the data at low $p_{\mathrm{T},Z}$, but the template fit significantly overestimates the electron fake contribution at high $p_{\mathrm{T},Z}$. As the relative contributions of both estimates are in agreement which each other the matrix method is used as the nominal background estimation technique and no additional uncertainty is assigned.

The sizeable relative uncertainties on the fake background estimates are besides the low statistics in the tails of the $p_{\mathrm{T},Z}$ distributions, a result of the substantial uncertainties on the fake lepton efficiencies. Together with their overall size, they required several adoptions in the definition of the signal and control regions to ensure that the uncertainty on the final result is not driven by this fake background component. To reduce the number of fake electrons in the $W \to e\nu + \mathrm{jets}$ region, the additional $E_{\mathrm{T}}^{\mathrm{miss}}$ requirement is introduced in addition to the criterion on the transverse W mass which is also applied in the $W \to \mu\nu + \mathrm{jets}$ region. The sub-leading lepton p_{T} requirement is set to 25 GeV to reduce the number of events related to low-p_{T} lepton fakes in the $Z \to \ell\ell + \mathrm{jets}$ signal regions. With the overall rather small size of the fake lepton background after the phase space adoptions mentioned above the corresponding uncertainties on the fake lepton backgrounds are of sub-leading order to the overall uncertainty on $\Gamma_Z(\mathrm{inv})$.

8 Uncertainties

The $p_{\mathrm{T},Z}$ spectra and the R^{miss} ratios, both on the presented detector level and later on the particle level, underlie several sources of systematic uncertainties. These can be grouped into experimental and theoretical modelling uncertainties alongside the statistical uncertainties in the data and in the MC simulation event yields. The statistical uncertainties are obtained by the square roots of the respective event yields as the binning is optimised to contain at least 20 events in each bin. They are considered to be uncorrelated between bins and regions. The experimental uncertainties are mainly related to the reconstruction, identification, isolation and trigger efficiencies of the reconstructed objects and their respective energy and momentum scales. In addition, event related quantities carry uncertainties such as the pile-up profile. These uncertainty sources are often studied in depth in dedicated measurements providing $1\,\sigma$ variations of the respective central values typically used to scale the MC simulations to the data. These uncertainty sources are split into uncorrelated components and are associated with sets of parameters which are varied to account for the respective sources. The uncertainties are propagated onto the results by repeating the entire measurement with the varied input parameters considering the estimated $1\,\sigma$ variation of the impact of the respective uncertainty source on the parameters. The comparison to the nominal result allows the derivation of the relative size of the uncertainty. They are applied to both the $Z \to \nu\nu + \mathrm{jets}$ and $Z \to \ell\ell + \mathrm{jets}$ signal regions of the R^{miss} ratios over the entire $p_{\mathrm{T},Z}$ spectra thereby accounting for bin-by-bin correlations as well as correlations between the numerator and the denominator. The various presented sources of systematic uncertainties are assumed to be uncorrelated and are hence added in quadrature to obtain the combined total uncertainty.

The sources of systematic uncertainties which have an impact on the measured invisible width are presented in this section and are separated into experimental and theoretical uncertainties.

8.1 Experimental Uncertainties

The various sources of experimental uncertainties related to particle objects or event quantities are derived by the ATLAS performance groups and are propagated through the analysis as presented in this section. Uncertainties on the background estimation methods used in Section 7 are described therein and are only summarised here.

8.1.1 Jet Uncertainties

The largest jet uncertainties are related to the jet energy and resolution scales which in parts need some specific treatments and are discussed in depth in the following. In addition, the uncertainties related to the efficiency of the (f)JVT jet selections removing pile-up jets are considered which are determined by analysing the $Z \to \mu\mu+$jets process [93, 94].

Jet Energy Scale Uncertainties

The various calibration steps contribute uncertainties to the jet energy scale (JES). These include four sources of systematic uncertainties arising through the jet pile-up correction [88]. The jet flavour composition uncertainty describes the uncertainty on the fraction of jets initiated by gluons which have a different response than quark-initiated jets, whereas the flavour response uncertainty covers the response difference of gluon-initiated jets between the Pythia and Herwig generators [124, 125]. The nominal flavour response uncertainty is the dominating source for the jet energy scale uncertainty in a wide range of considered jet p_{T}. Phase space specific flavour composition maps were derived in [22] which are applied to the $\Gamma_Z(\mathrm{inv})$ measurement after validating their consistency with the $\Gamma_Z(\mathrm{inv})$ phase spaces. The conservative, default quark and gluon jet fractions of 0.5 ± 0.5 are hence replaced by custom compositions. These have uncertainties between $5-15\%$ which are derived from differences in the considered phase spaces as well as the deviations to the fractions obtained from alternative MG5_aMC+Py8 predictions. This reduces the size of the conservative, nominal flavour uncertainty.

Energetic jets which are not fully contained within the calorimeters, but leak into the muon spectrometer, are assigned a punch-through uncertainty depending on their depositions in the muon detectors [125]. The η-intercalibration contributes with five uncertainties whereas the uncertainties from the other in-situ calibration steps stem from the event topology, analysis selections, the calibration of the reference objects, MC simulation modelling or from a statistical origin. These lead to a total of 125 jet energy scale uncertainty components. From the in-situ uncertainties, 98 only depend on p_{T} allowing a combination to a total of 15 parameters which still obtain a large degree of correlation information. This is achieved by performing an eigenvector decomposition of the corresponding covariance matrix [124]. This setting used in the analysis is called the 'category reduction' leading to a total of 28 uncertainties. The last component is the high-p_{T} single particle uncertainty for jets exceeding the 2.4 TeV threshold of the multijet in-situ analysis [126].

Jet Energy Resolution Uncertainties

The jet energy resolution (JER) uncertainties are derived using a similar reduction scheme in which 13 eigenvectors are determined from the three uncertainty sources (Equation 5.3) via pile-up and electrical noise analyses as well as from a dijet balance study [88]. For small jet momenta, the main contribution arises from propagating the JES uncertainties to the dijet measurement. The high p_{T} jet resolution is limited by a non-closure uncertainty which covers the difference between in-situ resolution measurements in MC simulation and the resolution derived directly from the particle level jet transverse momenta. Sources with smaller impacts are variations of the analysis cuts and the difference to another MC generator. An additional non-closure uncertainty stems from a random cone noise analysis either due to fluctuations in the topo-cluster formation or differences in the electronic noise depending on the number of particles from the hard-scatter interaction. The calibration factor of the noise to the appropriate scale and the variation of analysis cuts provide additional pile-up related contributions. Sources of the electrical noise uncertainty stem from an estimated uncertainty covering differences between data and simulation and from the fit performed to extract the electronic noise.

The uncertainties are propagated by introducing additional smearing to the nominal JER smearing, σ_{nom}, by considering the one sigma variation of the uncertainty σ_{unc}. The jets are hence smeared with a Gaussian of width

$$\sigma_{\mathrm{smear}} = \sqrt{(\sigma_{\mathrm{nom}} + |\sigma_{\mathrm{unc}}|)^2 - \sigma_{\mathrm{nom}}^2}. \tag{8.1}$$

To conserve the anti-correlations of crossing zero uncertainties the smearing is applied to the MC simulation if the σ_{unc} is positive and otherwise to the data. In the case where the precision of the resolution in data exceeds the one in the MC simulation an additional uncertainty is considered covering the difference between the two resolutions.

A Bootstrap smoothing method [127] is applied to the relative JER uncertainties because the single sampling for every jet from the Gaussian with a certain width to assign the extra smearing leads to the addition of spurious statistical uncertainties. The Bootstrap method allows quantifying the statistical uncertainty on the systematic JER variations which can give unreasonable shapes in the tails of the $p_{\mathrm{T},Z}$ spectra. The JER uncertainties are hence first rebinned until either the relative statistical error on the systematic uncertainty is smaller than 30% or they deviate by more than $2\,\sigma$ from the nominal distribution indicating their statistical significance. The rebinning is performed by combining bins with either their right, left or both neighbouring bins until they are fulfilling at least one of the two conditions. The procedure with the most remaining bins is chosen. The so-obtained uncertainties are then assigned to the corresponding bins of the original binning. A Gaussian kernel smoothing completes this procedure.

8.1.2 Charged Lepton Uncertainties

Electron uncertainties mainly stem from uncertainties on the efficiency scale factors. These are split into 117 components. The main contributions to the uncertainties of those scale factors are potential biases in the tag-and-probe methods used to determine the efficiencies and in the estimation of subtracted background processes [97]. Electron energy scale and resolution uncertainties are derived by studying $Z \to ee$ and $J/\Psi \to ee$ decays [98].

Muon uncertainties are dominated by uncertainties related to the efficiency scale factors which originate from potential biases in the tag-and-probe method used to determine the efficiencies, the estimation of the non-prompt muon backgrounds, the isolation criteria and the invariant mass range of the two muons. These are combined into eight components related to reconstruction, isolation and track-to-vertex-association efficiencies. Muon momentum scale and resolution uncertainties are studied in $Z \to \mu\mu$ and $J/\Psi \to \mu\mu$ resonance decays [101, 102]. These uncertainties are split into two components related to tracks reconstructed in the inner detector and in the muon spectrometer. The individual components are presented in [102]. An additional correction to the muon momenta measured in data is necessary due to the misalignment of detector components. The corresponding dominant uncertainty is derived by studying the non-closure when a measured bias is introduced on the muon momenta in the MC simulations which are compared to the data [102].

The tau energy scale uncertainty is determined from in-situ measurements of the $Z \to \tau_\mu \tau_{\mathrm{had}}$ decay and is dominated by background modelling, tau energy resolution and muon reconstruction uncertainties from the in-situ energy scale measurements [104].

8.1.3 Missing Transverse Momentum Uncertainties

All uncertainties from the hard constituents are propagated through the $E_{\mathrm{T}}^{\mathrm{miss}}$ calculation and two additional uncertainties for the soft term are considered. The uncertainties of the soft term are split into a scale and a resolution component which in turn are again separated in a contribution parallel and perpendicular to the hadronic recoil system. They are derived from observed differences in data and the MC simulation for processes which lack intrinsic $E_{\mathrm{T}}^{\mathrm{miss}}$ [107].

8.1.4 Other Uncertainty Sources

The MC simulations are reweighted to match the pile-up profile in the data and a corresponding uncertainty covering remaining differences is considered [67]. The integrated luminosity is measured with a precision of 0.87% [109] by the LUCID-2 detector [110] used for the primary luminosity measurement. This uncertainty cancels to a large degree in the R^{miss} ratio as only the subtracted, unconstrained background estimates have a residual dependence on the luminosity uncertainty.

Uncertainties of the data-driven background estimates are already discussed in the respective sections and are only summarised shortly here before the uncertainties related to the final extraction of the $\Gamma_Z(\mathrm{inv})$ measurement are presented which are mainly related to the methods used to bring the $Z \to \nu\nu + \mathrm{jets}$ and $Z \to \ell\ell + \mathrm{jets}$ event yields into the same phase space.

Data-driven Background Estimation Method Uncertainties

Both the QCD multijet and the non-collision background estimates are assigned a conservative uncertainty of 100% following [119]. The aforementioned uncertainties and theory uncertainties are propagated through both $W \to \ell\nu + \mathrm{jets}$ control regions onto the scale factors used for normalising the $W \to \ell\nu + \mathrm{jets}$ contributions in the $Z \to \nu\nu + \mathrm{jets}$ signal region. In addition, the derivation of the scale factors is repeated with a varied control region in which the m_T cut is changed to capture potential biases related to the definitions of the two control regions. Similar phase space variations are applied to the fake-enriched control regions used to derive the fake efficiencies for the lepton fake estimates. In these fake-enriched control regions only the factorisation and renormalisation uncertainties are significant and hence considered in the subtraction of the real contributions to determine the electron and muon fake efficiencies.

Γ_Z(inv) Extraction Uncertainties

The uncertainties mentioned above combined with the theory uncertainties presented in Section 8.2 are sufficient to derive the uncertainties on the measured R^{miss} ratios within the defined signal region's phase spaces obtained from reconstructed particles. The extraction of $\Gamma_Z(\text{inv})$ relies on detector corrections transferring the ratios from detector to particle level. This is done with a bin-by-bin detector correction presented in Chapter 10. This bin-by-bin correction of the R^{miss} ratio is compared to an iterative Bayesian unfolding procedure [128] where each individual $Z \to \nu\nu + \text{jets}$ or $Z \to \ell\ell + \text{jets}$ spectrum is unfolded before R^{miss} is constructed. The difference between the bin-by-bin correction and the R^{miss} ratio constructed from the spectra corrected with two iterations of Bayesian unfolding is taken as uncertainty to cover potential residual biases in the detector correction factors.

The so obtained R^{miss} ratio at particle level contains contributions from off-shell photons which interfere with the Z boson in the production of charged lepton pairs and the invariant mass of the Z boson is constrained to values close to the Z boson mass to avoid sizeable contributions from the photon production channel. The charged leptons correspond to dressed-leptons after the detector correction as photons within a cone of $\Delta R < 0.1$ are added to the final state lepton in the used MC simulations. The neutrinos do not radiate any photons and hence the leptons are corrected to Born level before any final state radiation. Correction factors are derived in MC simulations as a function of $p_{\text{T},Z}$ to correct for these effects and the corresponding statistical as well as factorisation and renormalisation scale uncertainties are considered as an additional source of systematic uncertainty on R^{miss}.

The translation from a measured R^{miss} value to the invisible width relies on the multiplication with the measured $\Gamma_Z(\ell\ell)$ as shown in Equation 2.7. The uncertainty on $\Gamma_Z(\ell\ell)$ is taken from their combination assuming lepton universality [6].

8.2 Theory Uncertainties

The theory uncertainties can be separated into three main categories which partially traces back to the factorisation of the calculation of the cross section in perturbation theory as presented in Equation 4.1. The first component is related to the fixed order calculation of the hard-scattering process in which the perturbative expansion of the partonic cross section is stopped at some fixed order and the higher order terms are neglected. This leads to an uncertainty on the cross section whose effects are studied by varying the renormalisation (μ_R) and factorisation (μ_F) scale up and down by a factor of two. The uncertainty is obtained from the envelope of a seven-point pairwise variation of the two scales with the constraint that no off-diagonal variations are allowed, where one scale is varied up and the other down, to avoid large logarithms [129]. This QCD scale uncertainty is typically the dominant theoretical uncertainty for all processes.

The parton distribution functions (PDFs) are affected by experimental uncertainties stemming from the underlying measurements and uncertainties related to the functional form of the fits used in the determination of the various PDF sets. The PDF4LHC15_nnlo PDF set [130] and the NNPDF3.0nnlo PDF set [77] are used to derive a corresponding uncertainty. The PDF4LHC15_nnlo uncertainties are given as a symmetric Hessian PDF set with n (30) eigenvectors which are combined to a single uncertainty parameter [130]

$$\delta^{\mathrm{PDF}}\sigma = \sqrt{\sum_{k=1}^{n} \left(\sigma^{(k)} - \sigma^{(0)}\right)^2} \ , \tag{8.2}$$

with the nominal PDF of this set $\sigma^{(0)}$. For some MC processes, PDF MC sets are provided instead of eigenvector sets. For those $\delta^{\mathrm{PDF}}\sigma$ is determined by taking the average of all MC replicas as $\sigma^{(0)}$ and dividing the sum of the standard deviations by $n-1$.

The strong coupling constant α_s is determined from measurements and its value of 0.118 is given at the scale of the Z boson mass. The translation to another scale introduces additional uncertainties as the used renormalisation group is truncated at a fixed order. The respective uncertainty is obtained by using the same PDF set but evaluated at two different values of α_s [130]:

$$\delta^{\alpha_s}\sigma = \frac{\sigma(\alpha_s^{\mathrm{up}}) - \sigma(\alpha_s^{\mathrm{down}})}{2} \ . \tag{8.3}$$

For the NNPDF3.0nnlo (PDF4LHC15_nnlo) PDF set these values are 0.119 (0.1195) and 0.117 (0.1165). The PDF and α_s are typically added in quadrature and referred to as $\delta^{\mathrm{PDF}+\alpha_s}$.

One additional uncertainty is added for the subtracted top backgrounds. The interference and overlap between $t\bar{t}$ and tW top production is removed by the diagram-removal scheme [131]. An alternative diagram-subtraction scheme [131, 132] is evaluated and the difference between these two approaches is assigned as an uncertainty.

8.3 Relative Sizes of the Uncertainty Components

In Figure 8.1 the symmetrized relative uncertainties are shown for the $Z \rightarrow \nu\nu +$jets signal region and in Figure 8.2 for the $Z \rightarrow ee +$jets (up) and $Z \rightarrow \mu\mu +$jets (down) signal regions on detector level if they exceed 0.5% in any bin. The $Z \rightarrow \nu\nu +$jets signal region at low $p_{\mathrm{T},Z}$ is dominated by the uncertainties of the QCD multijet and by the jet energy scale. The latter is also the leading uncertainty source of the $Z \rightarrow \ell\ell +$jets signal regions at low $p_{\mathrm{T},Z}$. Another sizeable component is the QCD scale uncertainty of the subtracted MC simulations where the top related processes contribute the most. They are denoted as residual theory uncertainty. The lepton efficiency uncertainties range for both $Z \rightarrow \ell\ell +$jets signal regions from around 1% at low $p_{\mathrm{T},Z}$ to 4-6% at high $p_{\mathrm{T},Z}$ and are slightly smaller for muons compared to electrons. Overall they are among the leading uncertainty contributions in the R^{miss} ratio as they do not cancel during the construction of the ratio in contrast to uncertainties which contribute to the numerator and the denominator such as uncertainties related to jets. The sizes of the relative uncertainties in the two $Z \rightarrow \ell\ell +$jets signal region are comparable to each other. The statistical uncertainties at low $p_{\mathrm{T},Z}$ are slightly smaller in the muon channel. In the tails of the two lepton signal regions, the statistical uncertainties become comparable again as the muon and electron reconstruction and identification efficiencies approach each other. The statistical uncertainty becomes the largest uncertainty at high $p_{\mathrm{T},Z}$ at 670 GeV for

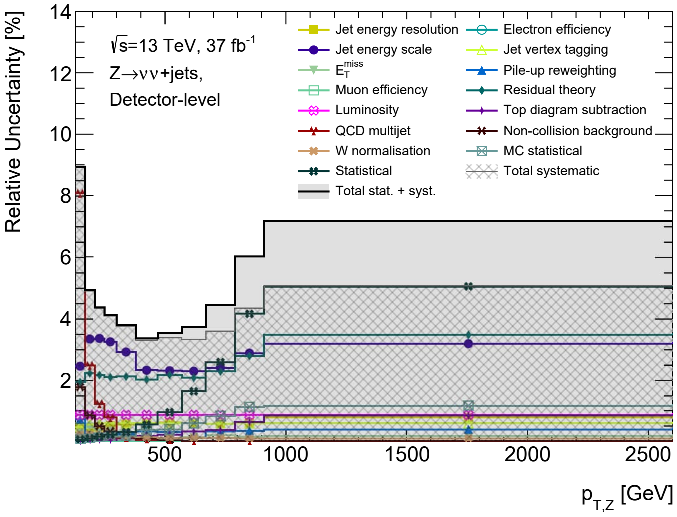

Figure 8.1: Relative uncertainties in the $Z \rightarrow \nu\nu +$jets signal region. Only systematic uncertainties with a contribution of at least 0.5% in any bin are presented. The shown uncertainties are symmetrized.

$Z \to \nu\nu +$jets and at 500 GeV for the $Z \to \ell\ell +$jets signal regions. In the $Z \to \nu\nu +$jets signal region the total uncertainty ranges from 9% at low $p_{\mathrm{T},Z}$ to a minimum of about 3.5% around 400 GeV and rises to 7% in the tail. The uncertainties for the $Z \to \ell\ell +$jets regions rise from 3% (2.5%) for electrons (muons) up to 18% at high $p_{\mathrm{T},Z}$.

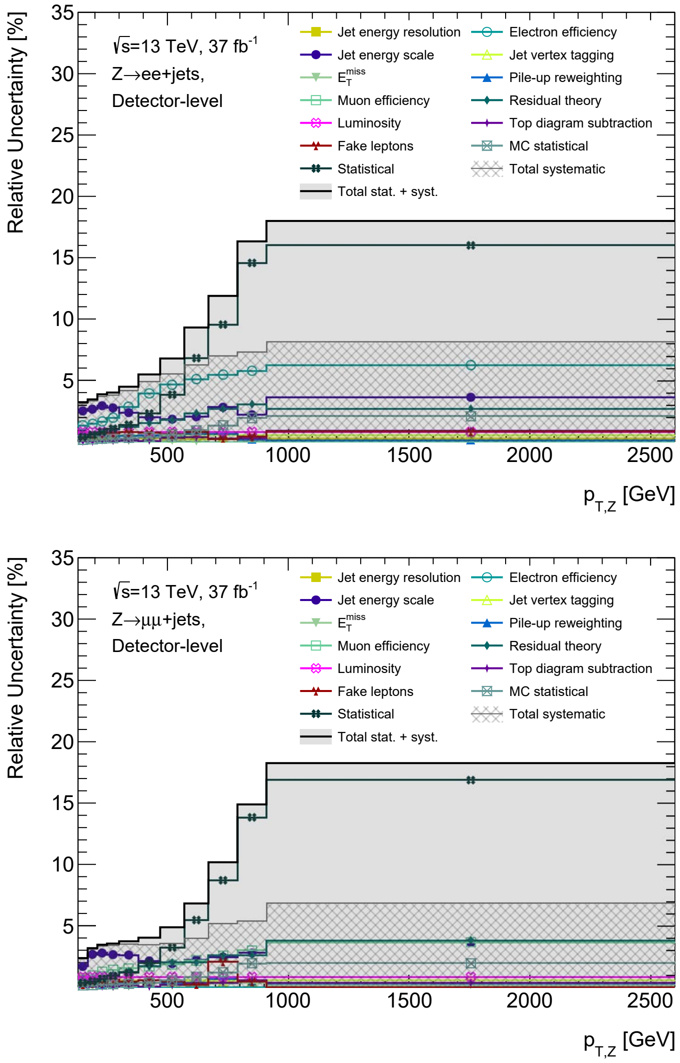

Figure 8.2: Relative uncertainties in the $Z \to ee +$jets (top) and $Z \to \mu\mu +$jets (bottom) signal region. Only systematic uncertainties with a contribution of at least 0.5% in any bin are presented. The shown uncertainties are symmetrized.

9 Detector Level Results

The proper modelling of the structures observed in the measured data by the detector level signal MC simulations and the background processes in the $Z \rightarrow \nu\nu+$jets and $Z \rightarrow \ell\ell+$jets signal regions are validated in this chapter. These backgrounds are either directly taken from the detector level MC simulations or obtained via the data-driven methods presented in Chapter 7. A proper description of the data by the MC simulation is important for a valid subtraction of the background events from the data in the three signal regions to construct the R^{miss} ratios.

The measured event yields in the $Z \rightarrow \nu\nu+$jets and in both $Z \rightarrow \ell\ell+$jets signal regions are hence compared to the SM MC simulation at the detector level including the data-driven background estimates derived in Chapter 7. Figure 9.1 shows this comparison for the measured $p_{\text{T},Z}$[1] distribution in the $Z \rightarrow \nu\nu+$jets signal region. The $W \rightarrow \ell\nu+$jets contributions are normalised according to the procedure introduced in Section 7.3. The non-collision and the QCD multijet backgrounds are both derived with data-driven methods and contribute only at small values of $p_{\text{T},Z}$. The remaining SM contributions are obtained from MC simulations and are scaled to $37\,\text{fb}^{-1}$ to match the integrated luminosity of the data. Z boson decays into charged leptons and electroweak vector boson production in association with a jet are summarised as 'Others'. The contributions from $W \rightarrow \ell\nu+$jets events and processes involving semi-leptonic top decays decrease with increasing $p_{\text{T},Z}$ as the leptons tend to have higher momenta. Leptons with larger p_{T} also tend to be more central which leads to an increased reconstruction efficiency as the identification efficiency is higher in the central region [96]. The $Z \rightarrow \nu\nu+$jets signal contribution rises from about 42% at low $p_{\text{T},Z}$ to 71% at high $p_{\text{T},Z}$. An increase is also observed for the di-/triboson processes and the electroweak V+jet production including Z boson decays into neutrinos due to the typically larger jet transverse momenta [133] recoiling against the Z boson.

The black error bars on the data show the statistical uncertainty whereas the blue-hashed band represents the combined statistical and systematic uncertainty. The latter includes experimental uncertainties driven by the jet energy scale, uncertainties related to the QCD multijet, the non-collision background and the $W \rightarrow \ell\nu+$jets normalisation

---

[1] The definition of $p_{\text{T},Z}$ is given in Equation 6.1.

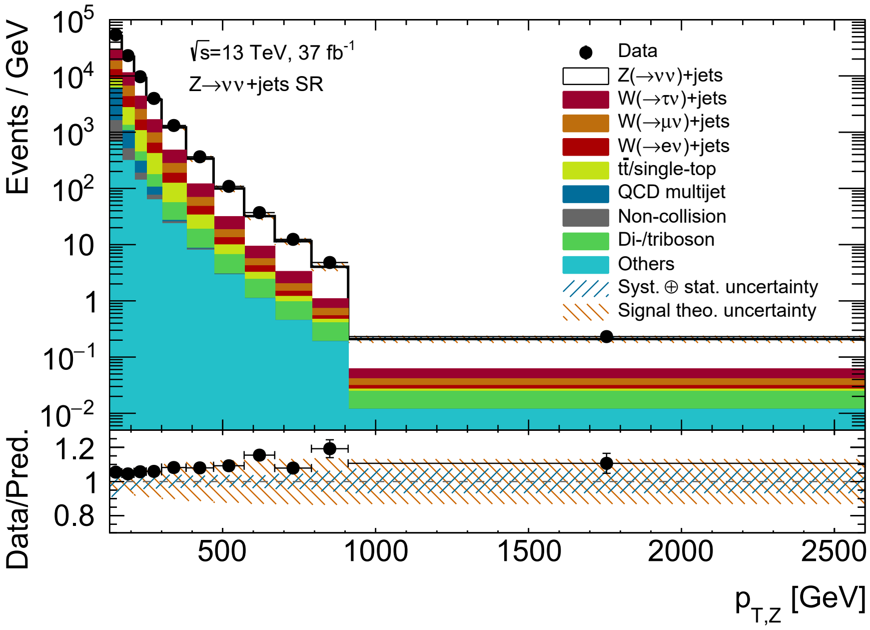

Figure 9.1: The $p_{\mathrm{T},Z}$ spectra are displayed for both the data and the MC simulation (including the data-driven backgrounds) in the $Z \to \nu\nu+$jets signal region. The error bars on the data represent the statistical uncertainties, while the blue-hashed band depicts the combined statistical and systematic uncertainties. The theory uncertainty on the signal process, presented in white, is shown as the orange-hashed band. The lower panel illustrates the agreement between the data and the MC simulation, which mainly falls within the corresponding uncertainty bands with some outliers in the high-p_{T} tail.

scale factors, as well as residual theory uncertainties from the subtracted backgrounds, compare Section 8.3. They range from 9% in the lowest $p_{\mathrm{T},Z}$ bin, dominated by the QCD multijet uncertainty, to a minimum of 3.5% around 400 GeV, reaching 8% in the tail of the distribution which is dominated by the statistical uncertainty. The lower panel illustrates the agreement between the data and the MC simulation considering the various background estimates. It can be seen that the shape of the MC simulation resembles the data, but they have a negative normalisation offset of about 5% compared to the data. This indicates that the normalisation of the modelled $Z \to \nu\nu+$jets signal process is too small as the main backgrounds are normalised to the data via the dedicated control regions. Two upwards fluctuations above the otherwise flat ratio of the data over the MC simulation are observed around 600 (900) GeV of 10 (15)%. These outliers are within the 1-2 σ interval considering the theoretical uncertainties related to the dominating renormalisation and factorisation scale on the $Z \to \nu\nu+$jets signal process which are shown by the orange-hashed band.

The $p_{\mathrm{T},Z}$ spectra of the $Z \rightarrow ee+$jets (top) and $Z \rightarrow \mu\mu+$jets (bottom) are shown analogously in Figure 9.2. The overall signal event yield in these regions is more than an order of magnitude smaller compared to $Z \rightarrow \nu\nu+$jets. A factor of about six is expected as in the Z boson decay into a pair of neutrinos all neutrino families are combined and overall their branching fractions are higher as they do not have a contribution from the electric charge (Equation 2.7). The remaining difference results from the inefficiencies of reconstructing the charged leptons. The larger event yields in the muon channel, in particular at small $p_{\mathrm{T},Z}$, are a consequence of the higher reconstruction efficiency of muons compared to electrons [96, 100]. Overall the 2-lepton signal regions are quite pure having a signal contribution of about 95% due to the strict selection requirements placed on the charged lepton pairs. In both regions, the Z boson decay into a pair of charged electrons or muons decreases slightly for increasing $p_{\mathrm{T},Z}$ to about 85% at the high $p_{\mathrm{T},Z}$ tail as the contributions from di-/triboson processes as well as from electroweak V+jet production increase.

The shape of the data is again well described by the MC simulation including the data-driven fake lepton background aside from some fluctuations in the tails of the distributions. The data exceed the MC simulation in both the electron (8%) and the muon (6%) channel similar to the $Z \rightarrow \nu\nu+$jets signal region. In the $Z \rightarrow ee+$jets signal regions the last two bins of the ratio fluctuate upwards and the bin around 600 GeV fluctuates downwards. In the $Z \rightarrow \mu\mu+$jets signal region the bin at 600 GeV shows a small upwards fluctuation similar to the $Z \rightarrow \nu\nu+$jets signal region as well as in the second to last bin. Nevertheless, the agreement between the data and the MC simulation in both $Z \rightarrow \ell\ell+$jets signal regions is for every bin well within 1-2 σ with respect to the corresponding uncertainties, in particular, if the theory uncertainties on the signal processes are considered. The largest experimental uncertainties stem from the jet energy scale and the electron or muon efficiencies. The statistical uncertainty becomes the dominant source for $p_{\mathrm{T},Z}$ above 500 GeV.

These three signal regions allow the construction of the R^{miss} ratios. The SM background predictions from MC simulations and the obtained background estimates from Chapter 7 are subtracted from the $Z \rightarrow \nu\nu+$jets signal region thereby constructing the numerator of the ratio as well as from the $Z \rightarrow ee+$jets and $Z \rightarrow \mu\mu+$jets which form the denominators of the two respective ratios. The R^{miss}_{ee} and $R^{\mathrm{miss}}_{\mu\mu}$ are then obtained by a bin-by-bin division of the $p_{\mathrm{T},Z}$ distribution of the respective numbers of signal events in both the numerator and the denominator. Figure 9.3 compares these measured ratios to the ratios obtained from MC simulations of $Z \rightarrow \nu\nu+$jets to $Z \rightarrow ee+$jets (top) and $Z \rightarrow \nu\nu+$jets to $Z \rightarrow \mu\mu+$jets (bottom). A good agreement between the data

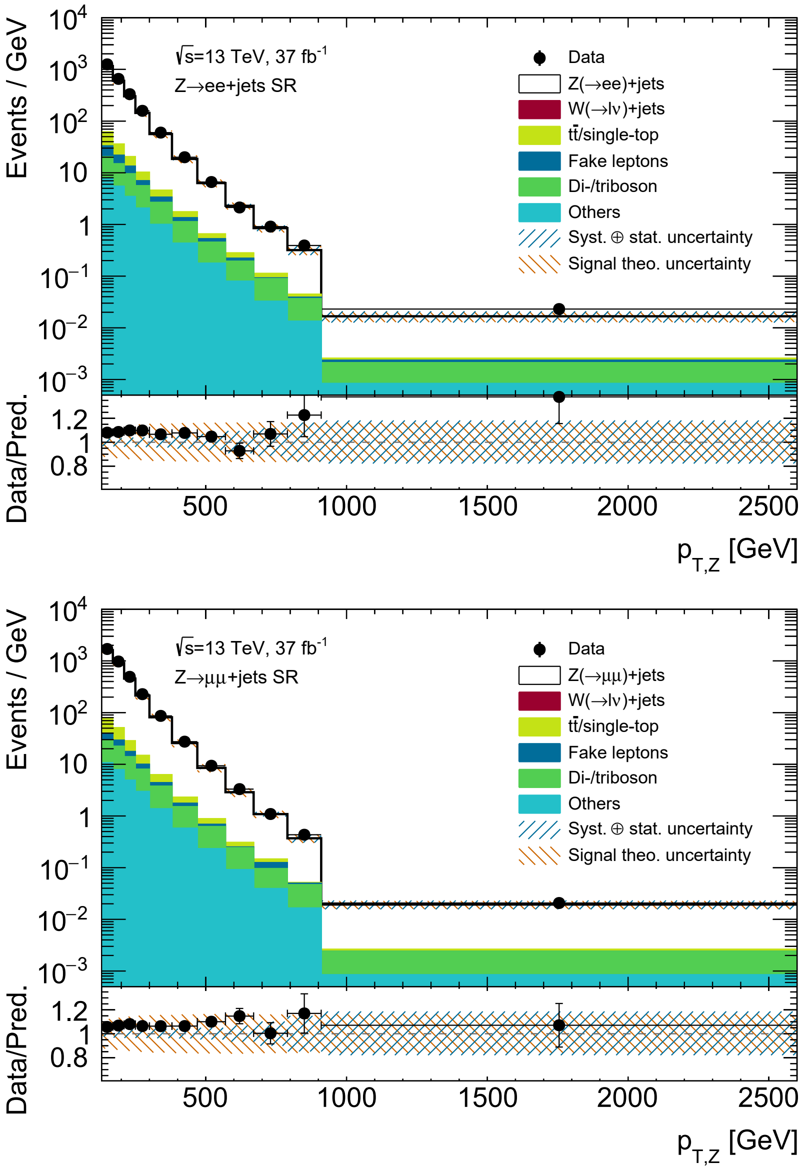

Figure 9.2: The $p_{\mathrm{T},Z}$ spectra are displayed for both the data and the MC simulation (including the fake lepton backgrounds) in the $Z \to ee +$ jets (left) and $Z \to \mu\mu +$ jets (right) signal regions. The error bars on the data represent the statistical uncertainties, while the blue-hashed bands depict the combined statistical and systematic uncertainties. The theory uncertainties on the signal process, presented in white, are shown as the orange-hashed band. The lower panel illustrates the agreement between the data and the MC simulation.

and the MC simulations is observed which improves compared to the agreement in the individual channels. This can be understood as the normalisation mis-modelling in the Z boson production cancels to a large extent in the construction of the ratios.

One outstanding deviation is however observed between the data and the MC simulations in the R_{ee}^{miss} ratio at 570-670 GeV which is a combination of the aforementioned upwards fluctuation of the ratio between data and the MC simulation in the $Z \rightarrow \nu\nu+\mathrm{jets}$ signal region paired with a corresponding downwards fluctuation in the $Z \rightarrow ee+\mathrm{jets}$ signal region. They have already been observed in previous measurements covering similar phase spaces [134] and are less pronounced in the full Run 2 dataset [119]. The dominant uncertainties on the two ratios are the lepton efficiencies, theory uncertainties related to the renormalisation and factorisation scale and at low $p_{\mathrm{T},Z}$ the uncertainty of the QCD multijet background. Above 500 GeV the statistical uncertainty becomes the dominant source of uncertainty. The jet energy scale uncertainty which plays an important role in the individual measurements cancels to a large extent which shows the strength of a ratio measurement which reduces correlated uncertainty sources. The combined uncertainty which adds the individual components in quadrature ranges from 3% up to 18% in both ratios.

Even if the R_{ee}^{miss} and $R_{\mu\mu}^{\mathrm{miss}}$ ratios show good agreement with the detector level MC simulation obtained from both Sherpa 2.2.11 and MG5_aMC+Py8, they are in clear contrast to the SM prediction for these ratios (Equation 2.6), which expects them to be constant as a function $p_{\mathrm{T},Z}$ and close to 5.97. R_{ee}^{miss} however ranges from values around 20 to 10 from low to high $p_{\mathrm{T},Z}$ and $R_{\mu\mu}^{\mathrm{miss}}$ ranges from around 15 to 9. This is a result of the more restrictive phase space selections which need to be placed on the charged leptons compared to the neutrinos, and the inefficiency of reconstructing the charged leptons. The R^{miss} ratios, therefore, need to be corrected for detector effects and be extrapolated to a common phase space which is presented in the next chapter.

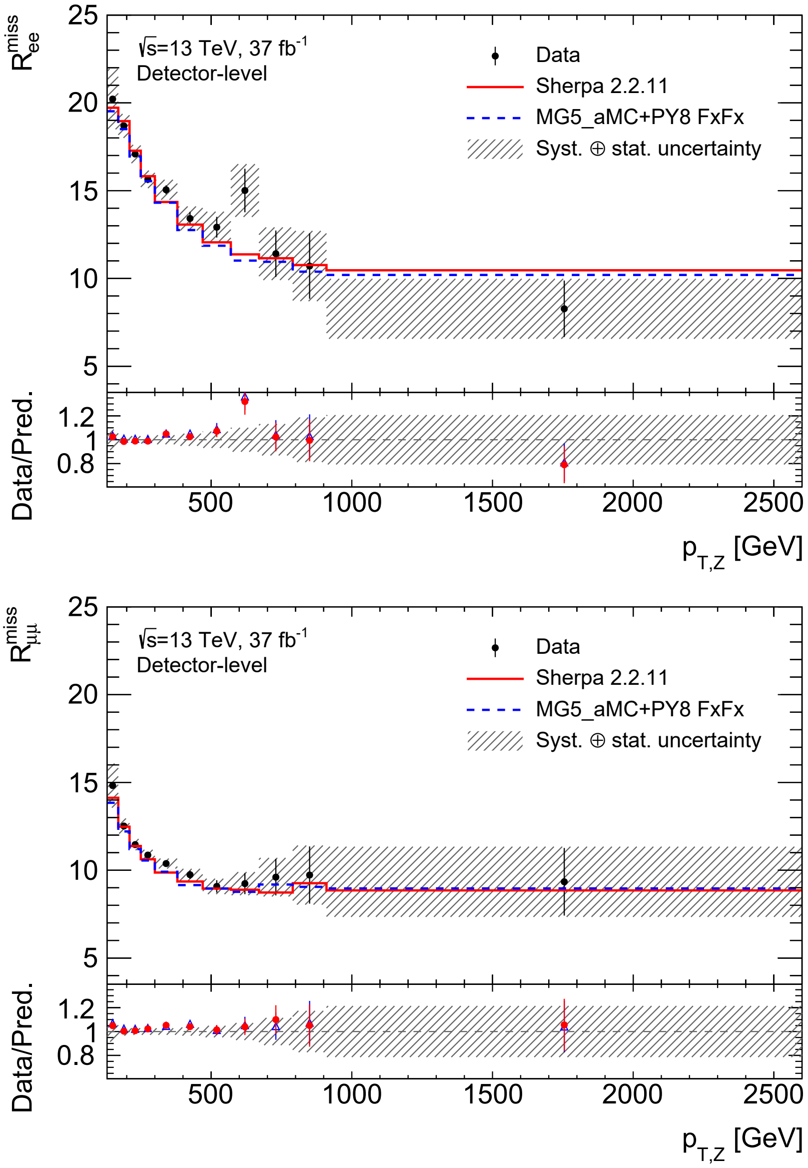

Figure 9.3: Comparison of the R^{miss}_{ee} (top) and $R^{\text{miss}}_{\mu\mu}$ (bottom) ratios obtained from the background-subtracted data with the detector level MC simulation from SHERPA 2.2.11 (red) and MG5_AMC+PY8 (blue). The statistical uncertainties on the data are shown as error bars and the total combined statistical and systematic uncertainties are shown as the grey hashed bands. Statistical and systematic uncertainties on the MC simulation are not shown. The lower panels show the ratio between the data and the MC simulation which overall are in good agreement with each other.

10 Transferring R^{miss} to Particle Level

The R^{miss} ratios presented in the previous chapter require corrections to transfer the $Z \rightarrow \nu\nu +$jets and the $Z \rightarrow \ell\ell +$jets signal regions into one common phase space. This is necessary as the $p_{\mathrm{T},Z}$ spectra are measured within different phase spaces defined by the selections placed on the final state particles. On detector level, where the particles are subject to acceptance, reconstruction efficiency and resolution effects, the phase spaces of the charged lepton signal regions are restricted to correspond to the detector acceptance for the various particle types. In particular, the leptons are restricted to be within the coverage of the inner tracking detector. Such restrictions do not apply for neutrinos as they are not reconstructed within the detector nor do they suffer from inefficiencies in their reconstruction. The corrections necessary to harmonize the two processes are presented in this chapter.

The measured R^{miss} ratios in the previous chapter correspond to the detector level which sometimes is also called reconstruction level, indicating that the particles need to be reconstructed from detector signatures and thereby underlie various detector effects such as inefficiencies, resolution effects or particle mis-identification. The corresponding detector level predictions are obtained from MC simulations in which the final state particles after the parton shower are propagated through the detector simulation. Events after the simulation of the hard-scatter process are on parton level and the particle level is defined as the state after the parton shower. Particle level objects also need to be formed using partially similar methods as during the reconstruction step for the detector level objects.

Particle level electrons and muons are required to be prompt which means that they do not originate from the decay of a hadron. Dressed leptons recover most of their final state radiation by adding the four-momenta of prompt photons within a cone of $\Delta R < 0.1$ to the lepton four-momentum.

Particle level jets are formed using the $R = 0.4$ anti-k_t algorithm to cluster all stable final state particles excluding prompt, dressed leptons from W, Z, Higgs, and tau decays and prompt photons from Higgs decays. Jets including a hadron originating from a tau decay are considered as hadronically decaying taus.

The common particle level phase space into which both detector level $p_{\mathrm{T},Z}$ spectra are extrapolated is defined by the requirement of at least one particle level jet with a p_{T} exceeding 110 GeV contained within $|\eta| < 2.4$, a $p_{\text{T},Z}$ above 130 GeV and no additional prompt lepton. The particle level $p_{\text{T},Z}$ is defined as the p_{T} of the four-momenta sum of either the charged-lepton pair or the pair of the prompt neutrinos where either pair stems from a Z boson decay. The $p_{\text{T},Z}$ is hence expected to correspond to the p_{T} of the Z boson. Two effects unique to charged lepton pairs affect this $p_{\text{T},Z}$ definition. They need to be taken into account and corrected for in R^{miss}.

The final state charged leptons in the MC simulation are provided as dressed-leptons where the momenta of all prompt photons contained within a cone of $\Delta R < 0.1$ around the lepton are added to the lepton. This becomes necessary as the charged leptons undergo final state radiation where they radiate photons. These dressed leptons however are not identical to the leptons on the so-called Born level which refers to leptons before any final state radiation. The difference between these two lepton definitions arises from photons which are either radiated at large angles and hence are not added back to the lepton or from photons which stem from other processes and might be falsely added to the lepton. Only the $p_{\text{T},Z}$ of the Born level leptons corresponds to the p_{T} of the Z boson and hence is equivalent to the $p_{\text{T},Z}$ obtained from the prompt neutrino pairs. Hence, a corresponding dressed-to-Born level correction needs to be determined and applied to the $Z \to \ell\ell + \text{jets}$ signal regions.

The second effect is related to the additional interaction of charged leptons with photons which is not present for the electrical neutral neutrinos [37]. The corresponding Feynman diagrams of the production of a neutrino or a charged lepton pair in association with a radiated gluon are depicted in Figure 10.1. At the detector level, an invariant mass criterion on the charged lepton pair is placed of 25 GeV around the Z boson mass to ensure that the measured events stem mostly from Z boson decays instead of the production via virtual photons. Close to the Z boson mass the Z boson contribution is dominating whereas the γ^* contribution becomes sizeable in the tails. Moreover, the γ^* contribution diverges at low $p_{\text{T},Z}$. A generator level cut of 40 GeV is hence applied in the MC generation of the $Z \to \ell\ell + \text{jets}$ sample. This cut is not applied to the neutrinos as they do not interact with the photon. In addition no $m_{\ell\ell}$ selection is applied to the neutrinos on both detector and particle level as they cannot be directly reconstructed in the detector and are only indirectly accessible through $E_{\text{T}}^{\text{miss}}$. A correction factor is derived in simulation which extrapolates the invariant mass of the charged lepton pair to the full phase space and subtracts the γ^* contribution and the corresponding interference term.

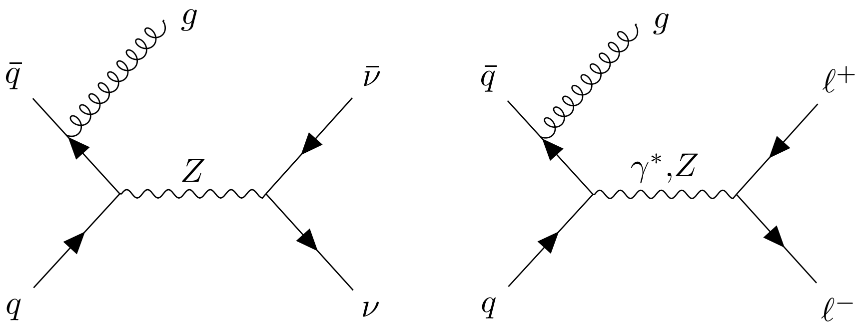

Figure 10.1: Feynman diagrams showing the production of a Z boson decaying to a neutrino pair (left) and the decay into a charged lepton pair including the additional production via a virtual photon (right). In both diagrams, a gluon is radiated from one of the initial state quarks. The Feynman diagrams are generated using the TikZ-Feynman package [135].

Both corrections related to the $p_{\mathrm{T},Z}$ of the charged lepton pairs are derived via dedicated particle level simulations performed with the PYTHIA 8.3 event generator and are applied as scale factors to R^{miss}. They are determined for electrons and muons separately and the corresponding particle level event selections are applied.

The dressed-to-Born correction is derived by comparing the event yields obtained by a reimplementation of the dressing procedure to those obtained by adding back photons to the leptons based on the simulation history, both as a function of $p_{\mathrm{T},Z}$. The matched photons are removed from the subsequent jet clustering to avoid double counting.

The size of the dressed-to-Born correction is checked with a particle level implementation of the analysis in the Rivet [136] framework, which allows a fast processing of the nominal SHERPA 2.2.11 particle level simulations, by adding the photons independently of the ΔR requirement to the closest final state lepton. The scale factors derived with PYTHIA are applied to R^{miss} as they are determined with full access to the truth record of the generator. Compatible results are found within the corresponding uncertainties and hence no additional uncertainty is applied for the difference between the two methods.

The dressed-to-Born correction is shown for both the electron and the muon channel on the left panel of Figure 10.2. The correction is about 2% at low $p_{\mathrm{T},Z}$ and slightly decreases to 1.5% in the high $p_{\mathrm{T},Z}$ tail indicating that not all final state photon radiation is correctly recovered for the dressed-leptons. This is not a problem in other analyses as the dressed-leptons are closely resembling the lepton reconstructed by the detector. The correction factors for electrons and muons are in perfect agreement with each other within their respective statistical uncertainties.

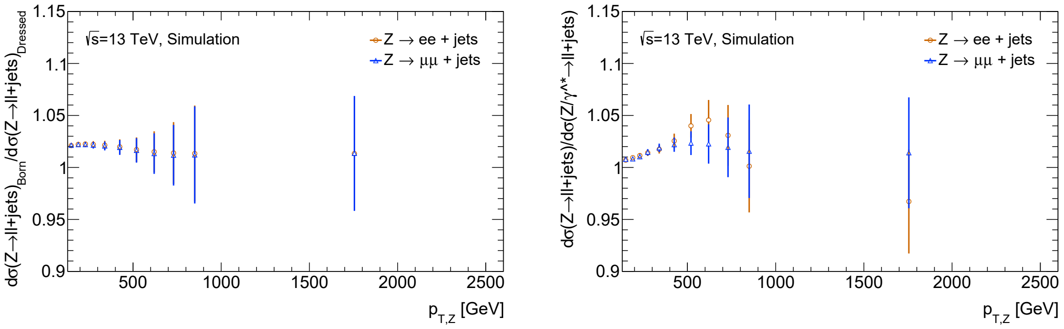

Figure 10.2: The dressed-to-Born (left) and the γ^* (right) correction as a function of $p_{\mathrm{T},Z}$ for $Z \to ee+$jets (orange) and $Z \to \mu\mu+$jets (blue). Statistical uncertainties on the scale factors are shown as error bars.

The γ^* contribution due to the interference of the γ^* and the Z boson for the charged lepton pair production is subtracted via the derivation of a corresponding $p_{\mathrm{T},Z}$ dependent scale factor which is applied to R^{miss}. At the same time, the invariant mass selection criterion on the two-lepton system is removed. This is achieved by simulating once the $Z \to \ell\ell+$jets process with the γ^* contribution and $66 < m_{\ell\ell} < 116\,\text{GeV}$, and once via a pure unconstrained Z boson production. The inverse of the division of the two event yields as a function of $p_{\mathrm{T},Z}$ gives the scale factors which are applied to the R^{miss} ratios.

The right panel of Figure 10.2 shows the size of the γ^* correction as a function of $p_{\mathrm{T},Z}$ which ranges from 1% to 2.5% for the muon channel and to values up to 5% for the electron channel. The correction factors for the electron and muon channels are in very good agreement for $p_{\mathrm{T},Z}$ below 500 GeV. At larger $p_{\mathrm{T},Z}$ the electron correction factors start to fluctuate but are still in agreement with the ones from the muon channel within the respective relatively large statistical uncertainties. The behaviour in the tail is attributed to statistical fluctuations, whereas the rise at low $p_{\mathrm{T},Z}$ is assumed to be related to a larger virtuality of the Z boson which results in more events falling outside the allowed $m_{\ell\ell}$ interval.

These two corrections are applied both to the measured R^{miss}, after the detector correction, as well as to the SM predictions obtained directly from the particle level MC simulations as they affect both in the same way. In addition to the statistical uncertainty, QCD scale uncertainties are considered which are sub-dominant and therefore not shown in Figure 10.2.

10.1 Detector Correction

A detector correction is applied to transfer the measured R^{miss} ratios from the detector to the particle level to both R^{miss} ratios. Detector effects which are typically involved can be separated into an acceptance, efficiency and resolution component.

The resolution with which each particle is reconstructed, and calibration effects can lead to events which are reconstructed in a different $p_{\text{T},Z}$ bin at the detector level than at the particle level. The bin sizes are optimised such that the bin width roughly corresponds to two standard deviations of the respective $p_{\text{T},Z}$ resolution rounded to the nearest multiple of 10 GeV, with the additional requirement that for large $p_{\text{T},Z}$ each bin should contain at least 20 measured events which allows Gaussian statistical error treatment. The bin sizes are kept strictly the same for the numerator and the denominator to construct the R^{miss} ratios. The detector response is expected to be similar between the $Z \to \nu\nu+$jets and $Z \to \ell\ell+$jets signal regions as they in first order depend on the reconstruction of the hadronic jet system which is very similar in the two regions. The near independence on the charged lepton system stems from the fact that the same leptons are first subtracted in the calculation of the $E_{\text{T}}^{\text{miss}}$ and then added again for the derivation of the $p_{\text{T},Z}$ observable[1].

The $E_{\text{T}}^{\text{miss}}$ trigger efficiency in the $Z \to \nu\nu+$jets and $Z \to \mu\mu+$jets signal regions will also have a small effect on $p_{\text{T},Z}$ close to the $E_{\text{T}}^{\text{miss}}$ trigger threshold. These effects are expected to be small and the migrations due to resolution effects in the particle reconstruction are very similar between the numerator and the denominators. The migrations are shown in Figure 10.3 for the $Z \to \nu\nu+$jets (left) and $Z \to ee+$jets (right) signal regions. These migration matrices are constructed from events which pass both the detector and the particle level selections. They are normalised such that they state the probability to find an event in a certain bin j at the detector level for an event which falls into bin i at the particle level. The chosen bin widths suggest that about 68% of the events are matched to the same bin. Two clear deviations from this approximation can be observed: in the last bin, which due to the event number restriction has a broader width, and the lowest $p_{\text{T},Z}$ bin, where the events with a smaller response are not matched at detector level. The bins in the range from 170-250 GeV have a slightly smaller probability to find the event in the respective detector level bin which is a result of the slightly finer binning used here. Migrations to the neighbouring bins are expected to be of the order of 27% and range for the bulk of the $p_{\text{T},Z}$ bins from 27-40%. These

---

[1] Small differences might occur if a lepton and a jet are very close to each other due to slightly different overlap removal procedures.

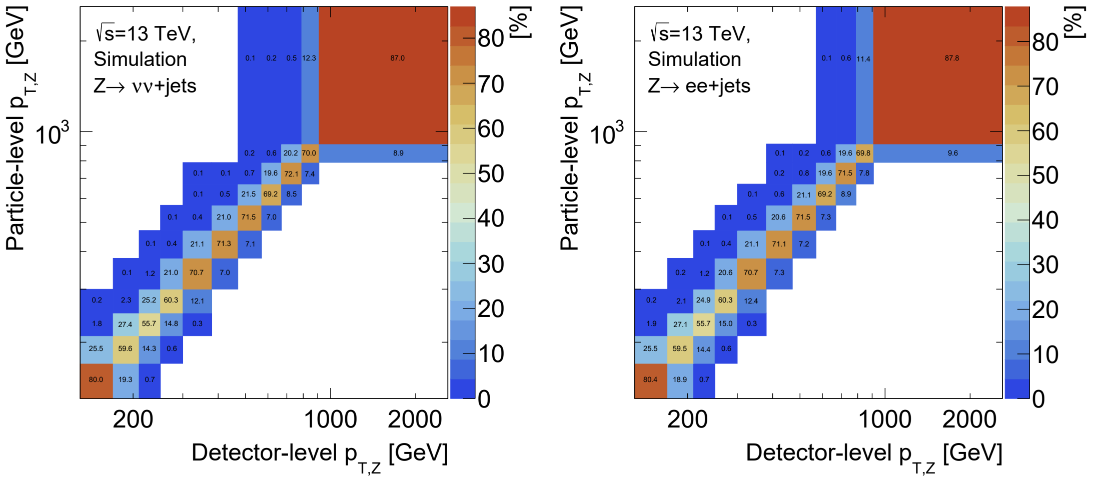

Figure 10.3: Migration matrices for the $Z \to \nu\nu+$jets (left) and $Z \to ee+$jets (right). These are normalised to state the probability of finding an event with a certain particle level $p_{\mathrm{T},Z}$ in a specific detector level bin.

migrations are not symmetric and biased towards smaller detector level $p_{\mathrm{T},Z}$ due to the exponentially falling $p_{\mathrm{T},Z}$ spectra. Larger off-diagonal migrations contribute at most 3% in both migration matrices. The two migration matrices are in good agreement with each other and thereby support the assumption of cancellation of migrations in R^{miss}.

The process of removing the detector effects from the measured result is often referred to as unfolding in analogy to the folding of the MC simulation after the parton shower with the detector response. The migrations due to resolution effects are very similar between the numerator and the denominator and therefore cancel to a large degree in the ratio. This justifies the usage of a bin-by-bin detector correction method, which neglects migrations due to resolution effects. The bin-by-bin correction procedure, which in general has a non-negligible dependence on the MC simulation used to determine the correction factors [137], is hence sufficient as this dependence cancels to a substantial degree. The main task is then to correct each bin for acceptance and efficiency effects.

The bin-by-bin correction mainly profits from being the computationally and conceptionally simpler approach. In this analysis, it is found to give consistent results with a more involved iterative Bayesian unfolding method [128] which is discussed later in this chapter. Neither, does the bin-by-bin detector correction introduce statistical uncertainties as a result of the pseudo-inversion of the folding matrix in a conventional matrix unfolding procedure or introduce a bias due to the shape modelling of the MC simulation used as the prior in a Bayesian unfolding method. In addition, correlations between the numerator and the denominator are conserved. Potential shortcomings of the simplified approach are considered by taking the difference to an alternative, more involved method as uncertainty into account as will be shown in the end of this section.

Each bin is corrected on its own and no correlations to other bins are considered. The acceptance correction uses the MC simulation to extrapolate the phase space of the charged lepton pairs to the full phase space which the neutrinos can populate. This includes the phase space outside the range of the tracker which restricts the charged lepton reconstruction at the detector level. In addition, the inefficiencies of leptons being not reconstructed, identified, or failing any other efficiency related selection requirement are corrected. Inefficiencies in the applied electron and $E_{\mathrm{T}}^{\mathrm{miss}}$ triggers are also correct in this way. In addition, effects due to the jet cleaning procedure including the f(JVT) event veto for the QCD multijet background rejection at low $p_{\mathrm{T},Z}$, and inefficiencies in the overlap removal procedure for real, close-by objects are removed by the detector correction. Finally, boundary effects at the jet or $p_{\mathrm{T},Z}$ requirements are considered which lead to events passing only the particle or the detector level selection.

Events fulfilling only the particle level requirements are called misses and are the result of inefficiencies, resolution, and boundary effects. Fakes in contrast pass only the detector level selections due to mis-identification, resolution and boundary effects. The detector correction takes these fakes and misses into account.

The detector correction factors for bin i, $C_{i,\ell}$, are obtained from MC simulations as they contain both the particle and the detector level information and are defined as

$$C_{i,\ell} = \left(\frac{N_i(Z\to\nu\nu+\text{jets})}{N_i(Z\to\ell\ell+\text{jets})}\right)^{\text{detector-level}} \Bigg/ \left(\frac{N_i(Z\to\nu\nu+\text{jets})}{N_i(Z\to\ell\ell+\text{jets})}\right)^{\text{particle-level}}, \quad (10.1)$$

where ℓ refers to either an electron or a muon and N_i represents the number of simulated events in bin i for the respective process at either the detector level or the particle level with the respective event selections applied. The values of $C_{i,\ell}$ are presented in Figure 10.4 which range from 0.3 at low $p_{\mathrm{T},Z}$ to 0.6 at high $p_{\mathrm{T},Z}$ for the $Z\to ee+\text{jets}$ channel and from 0.4 to 0.7 for the $Z\to\mu\mu+\text{jets}$ channel. The smaller values for the electron channel are due to the smaller reconstruction and identification efficiencies for the electrons and the rise to higher $p_{\mathrm{T},Z}$ is a result of the increasing reconstruction efficiencies for higher lepton transverse momenta. A sizeable fraction of the correction factor stems from the 25 GeV p_{T} requirement of the sub-leading charged lepton on detector level which is not applied at particle level. The correction factors derived from the nominal SHERPA 2.2.11 simulation are in good agreement with the ones obtained from the alternative MG5_AMC+PY8 sample for both lepton channels.

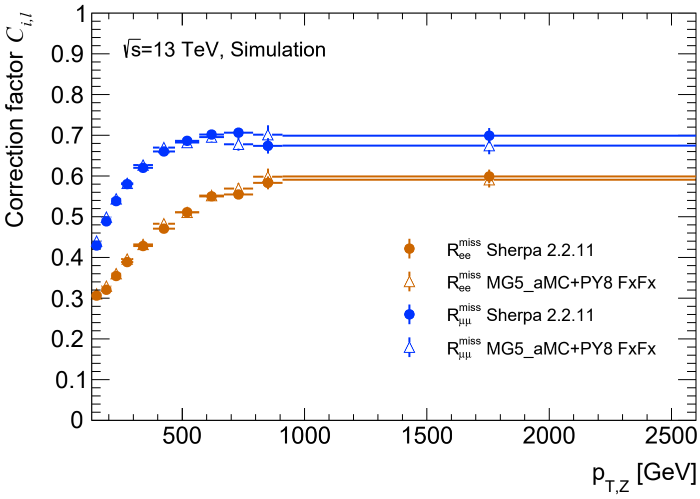

Figure 10.4: The bin-by-bin detector correction factors $C_{i,\ell}$ are presented as a function of $p_{\mathrm{T},Z}$ for R^{miss}_{ee} (orange) and $R^{\mathrm{miss}}_{\mu\mu}$ (blue). The solid circles show $C_{i,\ell}$ for the nominal SHERPA 2.2.11 simulation and the open triangles for the alternative MG5_AMC+PY8 FxFx simulation. Only statistical uncertainties on the MC simulations are displayed.

The nominal particle level R^{miss} ratios, which are corrected by the scale factor derived with the SHERPA 2.2.11 sample, and the R^{miss} ratios obtained by applying the MG5_AMC+PY8 correction factors, are then obtained by the following corrected ratio

$$R^{\mathrm{miss}}_{i,\ell\ell} = \frac{N^{\mathrm{data}}_i(Z \to \nu\nu + \mathrm{jets}) - N^{\mathrm{bkg}}_i(Z \to \nu\nu + \mathrm{jets})}{N^{\mathrm{data}}_i(Z \to \ell\ell + \mathrm{jets}) - N^{\mathrm{bkg}}_i(Z \to \ell\ell + \mathrm{jets})} \times \frac{1}{C_{i,\ell}} \, , \tag{10.2}$$

where i and ℓ denote the respective bin and the lepton channel used in the ratio. The R^{miss} ratios are compared to their corresponding MC predictions which are derived using the SHERPA 2.2.11 and the MG5_AMC+PY8 simulations as

$$R^{\mathrm{pred.}}_{i,\ell\ell} = \frac{N^{\mathrm{pred.}}_i(Z \to \nu\nu + \mathrm{jets})}{N^{\mathrm{pred.}}_i(Z \to \ell\ell + \mathrm{jets})} \, , \tag{10.3}$$

where the number of events in each bin i, $N^{\mathrm{pred.}}_i$, is determined by applying the analysis selections of the particle level fiducial phase space on the particle level objects and event quantities. To both the measured R^{miss} ratios as well as the respective MC simulations the before discussed dressed-to-Born and γ^* corrections are applied simultaneously as functions of $p_{\mathrm{T},Z}$.

In Figure 10.4 only statistical uncertainties on the MC simulations are presented whereas for the determination of the uncertainties on the R^{miss} ratios at particle level experimental and theoretical modelling uncertainties on the bin-by-bin detector correction factors are considered in addition. The relative uncertainties for R^{miss}_{ee} (top) and $R^{\mathrm{miss}}_{\mu\mu}$ (bottom) at particle level are presented in Figure 10.5 if they exceed 0.5% in any bin. The QCD multijet uncertainty from the $Z \rightarrow \nu\nu+$jets signal region is the dominant source at the low $p_{\mathrm{T},Z}$ before the QCD scale uncertainties from the predictions and the electron efficiency uncertainties take over. The tail of the $p_{\mathrm{T},Z}$ spectrum is dominated by the statistical uncertainty due to the lower event yield in the $Z \rightarrow \ell\ell+$jets signal regions. The uncertainty on the γ^* correction[2], which is mainly driven by the statistical component related to the limited number of generated events at high $p_{\mathrm{T},Z}$, grows to a comparable size to the electron efficiency uncertainties. The uncertainties related to the jet energy scale are sub-leading in contrast to the individual $p_{\mathrm{T},Z}$ measurements as they are assumed to be correlated and cancel to a large degree in the ratio. The relative uncertainties for the $Z \rightarrow \mu\mu+$jets ratio are similar to the $Z \rightarrow ee+$jets ratio but the muon efficiency uncertainties are slightly smaller than the electron counterparts. The bin with the smallest uncertainty has a relative uncertainty of roughly 4% (3%) in the R^{miss}_{ee} ($R^{\mathrm{miss}}_{\mu\mu}$) ratio.

Residual biases due to the detector correction method are studied by comparing the R^{miss} ratios obtained via the bib-by-bin correction to the ratios of $Z \rightarrow \nu\nu+$jets and $Z \rightarrow \ell\ell+$jets which are derived by individually unfolding them via iterative Bayesian unfolding [128] using the RooUnfold framework [138]. The R^{miss} ratios are obtained after two unfolding iterations of the corresponding background subtracted measured event yields where the respective SM signal MC simulations are taken as priors. The two iterations are a compromise between a reduced bias on the prior, which reduces as the number of iterations increases, and statistical fluctuations which grow with an increasing number of iterations. The non-closure between the two detector correction methods is below 2% and is taken as an uncertainty.

---

[2] The uncertainty of the γ^* correction implicitly refers to both the γ^* and the dressed-to-Born correction uncertainty as they share the same sources of uncertainties being derived from a common MC sample.

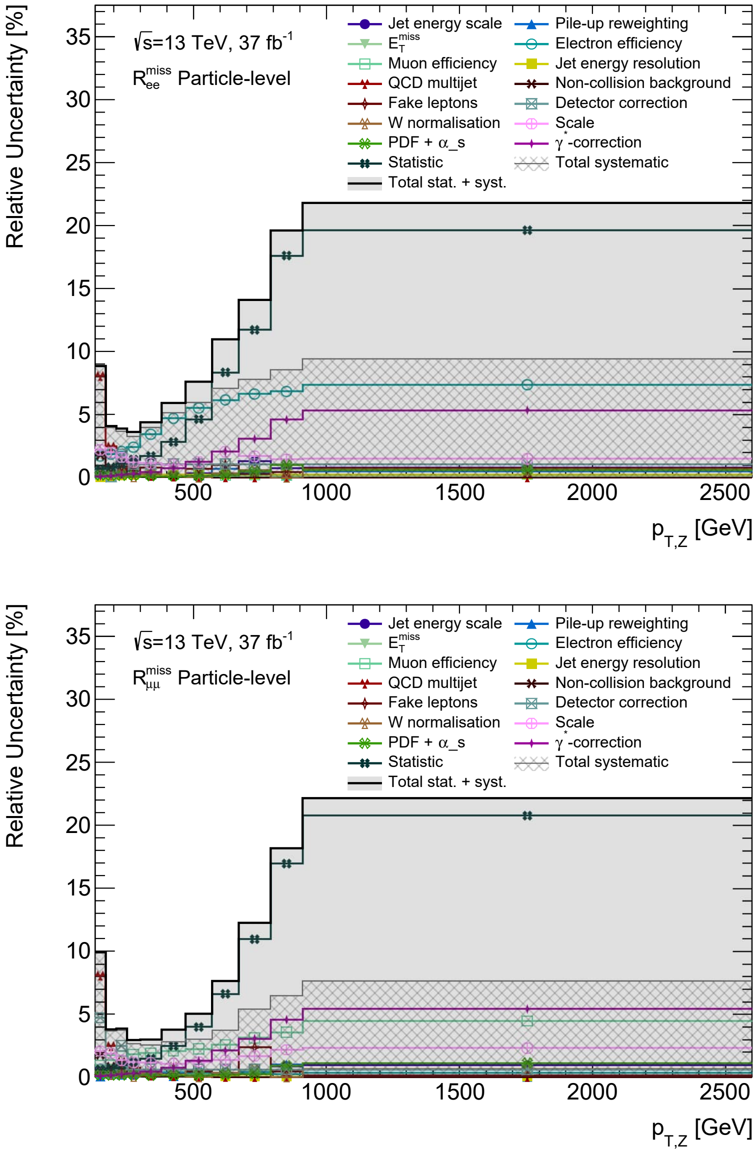

Figure 10.5: Relative uncertainties on the R^{miss}_{ee} (top) and $R^{\text{miss}}_{\mu\mu}$ (bottom) ratio at particle level. Only systematic uncertainties with a contribution of at least 0.5% in any bin are presented. The shown uncertainties are symmetrized.

11 Particle Level Results and Γ_Z(inv) Extraction

The result of this measurement is presented in this chapter. Both the R^{miss} ratios and the Γ_Z(inv) are compared to theory predictions and the latter to results from previous measurements of Γ_Z(inv) and the agreement is discussed in the context of the statistical and systematic uncertainties.

First, the measured R^{miss} ratios after the application of the corrections presented in Chapter 10 are shown in Section 11.1 on particle level. They are compared to their SM predictions to ensure that the features of the R^{miss} ratios are properly understood before they are used to determine the invisible width of the Z boson. Within the statistical interpretation, the best fit value of the R^{miss} ratios, $\hat{R}^{\mathrm{miss}}$, with the corresponding uncertainty is extracted via a χ^2 minimisation. The result is directly translated into Γ_Z(inv) through the multiplication of the leptonic partial decay width of the Z boson measured at LEP. This is presented in Section 11.2. In addition, the impact of the uncertainties on the final result is discussed. Finally, the Γ_Z(inv) value is compared to both direct and indirect measurements and interpreted in the context of the number of light neutrino families in Section 11.3.

11.1 Particle Level R^{miss} Ratios

The measured R^{miss}_{ee} (top) and $R^{\mathrm{miss}}_{\mu\mu}$ (bottom) ratios, corrected for detector effects and the γ^* contribution, are shown on particle (Born) level in Figure 11.1. Both R^{miss} ratios based on the detector correction derived with SHERPA 2.2.11 and MG5_AMC+PY8 are presented. The ratio with the SHERPA 2.2.11 detector correction is taken as the nominal. They are in good agreement with each other within the respective uncertainties.

These measured particle level R^{miss} ratios are compared to their SHERPA 2.2.11 and MG5_AMC+PY8 Born level predictions[1]. The predictions themselves show only minor differences from each other in the high-$p_{\mathrm{T},Z}$ tail which are covered by their statistical uncertainties. The data and the respective predictions are in good agreement within their combined statistical and systematic uncertainties, except for a deviation slightly above $2\,\sigma$ in the range from 570-670 GeV in R^{miss}_{ee} which is discussed in the corresponding

---

[1] Both data and predictions are corrected for the γ^* contribution.

detector level Figure 9.3. The data and the predictions agree within 2% ranging from 170-300 GeV and are well contained within the respective $1\,\sigma$ uncertainty bands, as are most of the bins with higher $p_{\mathrm{T},Z}$. The measured R^{miss}_{ee} at the highest $p_{\mathrm{T},Z}$ bin is roughly 15% below the electroweak prediction which is attributed to an upward fluctuation in the number of observed events in the $Z \rightarrow ee+\text{jets}$ signal region. This deviation is nevertheless almost consistent with the prediction within the $1\,\sigma$ uncertainty band due to the large statistical uncertainty of this bin. In the lowest $p_{\mathrm{T},Z}$ bin in the $R^{\text{miss}}_{\mu\mu}$ spectrum the measured R^{miss} is around 5% larger than the prediction but this deviation is covered by the respective uncertainties in this bin which are dominated by the multijet and detector correction uncertainties.

The measured R^{miss} ratios are nearly constant as a function of $p_{\mathrm{T},Z}$ and close to the value of 5.966 obtained from the electroweak calculations of the branching fractions (Equation 2.7). This clearly differs from the detector level distributions shown in Figure 9.3 which indicates that the applied corrections are able to remove the $p_{\mathrm{T},Z}$ dependence. An additional difference to the detector level ratios is that the relative uncertainties on the R^{miss} ratios on particle level increase slightly. This is a result of the statistical uncertainties in the MC simulations, theory modelling uncertainties, as well as experimental uncertainties, which are introduced through the detector correction and the γ^* correction.

The SM predictions shown in Figure 11.1 are also nearly independent of $p_{\mathrm{T},Z}$ as expected. Only in the electron channel, they show a deviation from this assumption at high $p_{\mathrm{T},Z}$. This is attributed to statistical fluctuations in the applied γ^* correction which can be seen in Figure 10.2 by comparing the electron and muon correction. These do not impact the overall precision of the measurement as they occur at high $p_{\mathrm{T},Z}$. The statistical uncertainties on the predictions and the uncertainties from the γ^* correction, including a statistical and a theoretical modelling uncertainty component, are added in quadrature and are shown as the capital-I error bars on both predictions. These indicate that the predictions are consistent with a flat-line assumption within their respective uncertainties.

The measured R^{miss} ratios at the particle level are consistent with the SM predictions and as they do not show any anomalous structures they are used to extract the invisible width of the Z boson.

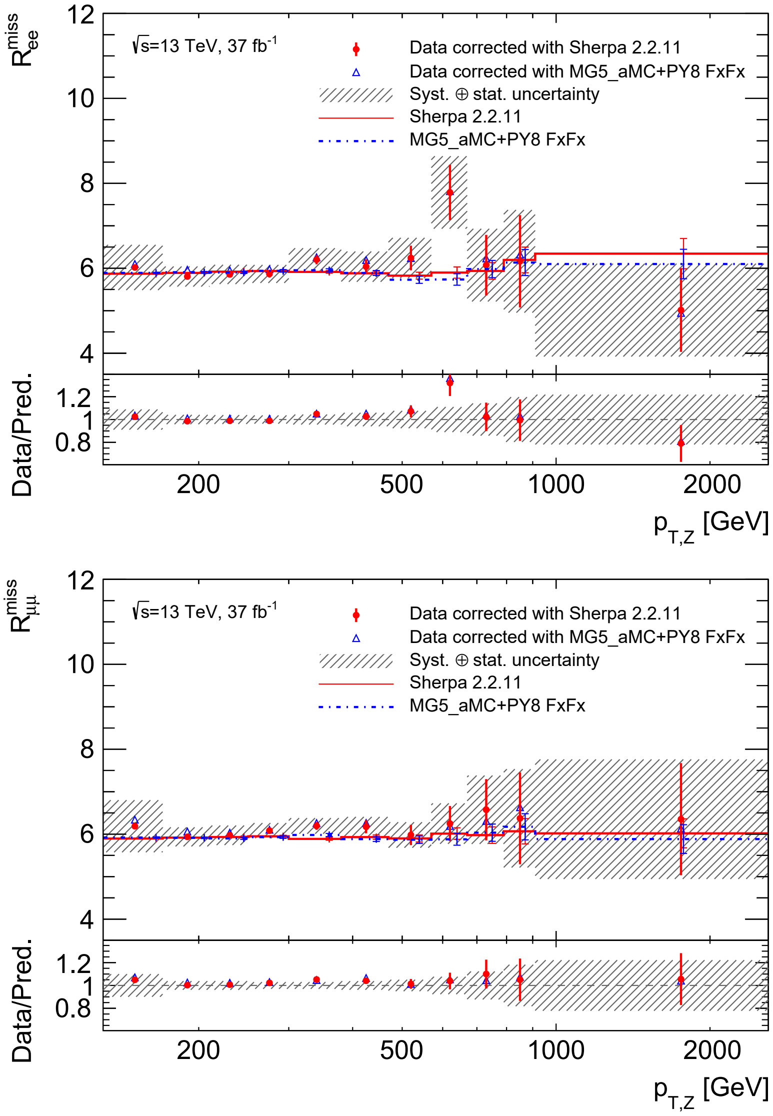

Figure 11.1: The measured R^{miss}_{ee} (top) and $R^{\mathrm{miss}}_{\mu\mu}$ (bottom) ratios as a function of $p_{\mathrm{T},Z}$ are presented in the particle level phase space. The statistical uncertainties on the data are shown as error bars and the total combined statistical and systematic uncertainties are shown as the grey hashed bands. The ratios are compared to the Sherpa 2.2.11 (red) and MG5_aMC+Py8 (blue) particle level predictions. The corresponding statistical uncertainties together with uncertainties on the applied γ^* correction are shown as the capital-I error bars. The lower panels show the ratio between the data and the predictions which overall are in good agreement with each other within the respective uncertainty bands.

11.2 Extraction of $\Gamma_Z(\mathrm{inv})$

The invisible width of the Z boson can be obtained by multiplying the best fit value, $\hat{R}^{\mathrm{miss}}$, obtained from a simultaneous χ^2 minimisation of the R^{miss}_{ee} and $R^{\mathrm{miss}}_{\mu\mu}$ ratios by the $\Gamma_Z(\ell\ell)$ width [6] which was obtained at LEP under the assumption of lepton universality. The widths for the electron and the muon channel are first separately derived before the invisible width is determined using both ratios simultaneously as inputs in the fit.

The nominal particle level R^{miss} ratios (presented in Section 11.1) are used to extract $\Gamma_Z(\mathrm{inv})$. The $Z \to \nu\nu+$jets and $Z \to \ell\ell+$jets processes can be factorised into the cross section of the production of the Z boson in association with a jet and in the corresponding branching fractions. The measured event yields used to construct the R^{miss} ratios then correspond to the ratio of the respective branching fractions as the production of the Z boson + jets cancels within the ratio. The ratio of branching fractions corresponds to the ratio of the invisible and the charged lepton partial decay widths assuming only SM contributions which is justified as until today no experimental evidence for exotic decays beyond the SM are found in this channel [119]:

$$R^{\mathrm{miss}} = \frac{\frac{d\sigma(Z\to\nu\nu+\mathrm{jets})}{dp_{\mathrm{T},Z}}}{\frac{d\sigma(Z\to\ell\ell+\mathrm{jets})}{dp_{\mathrm{T},Z}}} = \frac{\frac{d\sigma(Z+\mathrm{jets})\times\mathrm{BR}(Z\to\nu\nu)}{dp_{\mathrm{T},Z}}}{\frac{d\sigma(Z+\mathrm{jets})\times\mathrm{BR}(Z\to\ell\ell)}{dp_{\mathrm{T},Z}}} = \frac{\mathrm{BR}(Z\to\nu\nu)}{\mathrm{BR}(Z\to\ell\ell)} = \frac{\Gamma_Z(\mathrm{inv})}{\Gamma_Z(\ell\ell)}\ . \tag{11.1}$$

The explicit $p_{\mathrm{T},Z}$ dependent of R^{miss} and of the two ratios of branching fractions and partial decay widths is omitted in the above equation, given that these are considered to be constant as a function of $p_{\mathrm{T},Z}$ which is a result of the detector correction. Nevertheless, the R^{miss} ratios are still binned in $p_{\mathrm{T},Z}$. Every measured $p_{\mathrm{T},Z}$ bin in the particle level R^{miss} ratios corresponds to an individual measurement of the ratio of the invisible to the charged lepton partial decay width of the Z boson. The systematic uncertainties of these measurements are correlated across bins and channels which are incorporated in a single covariance matrix. The covariance matrix is constructed by assuming all systematic uncertainty sources to be fully correlated between bins and channels and the statistical uncertainties to be uncorrelated. This is a good assumption as for example, the jet-related uncertainties of the hadronic recoil of the Z boson are largely independent of the boson decay in boson + jet processes, or the lepton uncertainties which are object dependent. The resulting covariance matrix is displayed in Figure 11.2. The bin indices

1-10 correspond to the 10 $p_{\mathrm{T},Z}$ bins of the R^{miss}_{ee} distribution from 170-2600 GeV, whereas the bins 11-20 represent the respective $R^{\text{miss}}_{\mu\mu}$ $p_{\mathrm{T},Z}$ bins[2].

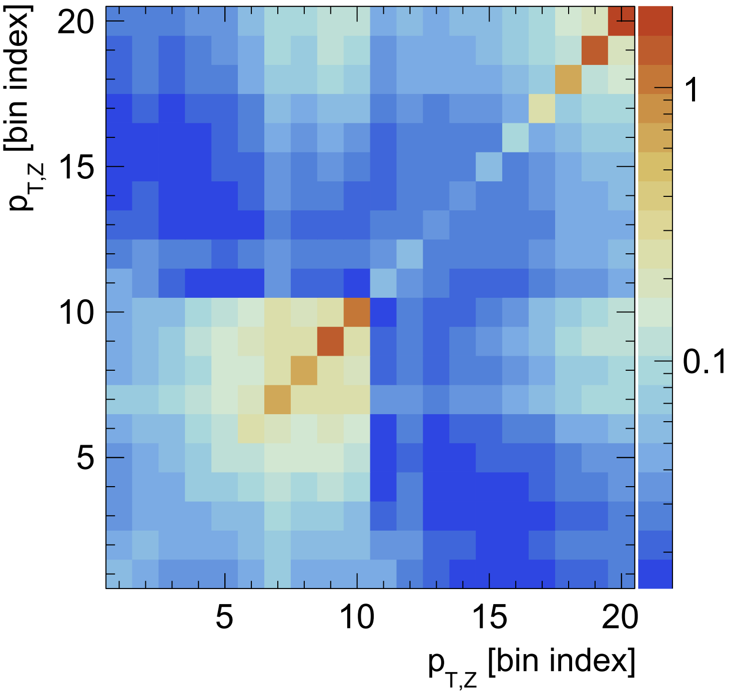

Figure 11.2: Covariance matrix of the R^{miss}_{ee} (bin indices 1-10) and $R^{\text{miss}}_{\mu\mu}$ (bin indices 11-20) ratios for $p_{\mathrm{T},Z}$ from 170-2600 GeV.

The largest values in each row or column are in general on the diagonal which also contains the uncorrelated statistical uncertainty component. A general trend of increasing covariance values towards higher $p_{\mathrm{T},Z}$ is observed. The covariances within each R^{miss} ratio are typically larger than the off-diagonal terms between the electron and the muon ratios. The larger covariance between the high $p_{\mathrm{T},Z}$ R^{miss}_{ee} and $R^{\text{miss}}_{\mu\mu}$ is attributed to the sizeable γ^* correction uncertainty which is correlated between the two ratios.

The covariances in the high $p_{\mathrm{T},Z}$ tail for the ratio with the electron denominator are larger than for the muon denominator as they are dominated by the electron efficiency uncertainties which are 6-7.5% compared to the corresponding muon efficiency uncertainties of 3-4.5%. The fourth R^{miss}_{ee} bin (bin index 3) and the fourth and fifth $R^{\text{miss}}_{\mu\mu}$ bin (bin index 13, 14) have the smallest covariance values and hence drive the overall precision of the measurement. These bins have small covariances between the two channels

---

[2] The lowest $p_{\mathrm{T},Z}$ bin from 130-170 GeV is not used in the extraction of the invisible width, which is discussed in more detail at a later point in this section, and therefore not shown.

as they are dominated by either the electron or the muon efficiency uncertainties which are besides residual effects in the $Z \to \nu\nu +$jets signal region uncorrelated.

At low $p_{\mathrm{T},Z}$ the covariance values are very similar for R^{miss}_{ee}, $R^{\text{miss}}_{\mu\mu}$ and for their cross terms as the main uncertainty contributions are the QCD multijet uncertainty and correlated QCD scale uncertainties in the $Z \to \nu\nu +$jets signal region which are present in both ratios. One additional feature is that in the R^{miss}_{ee} ratio, the penultimate bin has a larger covariance value even if the last bin has the larger total uncertainty which stems from a downward fluctuation of the central R^{miss}_{ee} value in the last bin as the covariance is determined from the product of the relative uncertainty and R^{miss}.

The uncertainty on the final $\Gamma_Z(\text{inv})$ measurement is obtained via this covariance matrix where all uncorrelated sources of uncertainties are added. These appear in either or both the subtracted background contribution and the detector-correction factors.

For the extraction of $\Gamma_Z(\text{inv})$ via a linear χ^2 fit it is important that the prediction is constant and hence independent of $p_{\mathrm{T},Z}$. In [25] it was extensively studied and shown that the R^{miss} ratios are constant as a function of $p_{\mathrm{T},Z}$ on the particle level, as long as the following conditions are met: final state QED radiation must be suppressed, the γ^* contribution must be absent, and no phase space selection criteria are allowed to be placed on the visible Z boson decay final states, which explicitly includes an overlap removal with close by jets at the detector level. All these requirements are fulfilled for the common particle level phase space defined in this measurement to which the R^{miss}_{ee} and $R^{\text{miss}}_{\mu\mu}$ ratios are transferred. The flatness of the predictions and the measured R^{miss} in the particle level phase space is seen in Figure 11.1. This justifies the extraction of the estimator of R^{miss} via a χ^2 minimisation following the approach of best linear unbiased estimators [139–141]. The χ^2 function which is minimised to obtain $\hat{R}^{\text{miss}}$ is defined as

$$\chi^2 = \mathbf{\Delta}^T \mathbf{V}^{-1} \mathbf{\Delta}, \tag{11.2}$$

where $\Delta_i = R^{\text{miss}}_{\text{data,i}} - \hat{R}^{\text{miss}}$ is the i^{th} component of a vector running over all $p_{\mathrm{T},Z}$ bins of both the R^{miss}_{ee} and the $R^{\text{miss}}_{\mu\mu}$ ratio, $R^{\text{miss}}_{\text{data,i}}$ is the respective measured ratio, $\hat{R}^{\text{miss}}$ is the estimator of the ratio which is independent of i, and $\mathbf{V}^{-1}$ represents the inverse covariance matrix. The correlations between both $Z \to \ell\ell +$jets regions are considered in the covariance matrix. In the construction of the covariance matrix all relative systematic uncertainties, which are not related to data-driven background estimation method uncertainties, are then propagated onto $\hat{R}^{\text{miss}}$ to stabilise the minimisation as proposed in [137].

It is observed that including the lowest $p_{\mathrm{T},Z}$ ranging from 130-170 GeV introduces a bias towards a lower central value in the extraction of $\hat{R}^{\mathrm{miss}}$. This type of bias has been observed before in other combinations of individual measurements with a large correlated normalisation uncertainty compared to small statistical uncertainties and is for example discussed in [137, 142]. The large correlations are attributed to the large QCD multijet uncertainty of 7.7% (Table 7.2) in this bin to neighbouring bins and across the two R^{miss} ratios. The central value or the overall precision of the measurement in a χ^2 minimisation where the uncertainties are considered uncorrelated is not impacted by the exclusion of this lowest $p_{\mathrm{T},Z}$ bin. This indicates that the influence of neglecting the first $p_{\mathrm{T},Z}$ bin in the actual minimisation is expected to be minimal and therefore this bin is excluded following an approach suggested in [140].

In a first step, the agreement between the data and the SHERPA 2.2.11 SM prediction shown in Figure 11.1 is evaluated. To derive a quantitative statement the p-value is determined which describes the goodness-of-fit which is defined as [137]

$$p = \int_{\chi^2_{\mathrm{obs}}}^{\infty} f_{\mathrm{NDF}}(z)dz \ . \tag{11.3}$$

Here χ^2_{obs} is the observed χ^2 and f_{NDF} is the χ^2 function with the number of degrees of freedom NDF. A reduced χ^2 of 20.5/20 is found for both R^{miss} measurements considering the bins used in the extraction of $\hat{R}^{\mathrm{miss}}$ which corresponds to a p-value of 0.43. This indicates that the prediction and the data are in good agreement.

The Γ_Z(inv) extraction is performed three times to obtain Γ_Z(inv) separately from both lepton channels and finally using the combined input, by multiplying the result with the respective $\Gamma_Z(\ell^+\ell^-)$ values obtained by the LEP experiments [6]. The partial widths of the Z boson for the charged leptons are summarised in Table 11.1. In the derivation of $\Gamma_Z(\ell^+\ell^-)$ lepton universality was assumed.

Z Partial Width	Value [MeV]
$\Gamma_Z(e^+e^-)$	83.91 ± 0.12
$\Gamma_Z(\mu^+\mu^-)$	83.99 ± 0.18
$\Gamma_Z(\ell^+\ell^-)$	83.984 ± 0.086

Table 11.1: Summary of the charged lepton partial decay widths obtained by the LEP experiments [1, 6].

The values obtained for $\Gamma_Z(\text{inv})$ using solely R^{miss}_{ee} or $R^{\text{miss}}_{\mu\mu}$ are

$$\Gamma_{Z,ee}(\text{inv}) = 490 \pm 3\ (\text{stat.}) \pm 16\ (\text{syst.})\,\text{MeV and} \tag{11.4}$$

$$\Gamma_{Z,\mu\mu}(\text{inv}) = 511 \pm 2\ (\text{stat.}) \pm 13\ (\text{syst.})\,\text{MeV}\ . \tag{11.5}$$

Both are dominated by systematic uncertainties. They are in agreement with each other and agree with the SM prediction of $\Gamma_Z(\text{inv})$ within their uncertainties even if the value obtained from the electron channel is slightly lower and the result from the muon channel slightly above the SM prediction of 501.445±0.047 MeV [1]. The χ^2 value determined in the fit in the electron channel is 12.2. A total of 10 $p_{\text{T},Z}$ bins are used to derive $\hat{R}^{\text{miss}}_{ee}$ which leaves 9 degrees of freedom. This translates into a p-value of 0.20 which indicates reasonable agreement between the data and $\hat{R}^{\text{miss}}_{\mu\mu}$. This can be understood as the data is overall well described by the SM prediction but fluctuates in some $p_{\text{T},Z}$ bins in the R^{miss}_{ee} ratio. For the muon channel $\chi^2/NDF = 3.6/9$ is obtained from the χ^2 minimisation which corresponds to a p-value of 0.94 indicating that $\hat{R}^{\text{miss}}_{\mu\mu}$ describes the data well.

$\hat{R}^{\text{miss}}$ is obtained from a simultaneous χ^2 minimisation including both R^{miss} ratios as they are corrected to the same phase space. In this case, the covariance matrix spans both channels and the systematic uncertainties are assumed to be correlated between the two ratios. The same χ^2 minimisation as for the results obtained from the individual channels yields a combined result of $\hat{R}^{\text{miss}} = 6.030 \pm 0.149$ which translates in

$$\Gamma_Z(\text{inv}) = 506 \pm 2\ (\text{stat.}) \pm 12\ (\text{syst.})\,\text{MeV}\ . \tag{11.6}$$

This shows that the measurement of the invisible width of the Z boson is systematically limited. The combined reduced χ^2 is 17.3/19 as the fit still has only one degree of freedom but considers all 20 bins. This translates to a p-value of 0.57 which shows very good agreement between the measured R^{miss} and $\hat{R}^{\text{miss}}$, where the latter describes the data even better than the Sherpa 2.2.11 SM predictions.

With a precision of 2.5%, the obtained result represents the single most precise direct determination of $\Gamma_Z(\text{inv})$ obtained to date and the central value is in excellent agreement with the SM prediction of 501.445 ± 0.047 MeV [1].

The extraction of $\hat{R}^{\text{miss}}$ via the χ^2 minimisation is cross-checked with a maximum likelihood fit of a function of a multivariate normal distribution where the k systematic sources of uncertainties are treated as floating nuisance parameters θ which are constrained by Gaussian priors G with means $\mu = 0$ and widths $\sigma = 1$ [22, 143]. For better readability $\mathbf{R}^{\text{miss}}$ is in the discussion of the likelihood function replaced by $\mathbf{y}$:

$$\mathcal{L}\left(\hat{\mathbf{y}},\theta|\mathbf{y}_{\text{data}}\right)=\frac{1}{\sqrt{(2\pi)^k|\mathbf{V}|}}\cdot \mathrm{e}^{-\frac{1}{2}\chi^2(\mathbf{y}_{\text{data}},\hat{\mathbf{y}},\theta)}\cdot\prod_{i\in\text{syst}}^{k}G\left(\theta_i\right). \tag{11.7}$$

In this approach, the covariance matrix $\mathbf{V}$ only contains the statistical uncertainties. The systematic uncertainties, with $1\,\sigma$ variations δ_i, are described by nuisance parameters which leads to a modified χ^2 function

$$\chi^2\left(\mathbf{y}_{\text{data}},\hat{\mathbf{y}},\theta\right)=\left(\mathbf{y}_{\text{data}}-\hat{\mathbf{y}}-\sum_i^k\theta_i\delta_i\right)^T\mathbf{V}^{-1}\left(\mathbf{y}_{\text{data}}-\hat{\mathbf{y}}-\sum_i^k\theta_i\delta_i\right). \tag{11.8}$$

Maximising the likelihood function in Equation 11.7 to extract the parameter of interest $\hat{\mathbf{y}}$ is equivalent to a minimisation of the negative log-likelihood (NLL) function. The latter gives a consistent result of 506 ± 2 (stat.) $\pm\, 12$ (syst.) MeV to the $\hat{R}^{\text{miss}}$ obtained from the χ^2 minimisation[3]. This additional extraction is not only crucial to check the convergence of the χ^2 minimisation method but also, in addition, provides valuable information about the systematic uncertainties.

Figure 11.3 presents the 25 nuisance parameters θ with the largest pulls before and after the NLL minimisation. The nuisance parameters which are constrained by more than 10% are the multijet background, the γ^* correction, as well as electron and muon efficiencies which are all among the dominant uncertainties in a particular $p_{\text{T},Z}$ range. None of these are over-constrained and range from 0.6-0.9. The QCD multijet and the lepton efficiencies are in addition slightly pulled to compensate for the non-flatness and the different offsets in the measured electron and muon R^{miss} ratios. Additional uncertainties related to the lepton fake estimates are slightly pulled. This is due to the fact that electron uncertainties play no crucial role in the $R^{\text{miss}}_{\mu\mu}$ ratio and vice versa. The R^{miss}_{ee} and $R^{\text{miss}}_{\mu\mu}$ ratios yield different central values of $\hat{R}^{\text{miss}}$ which are consistent with each other within uncertainties. The lepton efficiency nuisance parameters are hence pulled to minimise these differences between the two R^{miss} spectra. The nuisance parameter related to the non-collision background uncertainty is pulled in the same direction as the parameter of the QCD multijet uncertainty to compensate for shape differences in the low $p_{\text{T},Z}$ regime compared to the rest of the $p_{\text{T},Z}$ spectra. However, none of these nuisance parameters is unnaturally pulled by more than $1\,\sigma$.

The linearity of the problem to extract $\hat{R}^{\text{miss}}$ allows the determination of this value

---

[3] The two results are identical apart from floating point differences.

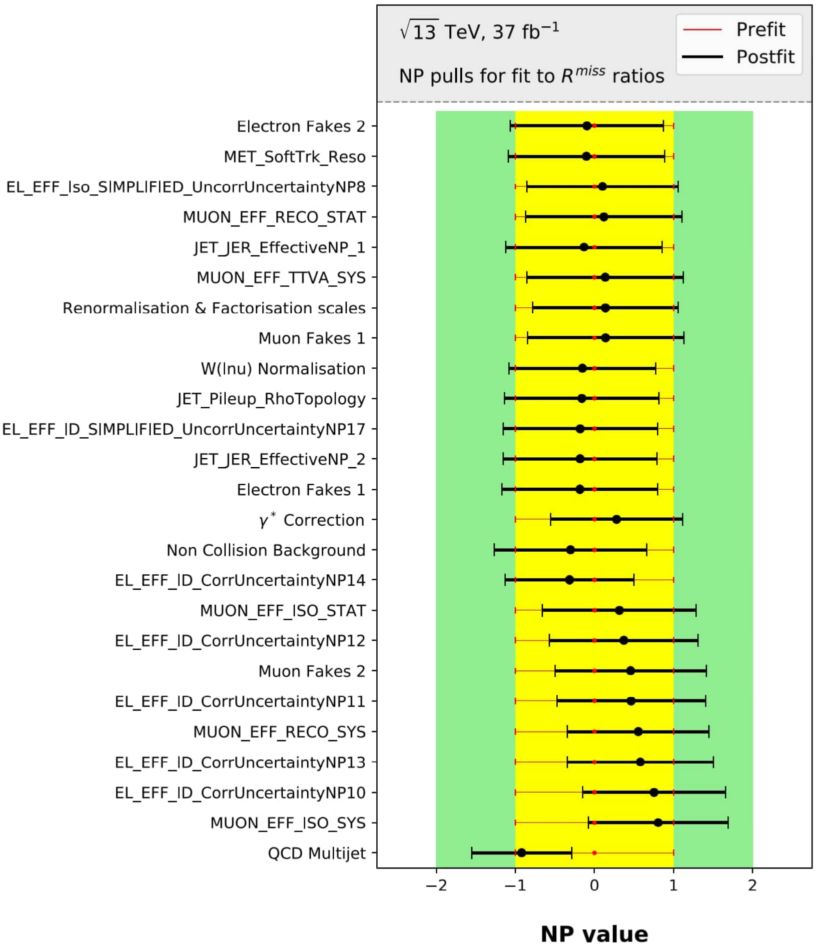

Figure 11.3: The 25 nuisance parameters with the largest deviation from $\mu = 0$ (pull) are shown before (red bar) and after (black bar) the minimisation of the NLL. No pull outside the yellow band is observed which indicates the $1\,\sigma$ boundary.

by simple matrix multiplication of the form $\left(\mathbf{A}\mathbf{V}^{-1}\mathbf{R}^{\mathbf{miss}^{T}}_{\text{data}}\right) / \left(\mathbf{A}\mathbf{V}^{-1}\mathbf{A}^{T}\right)$ where $\mathbf{A}$ is the 1-vector of size n where n is given by the dimensionality of the covariance matrix $\mathbf{V}$ which equals the length of the vector of the measured values of the two ratios $\mathbf{R}^{\mathbf{miss}}_{\text{data}}$ [144]. The corresponding result of 506 MeV is also consistent with the previous methods.

Impact of the Systematic Uncertainties on the Precision of the Measurement

The impact on the precision of the $\Gamma_Z(\text{inv})$ measurement of each source of systematic uncertainty is evaluated by repeating the χ^2 minimisation including all uncertainties except the one for which the impact is evaluated. The impact of the uncertainties on the

$\Gamma_Z(\text{inv})$ is presented in Table 11.2 and depends on the respective sizes of the uncertainties but also on their relative contributions to the bins with the largest sensitivity as the importance of each bin is effectively weighted by the total combined uncertainty of the bin. This becomes evident for the muon efficiency uncertainty, which has the largest impact on the result of 7.4 MeV, even if the electron efficiencies are larger in every R^{miss}_{ee} bin compared to the respective muon efficiency uncertainty in the corresponding $R^{\text{miss}}_{\mu\mu}$ ratio. The electron efficiency uncertainty nevertheless has an impact of 4.9 MeV on the measurement as they are one of the dominant uncertainties in the electron channel. In the most sensitive bins, the muon efficiencies are still above 2%, which is about 30% larger than the impact on $\Gamma_Z(\text{inv})$ of 1.5%, indicating that the R^{miss}_{ee} contributes towards the precision of the combination. Other uncertainties with a sizeable impact are the over both R^{miss} ratios correlated renormalisation and factorisation scale uncertainties with an impact of 5.9 MeV, the detector correction uncertainty (4.4 MeV), and the likewise correlated QCD multijet (3.2 MeV) and $E_{\text{T}}^{\text{miss}}$ (2.4 MeV) uncertainties which are both related to the numerator of the ratio. These six uncertainties yield a total impact of 12.2 MeV if they are added in quadrature. They are responsible for about 95% of the total impact on the $\Gamma_Z(\text{inv})$ measurement. A complete list with the impact of every considered uncertainty source is presented in Table 11.2 where the impact on $\Gamma_Z(\text{inv})$ for every uncertainty component not explicitly mentioned is below 2 MeV or 0.4%. The total impact is derived by adding the individual sources in quadrature and is found to be 12.9 MeV which is slightly larger than the 12.4 MeV systematic uncertainty obtained from the fit. It is important to note that they are not expected to match each other and the total impact is in general larger than the combined systematic uncertainty.

11.3 Discussion of the $\Gamma_Z(\text{inv})$ Result

The precision of the presented measurement of $\Gamma_Z(\text{inv})$ is mostly limited by systematic uncertainties which are mainly dominated by the lepton efficiency uncertainties from the denominators of the R^{miss} ratios. The overall precision of 13 MeV represents the single most precise direct measurement of the invisible width of the Z boson with a relative uncertainty corresponding to 2.5%. Figure 11.4 shows this result which is about 20% more precise than the LEP combination of the direct measurements and the result from the CMS experiment. The result derived in this analysis (denoted as ATLAS) is compared to the direct measurements of L3, OPAL, ALPEH, their LEP combination as well as the second measurement performed at the LHC by CMS. The indirect measurement obtained from the lineshape measurements of the visible widths at LEP assuming

Systematic Uncertainty Impact on Γ_Z(inv)	in [MeV]	in [%]
Muon efficiency	7.4	1.5
Renormalisation & factorisation scales	5.9	1.2
Electron efficiency	4.9	1.0
Detector correction	4.4	0.9
QCD multijet	3.2	0.6
$E_{\mathrm{T}}^{\mathrm{miss}}$	2.4	0.5
$Z(\to \mu\mu)$+jets lepton fake estimate	1.9	0.4
Jet energy resolution	1.6	0.3
$W(\to \ell\nu)$+jets normalisation	1.5	0.3
Pile-up reweighting	1.5	0.3
Non-collision background estimate	1.3	0.3
Jet energy scale	1.3	0.3
γ^*-correction	1.0	0.2
$Z(\to ee)$+jets lepton fake estimate	1.0	0.2
Luminosity	1.0	0.2
Parton distribution functions + α_s	0.7	0.1
$\Gamma_Z(\ell^+\ell^-)$ [1, 6]	0.5	0.1
Tau energy scale	0.4	0.1
Muon momentum scale	0.3	0.1
$W(\to \ell\nu)$+jets lepton fake estimate	0.3	0.1
(Forward) jet vertex tagging	0.2	< 0.1
Top subtraction scheme	0.2	< 0.1
Electron energy scale	0.1	< 0.1
Systematic	12	2.4
Statistical	2	0.4
Total	13	2.5

Table 11.2: The impact on Γ_Z(inv) of the different sources of systematic uncertainties. The total uncertainty is not expected to match the quadratic sum of the individual impacts of the uncertainties.

lepton universality is also shown in this summary plot. The precision of this indirect measurement remains with 499.0 ± 1.5 MeV [6] about one order of magnitude more precise than the direct measurements. The SM prediction which includes $\mathcal{O}(\alpha_s^4)$ and $\mathcal{O}(\alpha^2)$ corrections of 501.445 ± 0.047 MeV [1] is also presented. The stated uncertainty on the prediction is mainly impacted by the precision with which the Higgs and top quark masses are measured.

The direct LEP and LHC Γ_Z(inv) measurements are all in good agreement with each other within their respective uncertainties and are compatible with both the indirect

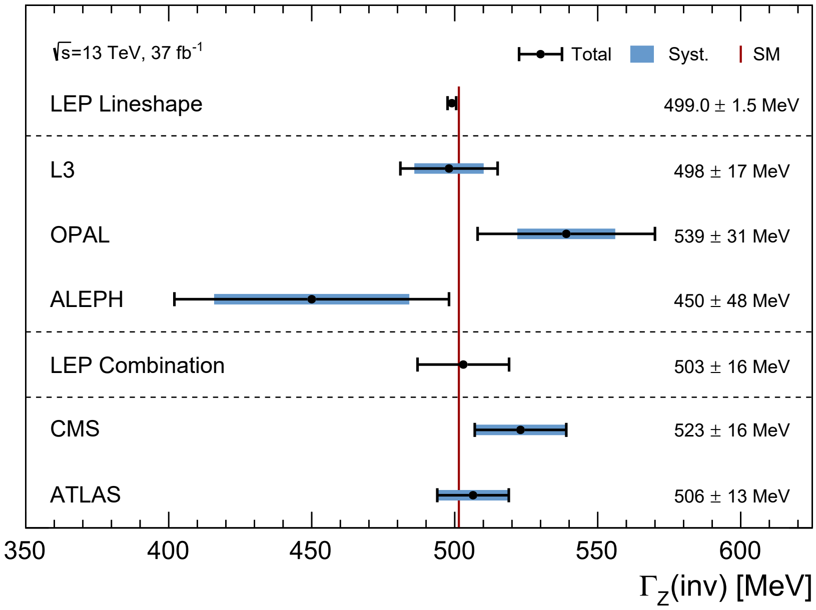

Figure 11.4: Direct measurements of Γ_Z(inv) by the L3, OPAL and ALEPH experiments at LEP and their combination, and by the CMS experiment at the LHC are presented together with the ATLAS result derived in this analysis. The total uncertainties are shown as the black error bars and the systematic uncertainties are represented by the blue bands. For the LEP combination, only the total uncertainty is displayed. The indirect measurement obtained from the lineshape fits to the data of the four LEP experiments and also states only its total uncertainty. The SM prediction from electroweak precision calculations is shown as the red solid line.

LEP result as well as with the SM prediction. This constitutes an important consistency check as any deviation from the SM prediction could indicate a sign of new physics and disagreements between the direct and the indirect Γ_Z(inv) results can provide valuable information on the underlying nature of such a potential source.

The obtained result is consistent with the SM and therefore provides no indication of physics beyond the SM influencing the Z boson invisible width. The measured value of $\hat{R}^{\text{miss}}$ is hence interpreted in terms of the number of light neutrino families N_ν. The SM prediction of the ratio of the partial decay widths of the Z boson in a pair of neutrinos or charged leptons is more precisely known as the individual widths. Assuming SM couplings and a single neutrino generation this gives $(\Gamma_Z^{\nu\nu}/\Gamma_Z^{\ell\ell})_{\text{SM}} = 1.99060 \pm 0.00021$ [44]. Comparing this prediction to the extracted $\hat{R}^{\text{miss}}$ ratio yields $N_\nu = 3.029 \pm 0.075$ which is in excellent agreement with the SM expectation of three neutrino families.

12 Summary

The electroweak sector of the Standard Model is very well understood and highly predictive, as its entire structure is determined by only a few parameters in contrast to a large number of observables able to test it. One key observable is the invisible width of the Z boson, $\Gamma_Z(\text{inv})$, which allows the determination of the number of light neutrino generations.

In the presented analysis, the $\Gamma_Z(\text{inv})$ is determined via ratio measurements of Z boson decays into either pairs of neutrinos or first and second generation charged lepton pairs in association with at least one highly energetic jet using $37\,\text{fb}^{-1}$ of proton-proton collisions at 13 TeV collected by the ATLAS detector at the Large Hadron Collider. The Z boson decays into neutrinos cannot be directly measured as neutrinos typically do not interact with the detector. The momentum imbalance in the transverse plane, the missing transverse momentum, is used as a proxy to measure the p_{T} of the neutrino pair for the $Z \to \nu\nu+\text{jets}$ process, which forms the numerator in both ratios. A common observable, $p_{\text{T},Z}$, is obtained by the vector sum of the transverse momenta of the charged leptons and $E_{\text{T}}^{\text{miss}}$ in the two $Z \to \ell\ell+\text{jets}$ processes. These form the denominators of the two independent R^{miss} ratios in the electron and in the muon channel. Dedicated event selection criteria are put in place to efficiently select these three processes.

Nevertheless, several background processes are able to pass these event selections. They are either modelled by Monte Carlo simulations, if their contributions are small, or determined via various data-driven methods which utilise information from both the data and the MC simulations to derive robust background estimates. A correct description of the background and signal processes is evaluated by comparing them to the measured spectra as a function of $p_{\text{T},Z}$. A good agreement within the statistical and systematic uncertainties in the three signal regions is observed. This justifies the subtraction of the background events from the data to construct the two R^{miss} ratios, which are $p_{\text{T},Z}$ dependent.

The $Z \to \nu\nu+\text{jets}$ and $Z \to \ell\ell+\text{jets}$ signal regions must be in a common phase space to eliminate this dependence. The limited angular acceptance of the ATLAS detector and the finite reconstruction efficiencies for the charged lepton pairs are the main factors which make a detector correction necessary. The measured R^{miss} spectra are transferred to the particle level by the application of correction factors derived in MC simulations. As a result of the detector correction R^{miss}_{ee} and $R^{\mathrm{miss}}_{\mu\mu}$ are constant as a function of $p_{\mathrm{T},Z}$ and their best estimator, $\hat{R}^{\mathrm{miss}}$, is extracted via a χ^2 minimisation.

The invisible width of the Z boson is finally obtained from a combination of $\Gamma_Z(\ell\ell)$ measured at LEP with $\hat{R}^{\mathrm{miss}}$ determined in the presented analysis:

$$\Gamma_Z(\mathrm{inv}) = 506 \pm 2\,(\mathrm{stat.}) \pm 12\,(\mathrm{syst.})\ \mathrm{MeV}\ ,$$

where the result is systematically limited by the efficiency uncertainties of the charged leptons. This measurement of $\Gamma_Z(\mathrm{inv})$ is in excellent agreement with the Standard Model prediction and also with previous measurements performed at LEP and the LHC. This result represents the to date single most precise measurement of this parameter based on $E_{\mathrm{T}}^{\mathrm{miss}}$ in the final state. The agreement with the SM leaves only a limited space for new physics contributions in this channel and justifies the interpretation in terms of the number of light neutrino generations, which is found to be $N_\nu = 3.029 \pm 0.075$.

Bibliography

[1] Particle Data Group, R. L. Workman, et al. Review of Particle Physics. *PTEP*, 2022:083C01, 2022. doi:10.1093/ptep/ptac097.

[2] N. Aghanim et al. Planck 2018 results. VI. Cosmological parameters. *Astron. Astrophys.*, 641:A6, 2020. doi:10.1051/0004-6361/201833910. [Erratum: Astron.Astrophys. 652, C4 (2021)].

[3] G. Bertone and D. Hooper. History of dark matter. *Rev. Mod. Phys.*, 90(4):045002, 2018. doi:10.1103/RevModPhys.90.045002.

[4] UA1 Collaboration. Experimental observation of lepton pairs of invariant mass around 95 GeV/c2 at the CERN SPS collider. *Physics Letters B*, 126(5):398–410, 1983. ISSN 0370-2693. doi:https://doi.org/10.1016/0370-2693(83)90188-0.

[5] UA2 Collaboration. Evidence for $Z^0 \to e^+e^-$ at the CERN pp collider. *Physics Letters B*, 129(1):130–140, 1983. ISSN 0370-2693. doi:https://doi.org/10.1016/0370-2693(83)90744-X.

[6] S. Schael et al. Precision electroweak measurements on the Z resonance. *Phys. Rept.*, 427:257–454, 2006. doi:10.1016/j.physrep.2005.12.006.

[7] ALEPH Collaboration. Measurement of the Z resonance parameters at LEP. *Eur. Phys. J. C*, 14:1, 2000. doi:https://doi.org/10.1007/s100520000319.

[8] DELPHI Collaboration. Cross-sections and leptonic forward-backward asymmetries from the Z^0 running of LEP. *Eur. Phys. J. C*, 16:371, 2000. doi:https://doi.org/10.1007/s100520000392.

[9] L3 Collaboration. Measurement of cross sections and forward-backward asymmetries at the Z resonance and determination of electroweak parameters. *Eur. Phys. J. C*, 16:1, 2000. doi:https://doi.org/10.1007/s100520050001.

[10] OPAL Collaboration. Precise determination of the Z resonance parameters at LEP: ‘Zedometry’. *Eur. Phys. J. C*, 19:587, 2001. doi:https://doi.org/10.1007/s100520100627.

[11] ALEPH Collaboration. A direct measurement of the invisible width of the Z from single photon counting. *Phys. Lett. B*, 313:520, 1993. doi:https://doi.org/10.1016/0370-2693(93)90027-F.

[12] L3 Collaboration. Determination of the number of light neutrino species from single photon production at LEP. *Phys. Lett. B*, 431:199, 1998. doi:https://doi.org/10.1016/S0370-2693(98)00519-X.

[13] OPAL Collaboration. Measurement of single photon production in e+e collisions near the Z^0 resonance. *Z. Phys. C*, 65:47, 1995. doi:https://doi.org/10.1007/BF01571303.

[14] CMS Collaboration. Precision measurement of the Z boson invisible width in pp collisions at s=13 TeV. *Phys. Lett. B*, 842:137563, 2023. doi:10.1016/j.physletb.2022.137563.

[15] M. Carena, A. de Gouvea, A. Freitas, and M. Schmitt. Invisible Z boson decays at e+ e- colliders. *Phys. Rev. D*, 68:113007, 2003. doi:10.1103/PhysRevD.68.113007.

[16] ATLAS Collaboration. Reconstruction, Energy Calibration, and Identification of Hadronically Decaying Tau Leptons in the ATLAS Experiment for Run-2 of the LHC. ATL-PHYS-PUB-2015-045, 2015. `https://cds.cern.ch/record/2064383`.

[17] ATLAS Collaboration. A precise measurement of the Z-boson double-differential transverse momentum and rapidity distributions in the full phase space of the decay leptons with the ATLAS experiment at $\sqrt{s} = 8$ TeV. ATLAS-CONF-2023-013, 2023. `https://cds.cern.ch/record/2854867`.

[18] ATLAS Collaboration. A precise determination of the strong-coupling constant from the recoil of Z bosons with the ATLAS experiment at $\sqrt{s} = 8$ TeV. ATLAS-CONF-2023-015, 2023. `https://cds.cern.ch/record/2855244`.

[19] ATLAS Collaboration. ATLAS data quality operations and performance for 2015–2018 data-taking. *JINST*, 15:P04003, 2020. doi:10.1088/1748-0221/15/04/P04003.

[20] G. Hiller and F. Kruger. More model-independent analysis of $b \to s$ processes. *Phys. Rev. D*, 69:074020, 2004. doi:10.1103/PhysRevD.69.074020.

[21] G. Aad et al. Performance of the upgraded preprocessor of the atlas level-1 calorimeter trigger. *Journal of Instrumentation*, 15(11):P11016, nov 2020. doi:10.1088/1748-0221/15/11/P11016.

[22] E. Nurse et al. Detector-corrected cross-sections in events with large missing transverse momentum in association with jets. Technical report, CERN, Geneva, 2019. https://cds.cern.ch/record/2702246.

[23] S. M. Weber. *Measurement of Vector Boson plus Jet Production Cross Sections and Dark Matter Interpretation with the ATLAS Detector*. PhD thesis, Heidelberg U., 2023. https://doi.org/10.11588/heidok.00032929.

[24] ATLAS Collaboration. Measurement of detector-corrected observables sensitive to the anomalous production of events with jets and large missing transverse momentum in pp collisions at $\sqrt{s} = 13\,\text{TeV}$ using the ATLAS detector. *Eur. Phys. J. C*, 77:765, 2017. doi:10.1140/epjc/s10052-017-5315-6.

[25] P.-H. Beauchemin and H. Son. Standard Model sensitivity studies for the $Z \to \nu\nu$+jets to $Z \to \ell\ell$+jets cross section ratio. Technical report, CERN, Geneva, 2018. https://cds.cern.ch/record/2300106.

[26] ATLAS Collaboration. Measurement of the Z boson invisible width at $\sqrt{s} = 13$ TeV with the ATLAS detector. ATLAS-CONF-2023-053, 2023. https://atlas.web.cern.ch/Atlas/GROUPS/PHYSICS/CONFNOTES/ATLAS-CONF-2023-053/.

[27] S. L. Glashow. Partial-symmetries of weak interactions. *Nuclear Physics*, 22(4): 579–588, 1961. ISSN 0029-5582. doi:https://doi.org/10.1016/0029-5582(61)90469-2.

[28] A. Salam. Weak and Electromagnetic Interactions. *Conf. Proc. C*, 680519:367–377, 1968. doi:10.1142/9789812795915_0034.

[29] S. Weinberg. A model of leptons. *Phys. Rev. Lett.*, 19:1264–1266, Nov 1967. doi:10.1103/PhysRevLett.19.1264.

[30] D. Galbraith and C. Burgard. Standard Model of the Standard Model. http://davidgalbraith.org/portfolio/ux-standard-model-of-the-standard-model.

[31] ATLAS Collaboration. Observation of a new particle in the search for the Standard Model Higgs boson with the ATLAS detector at the LHC. *Phys. Lett. B*, 716:1, 2012. doi:10.1016/j.physletb.2012.08.020.

[32] CMS Collaboration. Observation of a new boson at a mass of 125 GeV with the CMS experiment at the LHC. *Phys. Lett. B*, 716:30, 2012. doi:10.1016/j.physletb.2012.08.021.

[33] P. W. Higgs. Broken symmetries and the masses of gauge bosons. *Phys. Rev. Lett.*, 13:508–509, Oct 1964. doi:10.1103/PhysRevLett.13.508.

[34] F. Englert and R. Brout. Broken symmetry and the mass of gauge vector mesons. *Phys. Rev. Lett.*, 13:321–323, Aug 1964. doi:10.1103/PhysRevLett.13.321.

[35] G. S. Guralnik, C. R. Hagen, and T. W. B. Kibble. Global conservation laws and massless particles. *Phys. Rev. Lett.*, 13:585–587, Nov 1964. doi:10.1103/PhysRevLett.13.585.

[36] A. Pich. The standard model of electroweak interactions, 2007. `https://doi.org/10.48550/arXiv.0705.4264`.

[37] M. Thomson. *Modern Particle Physics*. Cambridge University Press, 2013. doi:10.1017/CBO9781139525367.

[38] P. Langacker. *The standard model and beyond*. Taylor & Francis, 2010. ISBN 978-1-4200-7906-7. doi:10.1201/b22175.

[39] P. Z. Skands. QCD for Collider Physics. In *2010 European School of High Energy Physics*, 4 2011. doi:10.48550/arXiv.1104.2863.

[40] N. Cabibbo. Unitary symmetry and leptonic decays. *Phys. Rev. Lett.*, 10:531–533, Jun 1963. doi:10.1103/PhysRevLett.10.531.

[41] M. Kobayashi and T. Maskawa. CP-Violation in the Renormalizable Theory of Weak Interaction. *Progress of Theoretical Physics*, 49(2):652–657, 02 1973. ISSN 0033-068X. doi:10.1143/PTP.49.652.

[42] J. Erler and M. Schott. Electroweak precision tests of the standard model after the discovery of the higgs boson. *Progress in Particle and Nuclear Physics*, 106: 68–119, 2019. ISSN 0146-6410. doi:https://doi.org/10.1016/j.ppnp.2019.02.007.

[43] G. Voutsinas, E. Perez, M. Dam, and P. Janot. Beam-beam effects on the luminosity measurement at LEP and the number of light neutrino species. *Phys. Lett. B*, 800:135068, 2020. doi:10.1016/j.physletb.2019.135068.

[44] P. Janot and S. Jadach. Improved Bhabha cross section at LEP and the number of light neutrino species. *Phys. Lett. B*, 803:135319, 2020. doi:10.1016/j.physletb.2020.135319.

[45] T. S. Pettersson and P. Lefèvre. The Large Hadron Collider: conceptual design. Technical report, 1995. `https://cds.cern.ch/record/291782`.

[46] O. S. Brüning, P. Collier, P. Lebrun, S. Myers, R. Ostojic, J. Poole, and P. Proudlock. *LHC Design Report*. CERN Yellow Reports: Monographs. CERN, Geneva, 2004. doi:10.5170/CERN-2004-003-V-1.

[47] L. Evans and P. Bryant. Lhc machine. *JINST*, 3(08):S08001, aug 2008. doi:10.1088/1748-0221/3/08/S08001.

[48] ATLAS Collaboration. The ATLAS Experiment at the CERN Large Hadron Collider. *JINST*, 3:S08003, 2008. doi:10.1088/1748-0221/3/08/S08003.

[49] CMS Collaboration. The CMS Experiment at the CERN LHC. *JINST*, 3:S08004, 2008. doi:10.1088/1748-0221/3/08/S08004.

[50] LHCb Collaboration. The LHCb Detector at the LHC. *JINST*, 3:S08005, 2008. doi:10.1088/1748-0221/3/08/S08005.

[51] ALICE Collaboration. The ALICE experiment at the CERN LHC. *JINST*, 3: S08002, 2008. doi:10.1088/1748-0221/3/08/S08002.

[52] C. Lefèvre. The CERN accelerator complex. Complexe des accélérateurs du CERN. 2008. `https://cds.cern.ch/record/1260465`.

[53] ATLAS Collaboration. Luminosity determination in pp collisions at $\sqrt{s} = 13$ TeV using the ATLAS detector at the LHC. 12 2022. `https://cds.cern.ch/record/2844887`.

[54] H. Bartosik et al. Injectors Beam Performance Evolution during Run 2. In *9th LHC Operations Evian Workshop*, pages 51–58, 2019. `https://cds.cern.ch/record/2750276`.

[55] R. Bruce et al. Review of LHC Run 2 Machine Configurations. In *9th LHC Operations Evian Workshop*, pages 187–197, Geneva, Switzerland, 2019. `https://cds.cern.ch/record/2750415`.

[56] ATLAS Collaboration. ATLAS Insertable B-Layer: Technical Design Report. 2010. https://cds.cern.ch/record/1291633.

[57] ATLAS Collaboration. Performance of the ATLAS trigger system in 2015. *Eur. Phys. J. C*, 77:317, 2017. doi:10.1140/epjc/s10052-017-4852-3.

[58] ATLAS Collaboration. Performance of the upgraded PreProcessor of the ATLAS Level-1 Calorimeter Trigger. *JINST*, 15:P11016, 2020. doi:10.1088/1748-0221/15/11/P11016.

[59] T. Sjostrand. Monte Carlo Tools. In *65th Scottish Universities Summer School in Physics: LHC Physics*, pages 309–339, 11 2009. doi:10.1201/b11865-14.

[60] A. Buckley et al. General-purpose event generators for LHC physics. *Phys. Rept.*, 504:145–233, 2011. doi:10.1016/j.physrep.2011.03.005.

[61] G. Altarelli and G. Parisi. Asymptotic freedom in parton language. *Nuclear Physics B*, 126(2):298–318, 1977. ISSN 0550-3213. doi:https://doi.org/10.1016/0550-3213(77)90384-4.

[62] V. N. Gribov and L. N. Lipatov. Deep inelastic e p scattering in perturbation theory. *Sov. J. Nucl. Phys.*, 15:438–450, 1972. https://cds.cern.ch/record/427157.

[63] Y. L. Dokshitzer. Calculation of the Structure Functions for Deep Inelastic Scattering and e+ e- Annihilation by Perturbation Theory in Quantum Chromodynamics. *Sov. Phys. JETP*, 46:641–653, 1977.

[64] B. Andersson, G. Gustafson, G. Ingelman, and T. Sjöstrand. Parton fragmentation and string dynamics. *Physics Reports*, 97(2):31–145, 1983. ISSN 0370-1573. doi:https://doi.org/10.1016/0370-1573(83)90080-7.

[65] B. R. Webber. A QCD Model for Jet Fragmentation Including Soft Gluon Interference. *Nucl. Phys. B*, 238:492–528, 1984. doi:10.1016/0550-3213(84)90333-X.

[66] D. Yennie, S. Frautschi, and H. Suura. The infrared divergence phenomena and high-energy processes. *Annals of Physics*, 13(3):379–452, 1961. ISSN 0003-4916. doi:https://doi.org/10.1016/0003-4916(61)90151-8.

[67] W. Buttinger. Using Event Weights to account for differences in Instantaneous Luminosity and Trigger Prescale in Monte Carlo and Data. Technical report, CERN, Geneva, 2015. https://cds.cern.ch/record/2014726.

[68] ATLAS Collaboration. The ATLAS Simulation Infrastructure. *Eur. Phys. J. C*, 70:823, 2010. doi:10.1140/epjc/s10052-010-1429-9.

[69] GEANT4 Collaboration, S. Agostinelli, et al. GEANT4 – a simulation toolkit. *Nucl. Instrum. Meth. A*, 506:250, 2003. doi:10.1016/S0168-9002(03)01368-8.

[70] E. Bothmann et al. Event generation with Sherpa 2.2. *SciPost Phys.*, 7(3):034, 2019. doi:10.21468/SciPostPhys.7.3.034.

[71] P. Nason. A new method for combining NLO QCD with shower Monte Carlo algorithms. *JHEP*, 11:040, 2004. doi:10.1088/1126-6708/2004/11/040.

[72] S. Frixione, P. Nason, and C. Oleari. Matching NLO QCD computations with parton shower simulations: the POWHEG method. *JHEP*, 11:070, 2007. doi:10.1088/1126-6708/2007/11/070.

[73] S. Alioli, P. Nason, C. Oleari, and E. Re. A general framework for implementing NLO calculations in shower Monte Carlo programs: the POWHEG BOX. *JHEP*, 06:043, 2010. doi:10.1007/JHEP06(2010)043.

[74] T. Sjöstrand, S. Ask, J. R. Christiansen, R. Corke, N. Desai, P. Ilten, S. Mrenna, S. Prestel, C. O. Rasmussen, and P. Z. Skands. An introduction to PYTHIA 8.2. *Comput. Phys. Commun.*, 191:159, 2015. doi:10.1016/j.cpc.2015.01.024.

[75] J. Alwall et al. The automated computation of tree-level and next-to-leading order differential cross sections, and their matching to parton shower simulations. *JHEP*, 07:079, 2014. doi:10.1007/JHEP07(2014)079.

[76] ATLAS Collaboration. ATLAS Pythia 8 tunes to 7 TeV data. ATL-PHYS-PUB-2014-021, 2014. `https://cds.cern.ch/record/1966419`.

[77] R. D. Ball et al. Parton distributions for the LHC run II. *JHEP*, 04:040, 2015. doi:10.1007/JHEP04(2015)040.

[78] R. D. Ball et al. Parton distributions from high-precision collider data. *Eur. Phys. J. C*, 77(10):663, 2017. doi:10.1140/epjc/s10052-017-5199-5.

[79] ATLAS Collaboration. Modelling and computational improvements to the simulation of single vector-boson plus jet processes for the ATLAS experiment. *JHEP*, 08:089, 2021. doi:10.1007/JHEP08(2022)089.

[80] ATLAS Collaboration. *ATLAS Computing: technical design report.* Technical design report. ATLAS. CERN, Geneva, 2005. `https://cds.cern.ch/record/837738`.

[81] M. Cacciari, G. P. Salam, and G. Soyez. The anti-k_t jet clustering algorithm. *JHEP*, 04:063, 2008. doi:10.1088/1126-6708/2008/04/063.

[82] S. Catani, Y. L. Dokshitzer, M. H. Seymour, and B. R. Webber. Longitudinally invariant K_t clustering algorithms for hadron hadron collisions. *Nucl. Phys. B*, 406:187–224, 1993. doi:10.1016/0550-3213(93)90166-M.

[83] S. D. Ellis and D. E. Soper. Successive combination jet algorithm for hadron collisions. *Phys. Rev. D*, 48:3160–3166, 1993. doi:10.1103/PhysRevD.48.3160.

[84] Y. L. Dokshitzer, G. D. Leder, S. Moretti, and B. R. Webber. Better jet clustering algorithms. *JHEP*, 08:001, 1997. doi:10.1088/1126-6708/1997/08/001.

[85] M. Wobisch and T. Wengler. Hadronization corrections to jet cross-sections in deep inelastic scattering. In *Workshop on Monte Carlo Generators for HERA Physics (Plenary Starting Meeting)*, pages 270–279, 4 1998. doi:10.48550/arXiv.hep-ph/9907280.

[86] ATLAS Collaboration. Topological cell clustering in the ATLAS calorimeters and its performance in LHC Run 1. *Eur. Phys. J. C*, 77:490, 2017. doi:10.1140/epjc/s10052-017-5004-5.

[87] ATLAS Collaboration. Jet reconstruction and performance using particle flow with the ATLAS Detector. *Eur. Phys. J. C*, 77:466, 2017. doi:10.1140/epjc/s10052-017-5031-2.

[88] ATLAS Collaboration. Jet energy scale and resolution measured in proton–proton collisions at $\sqrt{s} = 13\,\text{TeV}$ with the ATLAS detector. *Eur. Phys. J. C*, 81:689, 2020. doi:10.1140/epjc/s10052-021-09402-3.

[89] ATLAS Collaboration. Reconstruction of primary vertices at the ATLAS experiment in Run 1 proton–proton collisions at the LHC. *Eur. Phys. J. C*, 77:332, 2017. doi:10.1140/epjc/s10052-017-4887-5.

[90] M. Cacciari and G. P. Salam. Pileup subtraction using jet areas. *Physics Letters B*, 659(1):119–126, 2008. ISSN 0370-2693. doi:https://doi.org/10.1016/j.physletb.2007.09.077.

[91] J. M. Lindert et al. Precise predictions for $V+$ jets dark matter backgrounds. *Eur. Phys. J. C*, 77(12):829, 2017. doi:10.1140/epjc/s10052-017-5389-1.

[92] ATLAS Collaboration. Standard Model Summary Plots February 2022. Technical report, CERN, Geneva, 2022. `http://cds.cern.ch/record/2804061`.

[93] ATLAS Collaboration. Tagging and suppression of pileup jets with the ATLAS detector. ATLAS-CONF-2014-018, 2014. `https://cds.cern.ch/record/1700870`.

[94] ATLAS Collaboration. Forward jet vertex tagging using the particle flow algorithm. ATL-PHYS-PUB-2019-026, 2019. `https://cds.cern.ch/record/2683100`.

[95] ATLAS Collaboration. Identification and rejection of pile-up jets at high pseudorapidity with the ATLAS detector. *Eur. Phys. J. C*, 77:580, 2017. doi:10.1140/epjc/s10052-017-5081-5.

[96] ATLAS Collaboration. Electron and photon performance measurements with the ATLAS detector using the 2015–2017 LHC proton–proton collision data. *JINST*, 14:P12006, 2019. doi:10.1088/1748-0221/14/12/P12006.

[97] ATLAS Collaboration. Electron reconstruction and identification in the ATLAS experiment using the 2015 and 2016 LHC proton–proton collision data at $\sqrt{s} = 13\,\text{TeV}$. *Eur. Phys. J. C*, 79:639, 2019. doi:10.1140/epjc/s10052-019-7140-6.

[98] ATLAS Collaboration. Electron and photon energy calibration with the ATLAS detector using 2015–2016 LHC proton–proton collision data. *JINST*, 14:P03017, 2019. doi:10.1088/1748-0221/14/03/P03017.

[99] ATLAS Collaboration. Measurement of the photon identification efficiencies with the ATLAS detector using LHC Run 2 data collected in 2015 and 2016. *Eur. Phys. J. C*, 79:205, 2019. doi:10.1140/epjc/s10052-019-6650-6.

[100] ATLAS Collaboration. Muon reconstruction and identification efficiency in ATLAS using the full Run 2 pp collision data set at $\sqrt{s} = 13\,\text{TeV}$. *Eur. Phys. J. C*, 81:578, 2021. doi:10.1140/epjc/s10052-021-09233-2.

[101] ATLAS Collaboration. Muon reconstruction performance of the ATLAS detector in proton–proton collision data at $\sqrt{s} = 13\,\text{TeV}$. *Eur. Phys. J. C*, 76:292, 2016. doi:10.1140/epjc/s10052-016-4120-y.

[102] ATLAS Collaboration. Studies of the muon momentum calibration and performance of the ATLAS detector with pp collisions at $\sqrt{s} = 13$ TeV. *Eur. Phys. J. C*, 83(8):686, 2023. doi:10.1140/epjc/s10052-023-11584-x.

[103] T. Barillari et al. Local Hadronic Calibration. Technical report, CERN, Geneva, 2008. `https://cds.cern.ch/record/1112035`.

[104] ATLAS Collaboration. Measurement of the tau lepton reconstruction and identification performance in the ATLAS experiment using pp collisions at $\sqrt{s} = 13$ TeV. ATLAS-CONF-2017-029, 2017. `https://cds.cern.ch/record/2261772`.

[105] ATLAS Collaboration. Identification of hadronic tau lepton decays using neural networks in the ATLAS experiment. ATL-PHYS-PUB-2019-033, 2019. `https://cds.cern.ch/record/2688062`.

[106] ATLAS Collaboration. $E_{\mathrm{T}}^{\mathrm{miss}}$ performance in the ATLAS detector using 2015–2016 LHC pp collisions. ATLAS-CONF-2018-023, 2018. `https://cds.cern.ch/record/2625233`.

[107] ATLAS Collaboration. Performance of missing transverse momentum reconstruction with the ATLAS detector using proton–proton collisions at $\sqrt{s} = 13\,\mathrm{TeV}$. *Eur. Phys. J. C*, 78:903, 2018. doi:10.1140/epjc/s10052-018-6288-9.

[108] ATLAS Collaboration. Performance of the missing transverse momentum triggers for the ATLAS detector during Run-2 data taking. *JHEP*, 08:080, 2020. doi:10.1007/JHEP08(2020)080.

[109] ATLAS Collaboration. Luminosity determination in pp collisions at $\sqrt{s} = 13\,\mathrm{TeV}$ using the ATLAS detector at the LHC. 2022.

[110] G. Avoni et al. The new LUCID-2 detector for luminosity measurement and monitoring in ATLAS. *JINST*, 13(07):P07017, 2018. doi:10.1088/1748-0221/13/07/P07017.

[111] ATLAS. Internal Communication.

[112] ATLAS Collaboration. Performance of electron and photon triggers in ATLAS during LHC Run 2. *Eur. Phys. J. C*, 80:47, 2020. doi:10.1140/epjc/s10052-019-7500-2.

[113] ATLAS Collaboration. Selection of jets produced in 13 TeV proton–proton collisions with the ATLAS detector. ATLAS-CONF-2015-029, 2015. https://cds.cern.ch/record/2037702.

[114] J. Gonski. Jet Cleaning in 2016 and the Event Level Cleaning Tool. Technical report, CERN, Geneva, 2017. https://cds.cern.ch/record/2272136.

[115] D. Adams et al. Recommendations of the Physics Objects and Analysis Harmonisation Study Groups 2014. Technical report, CERN, Geneva, 2014. https://cds.cern.ch/record/1743654.

[116] ATLAS Collaboration. Beam-induced and cosmic-ray backgrounds observed in the ATLAS detector during the LHC 2012 proton–proton running period. *JINST*, 11: P05013, 2016. doi:10.1088/1748-0221/11/05/P05013.

[117] ATLAS Collaboration. Comparison between simulated and observed LHC beam backgrounds in the ATLAS experiment at $E_{\text{beam}} = 4\,\text{TeV}$. *JINST*, 13:P12006, 2018. doi:10.1088/1748-0221/13/12/P12006.

[118] ATLAS Collaboration. Characterisation and mitigation of beam-induced backgrounds observed in the ATLAS detector during the 2011 proton–proton run. *JINST*, 8:P07004, 2013. doi:10.1088/1748-0221/8/07/P07004.

[119] ATLAS Collaboration. Search for new phenomena in events with an energetic jet and missing transverse momentum in pp collisions at $\sqrt{s} = 13\,\text{TeV}$ with the ATLAS detector. *Phys. Rev. D*, 103:112006, 2021. doi:10.1103/PhysRevD.103.112006.

[120] S. Owen. Data-driven estimation of the QCD multijet background to SUSY searches with jets and missing transverse momentum at ATLAS using jet smearing. Technical report, CERN, Geneva, 2012. https://cds.cern.ch/record/1423310.

[121] ATLAS Collaboration. Tools for estimating fake/non-prompt lepton backgrounds with the ATLAS detector at the LHC. 2022. doi:10.48550/arXiv.2211.16178.

[122] ATLAS Collaboration. Electron efficiency measurements with the ATLAS detector using the 2012 LHC proton–proton collision data. ATLAS-CONF-2014-032, 2014. https://cds.cern.ch/record/1706245.

[123] R. Hyneman et al. Electron, Muon, and Photon Isolation in 2015-2018. Technical report, CERN, Geneva, 2019. https://cds.cern.ch/record/2672803.

[124] ATLAS Collaboration. Jet energy measurement and its systematic uncertainty in proton–proton collisions at $\sqrt{s} = 7\,\text{TeV}$ with the ATLAS detector. *Eur. Phys. J. C*, 75:17, 2015. doi:10.1140/epjc/s10052-014-3190-y.

[125] ATLAS Collaboration. Determination of jet calibration and energy resolution in proton–proton collisions at $\sqrt{s} = 8\,\text{TeV}$ using the ATLAS detector. *Eur. Phys. J. C*, 80:1104, 2020. doi:10.1140/epjc/s10052-020-08477-8.

[126] ATLAS Collaboration. A measurement of the calorimeter response to single hadrons and determination of the jet energy scale uncertainty using LHC Run-1 *pp*-collision data with the ATLAS detector. *Eur. Phys. J. C*, 77:26, 2017. doi:10.1140/epjc/s10052-016-4580-0.

[127] ATLAS Collaboration. Evaluating statistical uncertainties and correlations using the bootstrap method. ATL-PHYS-PUB-2021-011, 2021. `https://cds.cern.ch/record/2759945`.

[128] G. D'Agostini. A multidimensional unfolding method based on bayes' theorem. *Nucl. Instrum. Meth. A*, 362(2):487 – 498, 1995. ISSN 0168-9002. doi:10.1016/0168-9002(95)00274-X.

[129] J. M. Campbell et al. Event Generators for High-Energy Physics Experiments. In *Snowmass 2021*, 3 2022.

[130] J. Butterworth et al. PDF4LHC recommendations for LHC Run II. *J. Phys. G*, 43:023001, 2016. doi:10.1088/0954-3899/43/2/023001.

[131] S. Frixione, E. Laenen, P. Motylinski, C. White, and B. R. Webber. Single-top hadroproduction in association with a W boson. *JHEP*, 07:029, 2008. doi:10.1088/1126-6708/2008/07/029.

[132] ATLAS Collaboration. Studies on top-quark Monte Carlo modelling for Top2016. ATL-PHYS-PUB-2016-020, 2016. `https://cds.cern.ch/record/2216168`.

[133] ATLAS Collaboration. Measurement of the cross-section for electroweak production of dijets in association with a Z boson in pp collisions at $\sqrt{s} = 13\,\text{TeV}$ with the ATLAS detector. *Phys. Lett. B*, 775:206, 2017. doi:10.1016/j.physletb.2017.10.040.

[134] ATLAS Collaboration. Search for dark matter and other new phenomena in events with an energetic jet and large missing transverse momentum using the ATLAS detector. *JHEP*, 01:126, 2018. doi:10.1007/JHEP01(2018)126.

[135] J. Ellis. TikZ-Feynman: Feynman diagrams with TikZ. *Comput. Phys. Commun.*, 210:103–123, 2017. doi:10.1016/j.cpc.2016.08.019.

[136] C. Bierlich et al. Robust Independent Validation of Experiment and Theory: Rivet version 3. *SciPost Phys.*, 8:026, 2020. doi:10.21468/SciPostPhys.8.2.026.

[137] G. Cowan. *Statistical data analysis*. Oxford science publications. Clarendon Press, Oxford, 1998. ISBN 978-1-280-81976-6.

[138] L. Brenner, R. Balasubramanian, C. Burgard, W. Verkerke, G. Cowan, P. Verschuuren, and V. Croft. Comparison of unfolding methods using RooFitUnfold. *Int. J. Mod. Phys. A*, 35(24):2050145, 2020. doi:10.1142/S0217751X20501456.

[139] L. Lyons, D. Gibaut, and P. Clifford. How to combine correlated estimates of a single physical quantity. *Nucl. Instrum. Meth. A*, 270(1):110–117, 1988. ISSN 0168-9002. doi:https://doi.org/10.1016/0168-9002(88)90018-6.

[140] A. Valassi and R. Chierici. Information and treatment of unknown correlations in the combination of measurements using the BLUE method. *Eur. Phys. J. C*, 74: 2717, 2014. doi:10.1140/epjc/s10052-014-2717-6.

[141] R. Nisius. On the combination of correlated estimates of a physics observable. *Eur. Phys. J. C*, 74(8):3004, 2014. doi:10.1140/epjc/s10052-014-3004-2.

[142] G. D'Agostini. On the use of the covariance matrix to fit correlated data. *Nucl. Instrum. Meth. A*, 346(1):306–311, 1994. ISSN 0168-9002. doi:https://doi.org/10.1016/0168-9002(94)90719-6.

[143] L. Lista. Practical Statistics for Particle Physicists. In *2016 European School of High-Energy Physics*, pages 213–258, 2017. doi:10.23730/CYRSP-2017-005.213.

[144] V. Blobel and E. Lohrmann. *Statistische und numerische Methoden der Datenanalyse*. Teubner-Studienbücher : Physik. Vieweg+Teubner Verlag, 1998. ISBN 9783519032434. `https://books.google.de/books?id=NcIxajwHOZIC`.

Acknowledgements

First and foremost, I am extremely grateful to my supervisor, Monica Dunford, for her unwavering trust, insightful guidance, and tireless support. Beside all her obligations she acquired over the years, she always took the time to discuss physics never without sharing one of her many anecdotes.

I want to also express my deepest gratitude to Hans-Christian Schultz-Coulon, who welcomed me into his group and who supported, challenged, and motivated me in equal measures. I am very grateful to him for taking great care of the well-being of everyone in the group.

I want to specially thank Stephanie Hansmann-Menzemer for not only agreeing to be the second referee of this thesis, but also for all the work she invested in the research training group, and in particular for the time she took to supervise my student lecture.

I would like to thank Martin for introducing me to the ATLAS detector, in particular, to the Level-1 calorimeter trigger system, I really enjoyed the time working on the operation of the trigger. Silvia and Jan added to the overall experience that made me feel comfortable during my time at CERN, for which I am grateful.

It is not farfetched to say that without the contributions of Sebastian to the detector corrected boson + jet analysis, the presented work would not have been in such a final state as it is to this day. I am very thankful for all his help and advice reaching far beyond the day-by-day work related topics. It was a pleasure to work with him on this analysis. I would like to thank the entire team for all the lessons I was able to learn which turned out to be extremely helpful for the $\Gamma_Z(\text{inv})$ measurement, and I especially enjoyed our rare, in person collaboration meetings in the UK.

I would like to particularly thank Falk for his outstanding colour scheme used throughout this thesis. He also contributed by helping me to focus on life outside of physics by joining uncountable boardgame nights and climbing sessions, to which Hannah sometimes kept us company.

Falk, Sebastian, Thomas and myself share a questionable obsession of farm animals, farming tools, and farm buildings. I am grateful for the time we shared managing our farm and the many lessons I was able to learn from you at any time day or night.

I am very thankful to all my proofreaders and group members: Anke, Falk, Hannah,

Lisa, Mathias, Pavel, Philipp, Rainer, Sebastian, Thomas and Varsiha - but I am even more grateful for the great time we shared together at KIP, which of course includes everyone who was part of F8 and F11 over the past years.

A very special thanks goes out to Pierre-Hugues Beauchemin who trusted me in putting his idea of this measurement into action which he is eager to perform at a hadron collider already since the CDF data-taking. I want to express my gratitude for our very instructive bi-weekly discussion sessions which soon turned to weekly early morning chats for him, and I am looking forward to working with him in the future.

I want to thank all my friends I was able to make during my time in Heidelberg, and was able to keep from back home, and I want to express my dearest apologies to every one of you which I have not been able to see in these intense last months. I am very grateful for all the support my family offered me during all those years. Last but not least, I want to thank my partner, Iris, for always being there for me and supporting me throughout these last years we were able to spend together, I am looking forward to the many more to come.